Observation of Total Column Water Vapour

Dissertation

zur Erlangung des akademischen Grades eines Doktors der Naturwissenschaften am Fachbereich für Geowissenschaften der Freien Universität Berlin.

Autor:
Hannes Diedrich

Berlin, März 2016

Erstgutachter: Prof. Dr. Jürgen Fischer

Zweitgutachter: Prof. Dr. Ralf Bennartz

Tag der Disputation: 18.05.2016

Selbständigkeitserklärung

Hiermit erkläre ich an Eides statt, dass ich die vorliegende Arbeit selbständig und ohne fremde Hilfe angefertigt, keine anderen als die angegebenen Quellen und Hilfsmittel benutzt und die den benutzen Quellen wörtlich oder inhaltlich entnommenen Stellen als solche kenntlich gemacht habe. Diese Arbeit hat in gleicher oder ähnlicher Form noch keiner Prüfungsbehörde vorgelegen.

Berlin, März 2016

Contents

Chapter 1

Introduction

1.1 The role of water vapour in the Earth's climate

In the Earth's atmosphere, all possible phases of water are present: solid (ice), liquid (cloud droplets) and gas (water vapour). The sun drives the transformation between those phases, the water cycle. Figure 1.1 shows a schematic view of the global water cycle. Water evaporates from the surface (predominantly from the ocean) and can form clouds and precipitation. Only 0.001 % of the total amount of water is situated in the atmosphere (Durack 2015), where water vapour is the main fraction with 99 % (Wentz *et al.* 2007). Water vapour transports a large amount of energy through latent heat and is a big contributor to the Earth's energy budget. Additionally, water vapour plays a vital role in the formation of clouds and precipitation and is thus responsible for the transport of water to land surfaces (IPCC 2007).

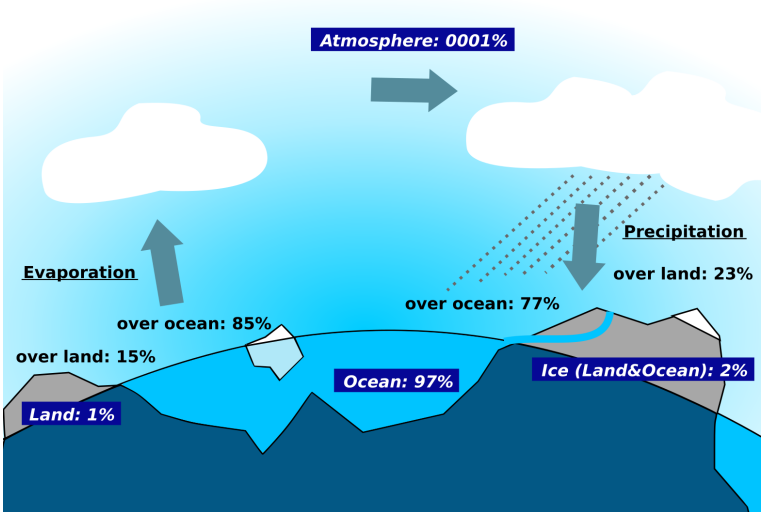

FIGURE 1.1: Schematic view on the water cycle; Numbers from Durack (2015).

Water vapour is the most common trace gas (1 % to 4 % of volume of the atmosphere) and is responsible for 60 % of the total greenhouse effect for clear skies due to the fact that it is the main contributor of absorption in the infrared (IR) spectrum where the Earth emits radiation (Kiehl and Trenberth 1997, Trenberth *et al.* 2009). Only a small fraction of the shortwave radiation originating from the sun is attenuated, but a large amount of terrestrial long wave radiation is hold back from emitting back into space due to water vapour.

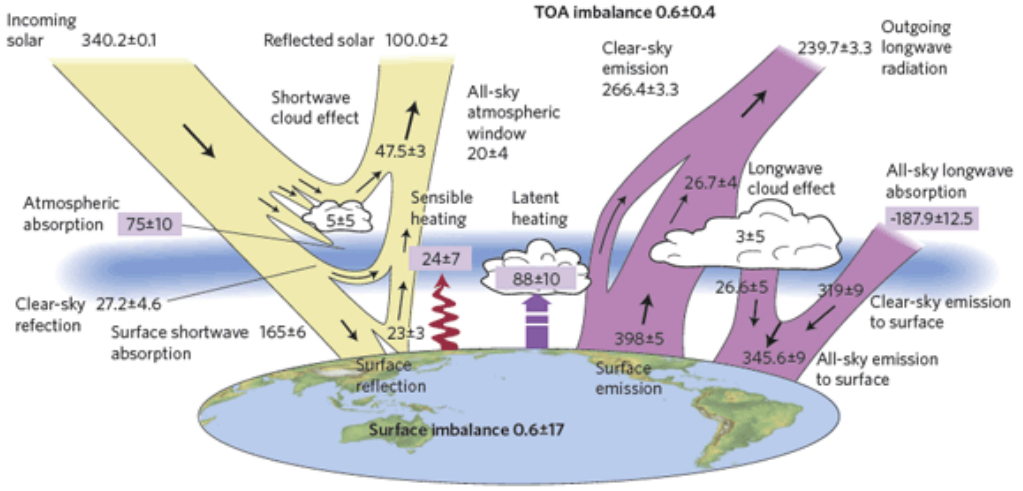

FIGURE 1.2: Global annual mean energy budget of the Earth for the period 2000–2010. Solar fluxes in yellow and infrared fluxes in pink are displayed in W/m^2. (Stephens *et al.* 2012)

Figure 1.2 shows an overview of the energy fluxes that contribute to the global energy budget. The top of atmosphere (TOA) fluxes were mainly derived from observations of the Clouds and the Earth's Radiant Energy System (CERES) space borne broad scanning radiometer (Stephens *et al.* 2012). $340.2 \pm 0.1\,\mathrm{W/m^2}$ of solar radiation reach the top of the atmosphere from which $100 \pm 2\,\mathrm{W/m^2}$ are reflected again by clouds and the Earth's surface. The resulting $240\,\mathrm{W/m^2}$ are absorbed by the atmosphere, its constituents (clouds and aerosols) and the Earth's surface, that emits radiation in the IR in the range of $239.7 \pm 3.3\,\mathrm{W/m^2}$. This results in a TOA imbalance of about $0.6\,\mathrm{W/m^2}$ with an accuracy of $0.4\,\mathrm{W/m^2}$, which is mostly due to instrument calibration errors. This imbalance appears in the change of the global mean temperature. Approximately one fifth of the incoming solar radiation is absorbed by the atmosphere. This component has one of the largest uncertainties in the scheme in Figure 1.2, which is mainly resulting from the uncertainties in the concentrations of greenhouse gases such as water vapour. Another uncertainty in the approximation of the radiation budget is the influence of clouds. About 70 % of the Earth's surface is covered by clouds (Stubenrauch *et al.* 2013). Clouds can reflect shortwave radiation, emit longwave radiation and hold back emitted longwave radiation from radiating back into space. As clouds form from water vapour,

the consideration of clouds in investigations concerning water vapour is necessary and vice versa.

1.2 The role of water vapour in a changing climate

The abrupt rise of the global mean surface temperature in the last three decades is the most popular indicator of climate change. As stated by IPCC (2014), the majority of investigations suggest that the climate change is associated with anthropogenic activities such as the emission of carbon dioxide (CO_2) due to fossil fuel burning or the enhanced emission of methane (CH_4) due to agricultural activities, among others. The imbalance of the Earth's energy budget as a result of the increased absorption of longwave radiation, is the main result of these changes. Additionally, several feedback mechanisms arise from the warming of the climate, concerning for example cloud formation, emittance of greenhouse gases and even the see level rise. Generally, in a warmer atmosphere it is more likely that water evaporates, because the relative humidity tends to remain more or less constant, as observations and numerical experiments consistently show (Held and Soden 2006, Wentz *et al.* 2007). Furthermore, there are a number of positive and negative feedbacks related to water vapour explained in the following.

In general, the presence of water vapour in the atmosphere causes an enhanced effect of the other greenhouse gases. A small positive variation in the amount of e.g. CO_2 results in a small decrease of longwave emission and an increase in temperature. Since the water vapour amount is increasing rapidly with air temperature, water vapour acts as an amplifier of the initial warming (Soden 2002).

Due to the exponential decrease of water vapour concentration with height and strong absorption features of water vapour in the IR, the emitted radiation of the Earth is effectively covered by the lower atmosphere. Consequently, the air layer that is responsible for the emission of longwave radiation is situated in the middle troposphere at around 5 km (mean over the whole globe, dependent on the water vapour amount). An increase in the atmospheric mean temperature results in a lifting of the effective height of emittance (Held and Soden 2000). Consequently, the volume that can hold water vapour is increased which in turn entails in an enhanced warming. As Shi and Bates (2011) state, the mean Upper Tropospheric Humidity (UTH) has increased in the last 30 years. The transportation of humidity to the higher troposphere can increase the formation of clouds. Clouds can serve as a reflector (mostly low level clouds) or as an insulator (mainly high clouds). Which of these effects is dominating and how the cloud water vapour feedback will evolve in the future is subject of various studies (IPCC 2014). Ramanathan *et al.* (1989) and Loeb *et al.* (2009) suggest that the reflection of shortwave radiation exceeds the global radiative forcing effect resulting in an overall cooling of the climate. However, there is substantial ambiguity of global-scale observations of cloud cover trends. Additionally, clouds are the greatest source of uncertainty in climate models due to the complex cloud formation processes including interaction with aerosols and water vapour (IPCC 2014).

Which one of these feedback mechanisms concerning water vapour is dominating, is still under active investigation. Most of the statements above originate from climate predictions of Global Circulation Models (GCM). Although the accuracy of these models is increasing due to improvement of the parametrisations and larger computational capability, the extensive monitoring of the change in water vapour in the atmosphere is crucial. Observations are the basis for a better understanding of the Earth's atmosphere and its feedback mechanisms. Furthermore, climate monitoring and evaluation of the model outputs can only be done with the help of ground and space borne observations.

Due to the immense importance of water vapour to the climate, more and more research groups and associations invest in studies related to water vapour. Recently, the Global Climate Observing System (GCOS) declared the total column of water vapour (TCWV) as an essential climate variable. The defined goal of GCOS is to provide long time series of TCWV in sufficiently high resolution to enable the determination of both local and global trends (GCOS 2010).

There are multiple data sets of TCWV derived from ground and space borne observations. The outcomes of trend analysis are diverse, but suggest a global increase of TCWV. Jin *et al.* (2007) found an average TCWV trend of about 2 mm per decade during 1994-2006 over GNSS stations that are mainly based on land. Over oceans of about 1.2 % per decade has been observed between 1989 and 2004 with space borne microwave radiometer Trenberth *et al.* (2005), Wentz *et al.* (2007). However, trends in the water vapour field deviate regionally. Mieruch *et al.* (2008) found significant trends ranging from -5 % to 5 % per year in the time between 1996 to 2006. Docter (2015) performed TCWV trend analysis from observation over global cloud-free land areas that reveal trends between -0.5 mm and +1 mm in the time between 2003 and 2012. In order to represent those small trends significantly, sufficient high accuracies of the TCWV observations are required.

1.3 Satellite remote sensing of water vapour

The sounding of humidity already started in the early 1920s with the first ascends of radiosondes (Pralungo *et al.* 2014). For the first time, the aggregation of vertical resolved information about temperature, humidity and wind was possible. The number of radiosonde stations increased over the years and served the understanding of the stratification of the atmosphere. Nowadays, soundings are an important part of the data that is needed for numerical weather prediction (NWP). However, the spatial distribution of radiosonde stations is too sparse for most parts of the Earth and mainly located on land areas. Additionally, the in some countries the number of radiosonde stations is decreasing. This is the result of the increasing importance of satellite remote sensing data that is assimilated into the NWP models.

Remote sensing from space can provide accurate monitoring of water vapour in high spatial and temporal resolution over long time series. Amongst others, these observations are needed for:

- improving the knowledge about the atmospheric processes concerning water vapour
- monitoring of the Earth's climate and its evolution
- assimilation of data into NWP and climate models

Remote sensing of water vapour with satellites started in the 1960s with the launch of the first meteorological satellite, the Television Infrared Observation Satellite (TIROS 2) (Bandeen *et al.* 1961). Since then, a number of meteorological satellites with instruments that are able to seek information about water vapour were launched. The number of possibilities and the accuracy increased with technological progress. Passive remote sensing methods are described hereafter.

The majority of the procedures use either reflected sunlight in the wavelength-range of 400 nm to 3 µm or terrestrial radiation emitted by the Earth (4 µm–20 cm). The suitable wavelength range strongly depends on the application. For water surfaces measurements in the microwave region is most suitable. For land applications the visible and near infrared range (NIR) is appropriate. In the thermal infrared, it is possible to retrieve information about the vertical distribution of water vapour.

Water vapour remote sensing over water surfaces is done since the 1980s with microwave radiometers such as the Special Sensor Microwave/Imager (SSM/I) (Schluessel and Emery 1990). The procedures use a water vapour absorption and emission band at 23 GHz (approximately 1,5 cm wavelength). The main advantages are:

1. Observations at day and night-time are possible, because earth and atmosphere emit radiation in the microwave spectrum.
2. A small influence of liquid water absorption can be accounted for in the retrievals. Consequently, TCWV can be derived even in the presence of clouds (except for heavy rain clouds).

Due to the fact that scattering on atmospheric particles can be neglected, the accuracy of the TCWV retrievals in the microwave spectrum is very high. The spatial sampling of about 20 km is sufficient for a global view but does not allow investigations of small scale effects.

Remote sensing of water vapour using measurements in the thermal infrared allows the sounding of vertical profiles of water vapour concentrations. This can especially serve the monitoring of middle and upper tropospheric humidity in order to quantify climate feedback effects (see Section 1.2), whereas TCWV is dominated by water vapour in the boundary layer. One example for such a sensor is the Infrared Atmospheric Sounding Interferometer (IASI) mounted on Metop Satellites. IASI brightness temperatures are derived in the strong water vapour absorption band between 5 µm and 8 µm with high spectral resolution of 0.2 nm. Sophisticated procedures convert these to temperature- and humidity profiles with a vertical resolution of about 2 km (Amato *et al.* 2009, Pougatchev *et al.* 2009, Wiegele *et al.* 2014). IASI data is assimilated into NWP models

for day and night over-paths. However, the accuracy in the lower troposphere, where most of the water vapour is located, is of about 10 % (Masiello *et al.* 2013). Additionally, the spatial resolution of about 12 km and the limitation to cloud-free scenes are further constraints. Similar instruments that are used to retrieve water vapour profiles are the Advanced microwave sounding unit (AMSU) on board Metop (Rosenkranz 2001) and the Atmospheric Infrared Sounder (AIRS) on board Aqua (Susskind *et al.* 2003).

There are also some retrievals that retrieve TCWV from infrared measurements around 10 µm, such as Casadio *et al.* (2016) for the Along Track Scanning Radiometer (AATSR) on board ENVISAT and Schroedterhomscheidt *et al.* (2008) for Spinning Enhanced Visible and Infrared Imager (SEVIRI) on board the geostationary Meteosat Second Generation (MSG). The latter enables TCWV observations with a temporal resolution of 15 minutes over cloud-free land surfaces. Nevertheless, the uncertainties are comparable high due to only weak water vapour absorption features in this spectral range.

Radiance measurements of reflected sunlight in the visible (VIS) spectral range can be used for the determination of TCWV e.g. (Grossi *et al.* 2015, Noël *et al.* 2002, Schrijver *et al.* 2009, Wagner *et al.* 2006). Although these procedures can provide TCWV on a high spatial resolution even over ocean surfaces, they face some challenges such as Rayleigh scattering and a strong influence of atmospheric scatterers. Additionally, the sensitivity to water vapour is comparably low due to weak absorption features in the VIS. Consequently, the uncertainties are higher in comparison to other methods.

High accuracies of TCWV observations over land surfaces can be achieved by retrievals that use radiance measurements in the NIR around 950 nm. In this spectral range the influence of Rayleigh scattering and aerosol scattering is lower than in the VIS. Although limited to cloud-free daytime scenes, high spatial resolutions up to 260 m x 290 m are possible. Here, the most dominant challenges are the surface reflectance and the scattering on atmospheric particles. However, these can be overcome by multi-spectral measurements. Good examples for multi-spectral instruments that can serve for TCWV remote sensing are the MOderate Resolution Imaging Spectroradiometer (MODIS) on board Aqua and Terra (Gao and Kaufman 2003) and the MEdium Resolution Imaging Spectrometer (MERIS) on board ENVISAT (Bennartz and Fischer 2001, Diedrich *et al.* 2015, Lindstrot *et al.* 2012) that play a superior role in this thesis.

Until now, observations of TCWV with sufficient accuracies are limited to polar orbiting satellites. First, microwave sounder are not applicable on geostationary satellites because of the quadratic reduction in energy with distance. Secondly, the instruments of the current generation of earth scanning spectrometers on e.g. MSG do not have channels that measure radiation in a water vapour absorption band with sufficient sensitivity to TCWV. The existing MSG water vapour channels are only sensitive to water vapour in the mid troposphere. The outputs are used for monitoring of atmospheric streams. The next generation of spectrometer on geostationary satellites is planned to measure in water vapour absorption channels in the NIR. This will enable observation of TCWV on a temporal resolution of about 5 minutes.

Recent studies address retrievals of water vapour isotopes investigating the sources and the circulation of water vapour in the atmosphere, serving the understanding of the water cycle. In detail, the ratio of semiheavy water and water (HDO/H_2O) provides information about the genesis and the age of the water vapour, because the heavier HDO is depleting more likely when water vapour condensates in contrast to evaporation. High spectral resolutions are needed to cover the weak absorption features in the IR. Due to the scarcity of water isotopes in the atmosphere, the retrievals face high uncertainties (Boesch *et al.* 2013, Frankenberg *et al.* 2009, Randel *et al.* 2012). However, this is a very promising field of study and can help to evaluate the representation of the water cycle in global climate models (Risi *et al.* 2012).

1.4 Aim and outline of thesis

The main aim of this thesis is the development of a sensor-independent total column water vapour retrieval for instruments that measure radiance in the $\rho\sigma\tau$-water vapour absorption band for cloud-free daytime land and ocean scenes. The motivation for the implementation of the retrieval was to produce long, consistent time series of TCWV with high spatial resolution in order to serve:

- climate monitoring, especially the trend analysis of TCWV
- atmospheric correction, especially for ocean color remote sensing
- studies about small scale phenomena of TCWV
- studies about cloud formation mechanisms
- numerical weather and climate prediction

The work was performed in the frame of the WaDaMo project funded by the *Bundesministerium für Wirtschaft und Forschung* (BMWi).

The algorithm was adapted to the MERIS and MODIS setup and will be applied for future missions such as the Ocean and Land Color Instrument (OLCI) on Sentinel-3, the Flexible Combined Imager (FCI) on Meteosat Third Generation (MTG), METimage on Metop-SG satellites and Sentinel-2. The architecture and the functionality of the TCWV retrieval is demonstrated in Chapter 3 and is partly based on the publication from Diedrich *et al.* (2015).

As stated in the last paragraph, the accuracy of the TCWV retrievals is of major importance for the interpretation of the retrieved data. Therefore, Chapter 4 is dedicated to the theoretical quantification of uncertainties of TCWV retrievals that use radiance measurements in the NIR, particularly for the future missions. The corresponding publication (Diedrich *et al.* 2013) has been considered in the decision-making process of the channel setting of OLCI which has been successfully launched into space on Sentinel-3

on February 16, 2016. Additionally, the universal TCWV retrieval provides uncertainty estimates on a pixel basis, taking all uncertainties into account that are introduced through assumptions in the forward model and errors of the input data.

The performance of the retrieval was evaluated against several sources of ground based TCVW observations. These play another important role in this thesis. First, they are compared to the TCWV retrieval for validation studies, including data sets of microwave radiometers (MWR), radiosondes, stations of the Global Navigation Satellite System (GNSS) and sun-photometer.

Secondly, GNSS TCWV data were used to derive the representativeness of TCWV observations from space. In particular, the influence of the constraint of cloud-free daytime measurements and the fact that polar orbiting satellites have low temporal coverage are discussed on Chapter 5. This study was submitted to the *Journal of Atmospheric Chemistry and Physics*.

Third, the availability of combined information of clouds and TCWV raised the idea of an application of TCWV. In Chapter 7, GNSS TCWV is combined with cloud information data in order to quantify the statistical relationship between water vapour and cloud properties.

In Chapter 2, the theoretical basis about radiative transfer, the used radiative transfer model, techniques, and description of the ground based TCWV data sets are presented.

A summary and an outlook concerning all partial studies is given in Chapter 7.

Chapter 2

Fundamentals

2.1 Water vapour

Unlike most trace gases, atmospheric water vapour is highly variable in space and time. The concentration of atmospheric water vapour depends on:

- the temperature of the surface body (land or water)
- the availability of water on the surface
- atmospheric turbulence (advection, convection)

Under normal atmospheric conditions, assuming no turbulence, water vapour evaporates and the partial pressure of water vapour in the air e is increasing until the saturation vapour pressure e_s is reached. e_s is directly coupled to the temperature of the surface via the Clausius-Clapeyron equation:

$$\frac{\mathrm{d}e_s}{\mathrm{d}T} = \frac{L_v(T)\ e_s}{R_v\ T^2}\ , \tag{2.1}$$

where T the temperature, L_v the specific latent heat of evaporation of water and R_v the individual gas constant of water vapour. Presuming an equilibrium of evaporation and condensation, the water vapour amount over warm surfaces is higher than over cold surfaces. However, the time that is needed for reaching this equilibrium, is usually higher than the change of the air mass above the surface through advection or convection. Consequently, the air is usually unsaturated. Furthermore, the availability of water is crucial for the water vapour amount.

Figure 2.1 shows vertical profiles of the temperature and specific humidity (SH), that is defined by the fraction of mass of water vapour to the mass of the air parcel. The profiles are standard atmospheres taken from McClatchey *et al.* (1972) and represent averaged conditions in the corresponding climatological areas. The most obvious feature is the increase of SH with increasing temperature that is connected with a decrease of

latitude (see brackets on the right panel of Figure 2.1). Additionally, the temperature and SH are higher in the summer month for the mid-latitude and subarctic profiles. The Total Column Water Vapour (TCWV) is defined as the integral of SH over the whole vertical column along the pressure levels to the surface pressure p_s:

$$\mathrm{TCWV}(p_s) = \frac{1}{1000 \times g} \int_0^{p_s} \mathrm{SH}(p)\; p \,\mathrm{d}p \;, \tag{2.2}$$

where g is the Earth's gravity constant. The TCWV describes the height of a column of water in mm that would result if all water in the air is condensed. Furthermore, Figure 2.1 shows that most of the water vapour is located in the lower air layers below 850 hPa. Over 90 % of the TCWV is situated in the lowest 5 km (lower than 500 hPa) (Liou 2002).

The top panel of Figure 2.2 shows the global distribution of the annual mean TCWV. Here again, the water vapour amount is increasing with decreasing latitude generally due to the increase of mean air temperature with decreasing latitude (represented by the annual mean of the 2 meter temperature in the lower panel of Figure 2.2). However, there are regions in the low latitudes where the temperature is high on average that also show low TCWV such as the Sahara, due to the low availability of water. Over the ocean, the TCWV is generally following the sea surface temperature (as described by the Clausius-Clapeyron equation). For example, the pacific area west of South America, were the sea surface temperatures are low due to the cold Humboldt current, the TCWV is also decreased. Additionally, the decrease of TCWV with height is also visible by the decreased TCWV values over elevated areas such as the Andes.

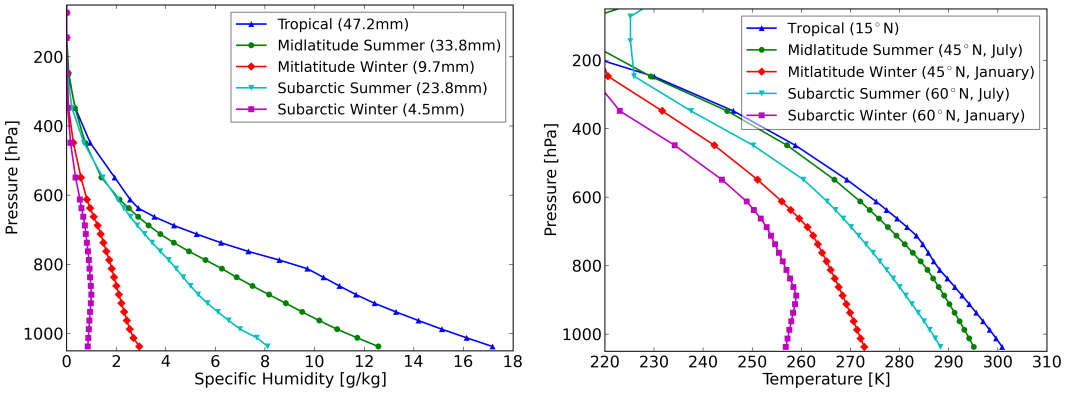

FIGURE 2.1: Profiles of specific humidity in g/kg (left) and temperature in K (right) for 6 standard profiles from McClatchey *et al.* (1972). The values in brackets indicate the corresponding TCWV (left plot) and the corresponding month and latitude (right plot).

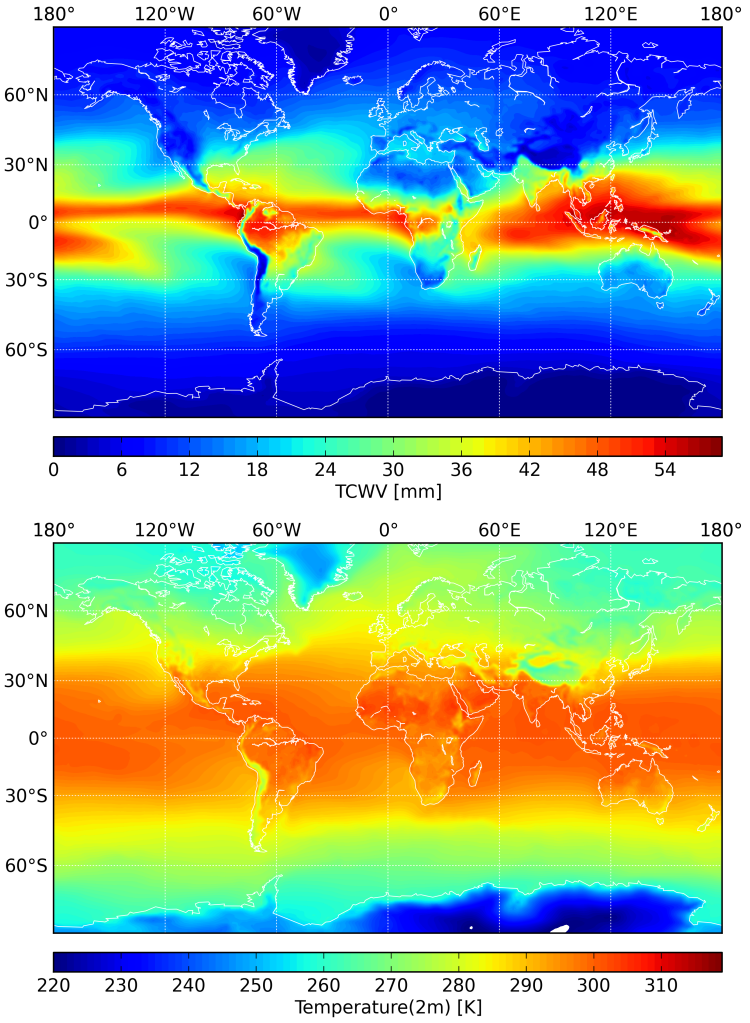

FIGURE 2.2: Upper panel: Global distribution of the annual mean TCWV in mm; lower panel: global distribution of temperature at 2 m in K. The data was extracted from ERA-Interim reanalysis data (Dee *et al.* 2011) and averaged for the year 2012.

2.2 Satellite remote sensing and radiative transfer

Remote sensing is usually defined as the gathering of information about a phenomenon without making physical contact with the matter. Here, the phenomenon is the total column water vapour that is distributed in the atmosphere. Naturally, the atmosphere is highly complex and variable. In order to retrieve TCWV, first radiative transfer simulations have to be performed and afterwards an inversion technique compares simulated and measured radiances from space borne radiometers. The radiative transfer calculations have to account for gaseous absorption, scattering of atmospheric particles such as aerosol as well as the properties of the Earth's surface.

This thesis focusses on the remote sensing of water vapour of reflected sun light. Consequently, this section dwells only on the mechanisms that correspond to radiation in the

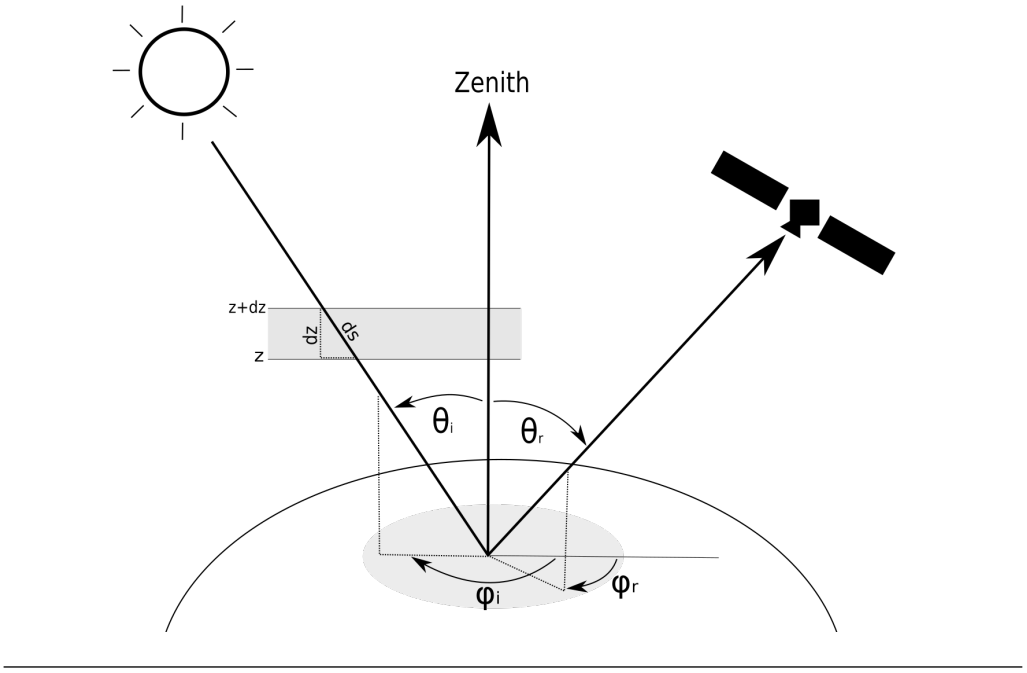

FIGURE 2.3: Satellite viewing geometry.

VIS to NIR and its applications to remote sensing. Figure 2.3 shows a scheme of the viewing geometry of a satellite instrument. It describes the path of the radiation that is emitted by the sun, reflected by the Earth's surface and received by the spectrometer at TOA. The solar zenith angle θ_i, viewing zenith angle θ_r, the solar azimuth angle ϕ_i and the viewing azimuth angle ϕ_r describe the viewing geometry of a remote sensing setup and is used in hereafter. ds represents the infinitesimal photon path through the atmosphere.

Radiative transport equation

In the following it is referred to the books of Liou (2002) and Petty (2006).

Sunlight is attenuated by the atmosphere. The initial radiation L_0 at a certain monochromatic wavelength λ is extenuated over an infinitesimal thickness ds of the medium. The attenuated radiance L can be described by:

$$L(\lambda) = \beta_e(\lambda)\ L_0(\lambda)\ ds, \tag{2.3}$$

where β_e is the extenuation coefficient that can be divided into two components, the absorption coefficient β_a and the scattering coefficient β_s with the unit [length^{-1}] or [mass^{-1}]:

$$\beta_e(\lambda) = \beta_a(\lambda) + \beta_s(\lambda)\ . \tag{2.4}$$

$L(\lambda)$ is the spectral radiance that is the power per unit area, solid angle, and spectral unit [$\mathrm{Wm^{-2}nm^{-1}sr}$]. The integration of Equation 2.3 along the path between the points s_1 and s_2 results in the *Beer's Law*:

$$L(\lambda, s_2) = \; L(\lambda, s_1) \exp\left[-\int_{s_1}^{s_2} \beta_e(\lambda, s) ds\right] \; . \tag{2.5}$$

The integral over the extinction coefficient along a distance is defined as the optical thickness τ that increases with increasing path length:

$$\tau(\lambda, s) = \int_{s_1}^{s_2} \beta_e(\lambda, s) ds \; . \tag{2.6}$$

The transmittance t of the air package is defined as the ratio of the radiance before and after the attenuation through the medium. With that, Equation 2.5 transforms to:

$$t = \frac{L(\lambda, s_2)}{L(\lambda, s_1)} = \exp\left[-\tau(\lambda, s_2 - s_1)\right] \; . \tag{2.7}$$

The transmittance is measure of the penetrability of the medium ranging from one for no attenuation ($\tau \to 0$) and zero of total extinction ($\tau \to \infty$).

The fundamental description of radiative transfer is represented by the following equation:

$$\frac{dL(\lambda, \tau)}{d\tau} = J(\lambda, \tau) - L(\lambda, \tau) \tag{2.8}$$

where J is the source term. In the solar spectrum ($\lambda < 3.5 \mu m$) it represents the incoming diffuse radiation mainly resulting from scattering. Consequently, additional to the absorption, radiative transfer has to account for single and multiple scattering.

Absorption of water vapour

The absorption of light by atmospheric gases is the result of absorbing and re-emitting of photons with distinct energies that are fixed by the energy gap between quantum stages of atmospheric molecules. The energy E of a photon is defined by its frequency or wavelength λ after the Einstein's law:

$$E = \frac{hc}{\lambda} \; , \tag{2.9}$$

where h is the Planck's constant, c the speed of light. As the molecules have distinctive energy levels, monochromatic absorption lines occur. The number and intensity of the absorption features depend on the number of energy levels of the molecules and the amount of the absorbing matter along the photon path. However, the absorption is not just limited to the distinct wavelengths when measuring absorption spectrum of the atmosphere. Three mechanisms are responsible for broadening of the monochromatic absorption lines:

Natural Broadening The *Heisenberg uncertainty principle* describes the relationship between the lifetime of an exited state Δt and the uncertainty of the energy between two states ΔE:

$$\Delta E \Delta t \approx h. \tag{2.10}$$

With Equation 2.9 it follows that the the shorter the lifetime of an exited state, the higher is uncertainty of the wavelength of the absorption line, thus the scattering around the original absorption line. This effect is minor in comparison to the two following.

Pressure Broadening Due to collisions of the absorbing molecules, the lifetime of exited states is reduced. The strength of this mechanism increases with higher molecule density. Consequently, it dominates the broadening in the lower atmosphere. The shape of the broadened line can be approximated by the Lorentz profile g_L as a function of distance to the idealized monochromatic absorption line $(\lambda - \lambda_0)$ and is therefore called Lorentz broadening:

$$g_L(\lambda - \lambda_0) = \frac{1}{\pi} \frac{\alpha}{(\lambda - \lambda_0)^2 + \alpha^2} \ , \tag{2.11}$$

where α is the line half width, dependent on the pressure p and temperature T, and is defined by:

$$\alpha(p, T) = \alpha_0 \left(\frac{p}{p_0} \right) \left(\frac{T_0}{T} \right)^n \tag{2.12}$$

n is an empirical determined exponent, α_0 is the line width at the reference pressure p_0 and temperature T_0 .

Doppler Broadening The motion of the molecules introduces a shift of frequencies ν due to the Doppler-effect. The shifted frequency is given by

$$\nu' = \nu(1 - \nu c) \ . \tag{2.13}$$

The Doppler broadening line shape g_D can be estimated by the function:

$$g_D(\lambda - \lambda_0) = \frac{1}{\alpha_D \sqrt{\pi}} exp \left[- \frac{(\lambda - \lambda_0)^2}{\alpha_D^2} \right] \tag{2.14}$$

where α_D is the temperature dependent Doppler half width:

$$\alpha_D = \frac{\lambda_0}{c} \sqrt{2RT} \ . \tag{2.15}$$

Consequently, the line width increases with higher temperatures because of the larger scattering of velocity of the molecules.

Figure 2.4 shows the line shapes of the Doppler and Lorentz broadening for equal width and strength. Pressure broadening is dominant in the lower troposphere, whereas Doppler broadening is dominant in higher air layers. Both mechanisms influence the absorption lines at the same time. As a consequence, the observed line shape is a combination of both and can be approximated with the Voigt line profile. The Voigt shape

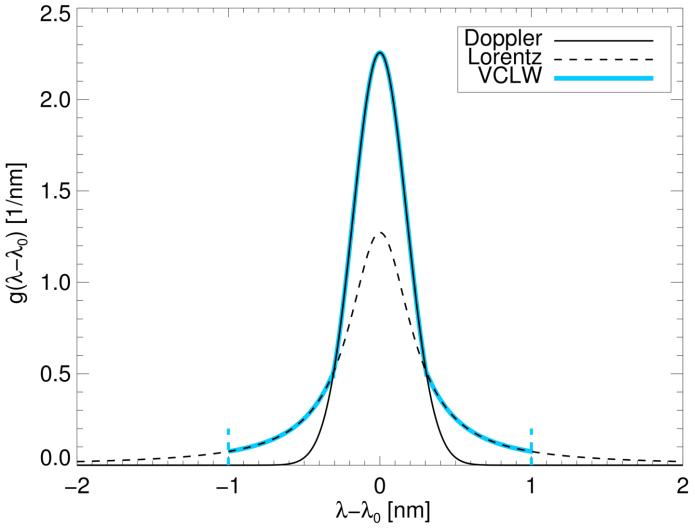

FIGURE 2.4: Doppler and Lorentz line shapes with equal strengths and width of 1 nm.

follows the Doppler profile near the center of the line and the Lorentz profile at the edges. Due to the fact that the Lorentz profile has an indefinite width, the edges are additionally cut off in the Voigt Center Lorentz Wings (VCLW) profile (see Figure 2.4). Data-bases of the spectral properties of atmospheric gases such as from Rothman *et al.* (2013) provide extensive information about the position, depth, and width of each absorption line. From these information and the knowledge about temperature, pressure and amount of gases, the absorption spectrum the atmosphere can be derived by adding all individual VCLW profiles (Doppler *et al.* 2014a) (see Figure 2.5).

The top panel of Figure 2.5 shows the absorption features of water vapour in the electromagnetic spectrum ranging from VIS (400 nm) to 30 µm. The comparison to the total atmospheric absorption (lower panel) reveals that the predominant part of the absorption that is taking place in the atmosphere is due to water vapour. This results from the quantum mechanical properties of the water molecule explained in the following. The water molecule is polar and is thus free to rotate around all three axes. First, water vapour can absorb and emit radiation in the microwave and far-IR (50 µm - 10 cm) due to changes in its rotational energy levels and second, it can absorb radiation on the NIR and mid-IR (1 µm to 50 µm) due to changes in its vibrational and rotational energy levels (Shine *et al.* 2012). Between the resulting strongly absorbing bands, there are regions with weaker absorption, the window bands. The absorption in these window bands is dominated by the so-called water vapour continuum. It has two components: The self continuum, due to interactions between water molecules and especially dimers ($(H_2O)_2$), and a foreign continuum due to interaction between water molecules and other air molecules. In most spectral parts, the water vapour continuum can modelled by the Lorentz wings of the VCLW line profile (Doppler *et al.* 2014a). Although a lot of studies

have been performed in the past and are still ongoing, the exact characteristics of the water vapour continuum are still unknown (Ptashnik *et al.* 2011).

Another influence to the absorption of water vapour are water isotopes such as semiheavy water (HDO) or $H_2{}^{18}O$. Despite the low abundance (<0.1 % in comparison to water vapour ($H_2{}^{16}O$)), they contribute significantly to the absorption scheme of water vapour, especially in the IR.

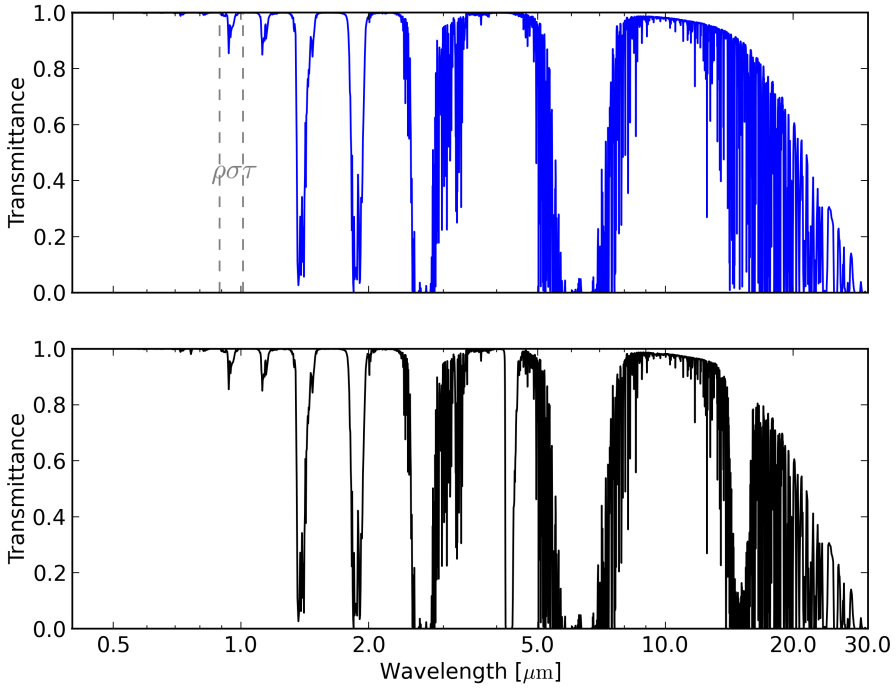

FIGURE 2.5: Transmittance of a standard latitude summer atmosphere as a function of wavelength for only water vapour (top panel) and including all atmospheric gases (bottom); derived with method of Doppler *et al.* (2014b) and data from Rothman *et al.* (2010).

Following Equation 2.5, the strength of absorption depends on the absorption coefficient that is dependent on the amount of absorbing substance and the length of the path that the photons travelled through the medium. As described in the previous section, the concentration of water vapour is increasing exponentially with pressure, thus with decreasing height. Consequently, the transmittance of the atmosphere is a function of height. For most of the absorption bands with low total atmospheric transmittance shown in Figure 2.5 the majority of the photons do not reach the surface of the atmosphere in that spectral range. The derivative of the transmittance with height is called *weighting function* and provides information about the height where the change of absorption is maximal, considering a measurement with a spectrometer at TOA. This feature can be utilized in order to retrieve information about the vertical profile of the water vapour or concentrations of water vapour in a certain height, e.g. the upper tropospheric humidity.

TABLE 2.1: Common sizes of atmospheric particles

Particle	Radius
Molecules	1 nm
Dust, Smoke, Haze	1 µm - 10 µm
Cloud Droplets	10 µm
Raindrops	1 mm

In order to retrieve water vapour of the whole vertical column, it is favourable to use absorption bands with sufficient absorption strength and where the weighting function peaks at around the surface. This is valid for the absorption band in the NIR in particular in the range around 940 nm in the so called ρστ-band (highlighted in the top panel of Figure 2.5).

Scattering and absorption of atmospheric particles

There is a high diversity of particles in the atmosphere. In interaction with electromagnetic radiation, two microscopic properties of atmospheric particles are important: the refractive index and the size parameter. The refractive index is a unit-less measure of absorption and scattering of the medium and is strongly dependent on the material and the incident wavelength. The relationship between the size of a particle and the wavelength of the radiation of interest is an important property of the particle and is represented by the size parameter x that is defined by:

$$x = \frac{2\pi r}{\lambda} \ , \tag{2.16}$$

where r is the radius of the particle and λ the wavelength of the incident wave. Typical radii of common atmospheric particles are displayed in Table 2.1. Is a particle sufficiently small in comparison to the wavelength ($x \ll 1$), the scattering process can be described by the Rayleigh-theory (Rayleigh 1928). In case of spherical particles that have the same dimension of the wavelength or are even bigger ($x \geq 1$) the Mie-theory can be applied in the radiative transfer simulations.

Rayleigh scattering For size parameters lower than 0.2 Rayleigh scattering can be assumed. The efficiency of scattering can be quantified by the scattering coefficient β_s that is inverse proportional to the wavelength to the power of four:

$$\beta_s \propto \lambda^{-4} \tag{2.17}$$

Consequently, the shorter the wavelength of the incident wave, the higher the scattering efficiency of the molecule. This phenomenon is responsible for the blue color of the clear sky. The directional dependency of the scattering is described by the phase function.

The Rayleigh phase function is symmetrical to scattering angle Θ:

$$P_R(\theta) = \frac{3}{4}(1 + cos^2\Theta) \ . \tag{2.18}$$

As a consequence, the same amount of radiation is scattered to the forward direction and to the backward-direction (see Figure 2.6).

Mie scattering Scattering on spherical particles, that have the same dimension of the incident wavelength ($0.2 < x < 2000$), can be explained by the Mie-theory (Mie 1908). In this regime the phase function is wavelength dependent and has a strong forward peak. Figure 2.6 shows an example of a realistic phase function of a mixture of dust particles with Log-normal size distribution with center at r = 1 µm at a wavelength of 800 nm. There is a nearly inverted linear relationship between Mie-scattering coefficients and the wavelength of the incident wave:

$$\beta_S \propto \lambda^{-A} \quad A \in [0.5, ..., 2.0] \tag{2.19}$$

Due to this relationship clouds appear gray, because the scatter efficiency is similar for each wavelength.

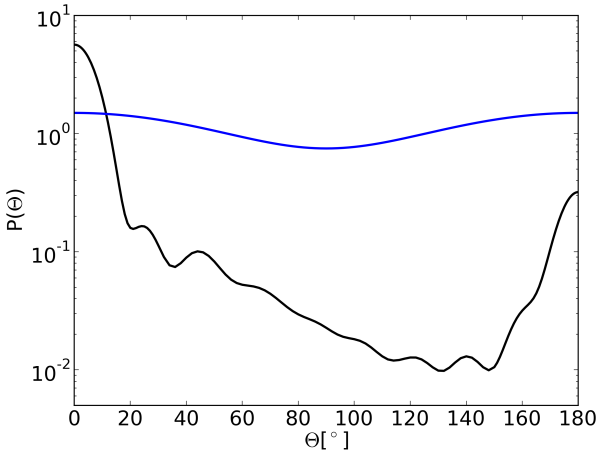

FIGURE 2.6: Examples of phase functions, normalized to 1; Blue: Rayleigh phase function; black: example of the Mie-phase-function of dust particles (Log-normal size-distribution with center at r = 1 μm and λ = 800 nm)

For clear skies, the constitution of aerosols is important for satellite remote sensing. One can divide aerosols in 4 main classes: Black carbon (originating from burning of organic matter), sulphates (e.g. from anthropogenic precursors or volcanic eruptions like sulphur), sea salt (from sea spray), and mineral dust (e.g. from deserts). Although dominated by the local source, in the real atmosphere there is always a mixture of aerosols. For example maritime aerosol contains mainly sea salt but can also include components of black carbon and dust. One important aerosol property is the single scattering albedo (SSA) ω_0 that quantifies the scattering efficiency compared against

total extinction efficiency:

$$\omega_0 = \frac{\beta_s}{\beta_s + \beta_a} \tag{2.20}$$

Usually, particles in an air mass are very heterogeneous in SSA, sizes, and shape. For radiative transfer simulations it is therefore necessary to consider the size-distribution of a mixture of particles with different optical properties.

Surface reflectance

The reflectance of the surface is one of the most important parameters in the remote sensing in the VIS to NIR. Two dominant processes are responsible for the reflectivity of the surface: Absorption and reflection. The amount of absorption of a surface depends on the material. Usually water bodies absorb 90 % of the sun light that reaches the surface, whereas snow covered land areas absorb only 10 % of the radiation. The remaining portion of light is reflected back diffusely. The directional dependency of the reflected radiation is described by the Bidirectional Reflection Distribution Function (BRDF). The intensity ($I^{\uparrow}$) of the radiation that was reflected by the surface is a function of the BRDF (ρ) and the incident flux of radiation:

$$I^{\uparrow}(\theta_r, \phi_r, \lambda) = \rho(\theta_i, \theta_r, \phi_i, \phi_r)\ F^{\downarrow}(\lambda) \tag{2.21}$$

For a surface that is reflecting equally in all directions (Lambertian reflector) the upward flux of radiation $F^{\uparrow}$, that is the integral of $I^{\uparrow}$ over the whole half space, can be derived by:

$$F^{\uparrow}(\lambda) = \pi\ I^{\uparrow}(\theta_r, \phi_r, \lambda) \tag{2.22}$$

Combining equation 2.21 and 2.22 we can define the surface albedo α on an Lambertian reflector:

$$\alpha(\lambda) = \frac{F^{\uparrow}(\lambda)}{F^{\downarrow}(\lambda)} \stackrel{!}{=} \pi \cdot \rho \tag{2.23}$$

2.3 Radiative transfer model

Most of the passive remote sensing algorithms are based on radiative transfer simulations. There are numerous radiative transfer models varying in their functionalities. The aim of each model is a simulation of radiative properties with accuracies that are sufficient for the individual task and with minimal computational expense.

In this thesis the radiative transfer model Matrix Operator Method Model (MOMO) was used that has been developed over a few decades now and has been updated recently to longwave radiation (Doppler *et al.* 2014a, Fell and Fischer 2001, Fischer and Grassl 1984). MOMO is a one-dimensional model with a coupled ocean-atmosphere system. Upward and downward radiative fluxes and radiances on the borders of the before-hand defined vertical layers can be derived for selectable zenith- and azimuth-angles in the wavelength range between 0.2 µm and 100 µm, covering the solar and terrestrial spectrum. In the

model, the Matrix Operator Method is used (Grant and Hunt 1969, Plass *et al.* 1973, Twomey *et al.* 1966), which is a numerical approach for the monochromatic computation of the radiative transfer in a scattering atmosphere. The atmosphere is divided into predefined layers. These again are divided into elementary layers where single-scattering can be assumed. The transmission, reflection and source term are derived for each of the sub-layers. Subsequently, the identical sub-layers are combined with the doubling algorithm in order to obtain the radiative properties of the entire layer. The adding algorithm analogously combines the radiative properties of the non-identical layers. For each predefined layer the optical thickness and the scattering properties such as the phase function of the mixture of scatterers and the extinction coefficient are required. In this work, scattering properties of the aerosols were calculated using a Mie code based on (Wiscombe 1980). The refractive properties of the aerosols and the natural mixture of the different components where extracted from Hess *et al.* (1998). The information of the gas absorption was extracted from the HITRAN data base (Rothman *et al.* 2010) that contains information about the position, intensity and width of the absorption lines of all gases that are present in the atmosphere. In order to reduce the computational effort of the high number of absorption lines in a line-by-line approach (Clough *et al.* 2005), a k-distribution method is applied. The procedure groups the absorption coefficients into bins of similar absorption strength. Subsequently, the radiative transfer simulation is performed for each bin and is combined afterwards, weighted by their contribution to the simulated band. Dependent on the demanded accuracy of the calculated optical thickness, the computational effort is reduced significantly (see the algorithm description in Chapter 3) for detailed information on the k-distribution method).

2.4 Ground based observations of total column water vapour

There are several ways to obtain the TCWV from ground. With Microwave Radiometers (MWR), Radiosondes, receivers of the Global Navigation Satellite System (GNSS), sun photometers e.g. Aerosol Robotic Network (AERONET) and LIDAR one can derive the TCWV. On one hand, there are disadvantages of low coverage of ground based observations especially over the oceans and the continental areas of Africa and central Asia. On the other hand, important advantages are high temporal resolution that serve investigations of the daily cycle of TCWV and the fact that stations are low in cost and can be repaired, calibrated and replaced, in particular for GNSS. In the following, three types of ground based observations are presented that where used in this thesis.

GNSS

The GNSS is designed for the exact determination of the position of a receiver and for the navigation purposes. The framework consists of multiple satellites on different orbital planes at around 20000 km height. This constellation allows that at least four satellites are coincidently visible over the horizon on every location at any time, which

is necessary for the exact three-dimensional positioning. GNSS satellites broadcast continuously signals on two carrier frequencies (1.57 GHz and 1.227 GHz). Satellite specific codes are modulated onto these frequencies that carry information such as the orbital parameters and time corrections. There are several methods to derive TCWV from GNSS measurements (e.g. Dick *et al.* (2001), Wang *et al.* (2007)), but the principle goes back to (Bevis *et al.* 1992). In the following, a brief overview of the general functionality of the procedure is given. The GNSS receiver on the ground is simulating the same signal as the satellites. The comparison of the detector signal and the satellite signal reveals a phase delay that is introduced by the time that the signal required to travel from satellite to the receiver. This time can be converted to the distance (range) between receiver and satellite. However, apart from inaccuracies in the clocks of satellite and receiver, there are several influences that introduce a bias to the range: The ionospheric delay due to the refractivity of the ionosphere, the hydrostatic delay due to the polarizability of the electrical neutral molecules and the wet delay resulting from the permanent dipole moment of the water vapour molecule. The ionospheric delay can be eliminated with straightforward procedures using linear combinations of the phases of the carrier frequencies. The hydrostatic delay can be approximated with empirical models that are mainly dependent on the surface pressure at the location of the receiver. The wet delay carries information of the TCWV. After correcting for the ionospheric delay and accounting for the elevation angle of the satellites with sophisticated mapping functions, the Zenith Total Delay (ZTD) can be derived. Subsequently, the hydrostatic delay is approximated with auxiliary data (the pressure and temperature at the location) and corrected for the viewing angle of the satellite, resulting in the Zenith Hydrostatic Delay (ZHD). Subtracting the ZHD from ZTD gives the Zenith Wet Delay (ZWD) that is transformed into the TCWV overlaying the receiver. There are several sources of errors e.g. in the approximation of the ionospheric and hydrostatic delays as well as technical and station specific characteristics. Nevertheless, the general accuracy of the TCWV derived from GNSS is around 1 mm–2 mm (Ning *et al.* 2015). Additionally, the fact that the viewing geometry is always slant, going through air layers that are not directly overhead, includes information about the water vapour of the surroundings. This feature has to be included in the interpretation of the GNSS TCWV data.

MWR

Ground based microwave radiometers can provide measurements of column-integrated amounts of water vapour and liquid water. The instruments used for the data set applied in this thesis detect microwave emissions of air molecules in the atmosphere at two frequencies, one sensitive to water vapour at 23.8 GHz and one mainly sensitive to liquid water at 31.4 GHz. A physical approach, meaning the comparison of the measured to simulated emissions, is straightforward due to the fact that the observation background is the known cosmic background temperature. High accuracies in TCWV of about 0.3 mm can also be achieved with a statistical retrieval algorithms that use location-dependent and monthly derived linear regression coefficients (Cadeddu *et al.* 2013, Turner *et al.* 2003, 2007).

Radiosonde

Radiosondes have been collecting data for nearly a century now and are still very important for the weather prediction. Radiosondes, launched from globally distributed stations, measure temperature, humidity and wind during the rise to about 20 km height. This vertically resolved information is crucial for studies on the upper troposphere. The integration of humidity, measured by the sondes, reveals that the TCWV, as nearly all water vapour is situated below that height. The measurements are performed with sensors that use a temperature- or humidity-dependent material in between a capacitor. The intensity and direction of the wind in a certain height is obtained from the drift of the radiosonde that in turn is monitored by GNSS tracking. Although the instruments have been developed and improved over the decades, there are error sources in the determination of the relative humidity (rH) profile e.g. a measurement error of the rH sensor that is sensitive to very low temperatures, calibration differences between the radiosonde stations etc. (Turner *et al.* 2003). In order to meet accuracy requirements of the climate observing community, the Global Climate Observing System (GCOS) established the GCOS Upper Air Reference Network (GRUAN) (Seidel *et al.* 2009). This network of a subset of global radiosonde stations operationally monitors and corrects radiosonde data for all known errors and omits data with high uncertainties (Dirksen *et al.* 2014).

Chapter 3

Universal TCWV retrieval

3.1 Introduction

As explained in detail in Chapter 1, the observation of long and consistent time series of TCWV is very important not only for climate monitoring. Again, the remote sensing of TCWV with radiance measurements in the NIR can provide high spatial resolutions with high accuracies. Currently, the longest time series of measurements of imaging spectrometer is provided by MODIS (since 2000 for Terra and since 2002 for Aqua) and is still ongoing. Unfortunately, the contact to ENVISAT equipped with MERIS, the European pendant to MODIS, was lost in April 2012, providing nearly 10 years of data. The following mission, OLCI on Sentinel-3 has been launched at February 16, 2016 leaving a gap of nearly 4 years. Also, in the future more instruments that measure radiance in the NIR will be launched, mainly initiated by the European remote sensing community (EUMETSAT and ESA), such as MetImage, Sentinel-2, Enmap, and Meteosat Third Generation (MTG). The geostationary MTG will provide measurements on high temporal resolution up to 5 minutes and will consequently enable the analysis of the daily cycle of TCWV for a large section of the Earth (see Chapter 5 for further information of future instruments). Despite the fact that the spectral settings, including channel number and location in the water vapour absorption band, are different for all the sensors, they all can contribute to the constitution of a long time series of TCWV. In order to provide the consistency of the remote sensing procedure, a universal TCWV retrieval has been implemented that can be adapted to all sensors that measure radiance in the $\rho\sigma\tau$-water vapour absorption band. The role-model is the method established by Lindstrot *et al.* (2012). The 1D-VAR procedure, based on differential absorption technique, derives TCWV for cloud-free scenes with uncertainty estimates on a pixel basis. The retrieval accounts for multiple scattering on atmospheric particles.

Recently, the procedure has been adapted to MODIS measurements in Diedrich *et al.* (2015). Additionally, the MERIS retrieval has been updated and improved and is now capable to retrieve TCWV over water surfaces. Comparisons to ground based measurements of TCWV revealed small differences that are presumably connected to instrument

Table 3.1: Position and widths of five NIR bands (original MODIS design specification) used for the TCWV retrieval (Xiong and Barnes 2006).

MODIS band	position [nm]	width [nm]	SNR
2	865	40	201
5	1240	20	74
17	905	30	167
18	936	10	57
19	940	50	250

calibration issues. Subsequently, the forward operator was designed to use pre-calculated coefficients that correct for these deviations. In the following the theoretical basis, concept and the architecture of the retrieval is presented. Additionally, results of extensive validation over land using independent ground based observations are presented. The water processor is still under development. Nevertheless, first evaluation studies were performed. The description in the following sections is partly based on Diedrich *et al.* (2015).

3.2 Space borne multi spectral sensors

The Moderate Resolution Imaging Spectroradiometer (MODIS)

MODIS was designed to provide global measurements of the Earth's cloud cover, radiation budget and thus to monitor processes in the ocean on land, and in the lower atmosphere. MODIS is a 36-band scanning radiometer covering the spectral range between 0.4 µm and 14.4 µm and with a spatial resolution between 250 m to 1 km depending on the band. It is mounted on both polar orbiting EOS (Earth Observing System) platforms Terra (morning transit: 10:30 am) and Aqua (afternoon transit: 1:30 pm). A two sided paddle-wheel mirror scans in a field of view of 110 degrees and with the swath of 2330 km. Consequently, global coverage can be provided in two days. MODIS bands are located on four separate focal plane assembles (FPAs) depending to their spectral positions and aligned in cross-track direction. Detectors of each spectral band are aligned in the along-track direction. Ten detectors, each with slight differences of their relative spectral response, scan the Earth simultaneously with a nadir spatial resolution of 1 km x 1 km per pixel in the NIR. Five bands in the NIR region between 0.8 µm and 1.3 µm are used for the TCWV retrieval (Table 3.1 and Figure 3.1). The bands 2 and 5 (865 nm and 1240 nm) are located in regions with few water vapour absorption features and are usually used for the remote sensing of vegetation and clouds. In the TCWV retrieval, these bands are used to estimate the surface reflectance in the $\rho\sigma\tau$-band. Bands 17, 18, 19 (905 nm, 936 nm, 940 nm) are water vapour absorption bands, with different strength of absorption. Absorption is more pronounced in band 18 and is therefore still sensitive to small TCWV values, while the weak absorption band 17 is sensitive to high TCVW values without being saturated.

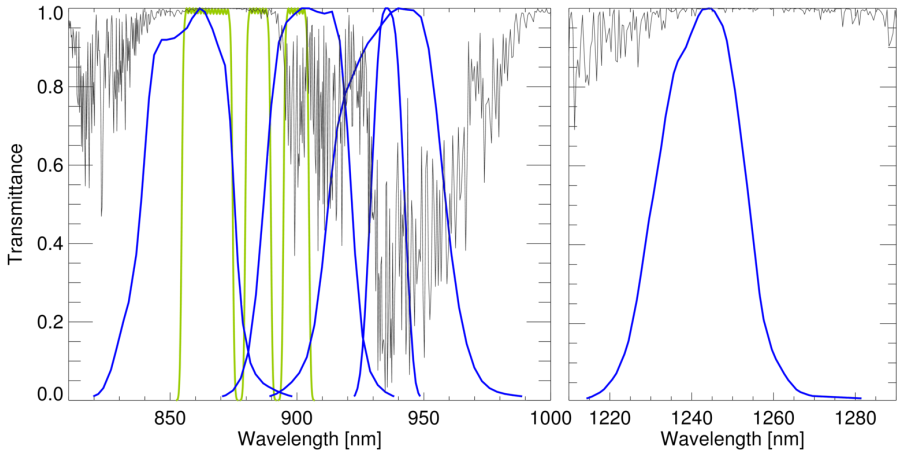

FIGURE 3.1: Simulated total atmospheric Transmittance due to water vapour in the NIR (absorption coefficients from HITRAN-database (Rothman *et al.* 2010); black curve) and actual relative response function of the five used MODIS Aqua bands (blue curves) and MERIS bands (green curves).

TABLE 3.2: Position and widths of MERIS bands in the NIR used for the TCWV retrieval (Rast *et al.* 1999).

MERIS band	center wavelength [nm]	width [nm]
13	865	20
14	885	10
15	900	10

The Medium Resolution Imaging Spectrometer (MERIS)

MERIS was primarily designed for ocean colour observations. However, MERIS measurements were used for numerous land applications over the years as well as for retrievals of atmospheric composition such as TCWV. MERIS is a medium-spectral resolution imaging spectrometer that operates in the reflective solar spectral range (390 nm–1040 nm) (Rast *et al.* 1999). The instrument scans the Earth in 15 spectral bands with five identical cameras using the "push broom" method over a field of view of 68.5 ° equivalent to 1150 km. The spatial resolution at nadir is 260 m x 290 m in "full resolution" mode. In the regular operation mode, the spatial resolution is reduced to 1x1 km ("reduced resolution" mode). The band widths and central wavelengths are listed in Table 3.2 and the relative response functions are plotted in Figure 3.1. The central wavelengths of the sensor vary across the field of view by up to 1.5 nm depending on the channel (Bourg *et al.* 2008).

3.3 Retrieval

The retrieval is based on the differential absorption technique (Gao *et al.* (1993); Bartsch *et al.* (1996); Albert *et al.* (2001); Albert *et al.* (2005)). The basic principle of the method is the comparison of the measured radiance in an absorption band to a close-by band with no or few water vapour absorption features. This retrieval compares simulated to measured radiances in the absorption band. It is based on a radiative transfer simulations that are stored in look-up-tables (LUTs). This can be achieved because of a convenient parametrisation of the forward model, explained in the following. The radiative transfer simulations were performed with MOMO that is described in detail in Chapter 2.

Forward Model

Taking into account the descriptions of Chapter 2, the radiance measured on TOA (L_{TOA}) for a certain channel (λ), viewing geometry (θ_i, θ_r) and the relative azimuth angle ϕ (that is difference between the viewing and sun azimuth angle $\phi_i - \phi_r$) is dependent on:

- the solar incoming flux corrected for the sun zenith angle $S_0 \cdot cos(\theta_i)$
- the surface reflectance $\rho(\lambda, \theta_i, \theta_r, \phi)$
- the two way transmittance $t(\lambda)$ of the atmosphere including downward and upward branch
- the atmospheric path radiance L_{path} that is the diffuse radiation originating from the scattering atmosphere due to incoming radiation
- the atmospheric spherical albedo S of the atmosphere for isotropic light entering it from the surface

The forward operator accounts for the surface reflectance and the total atmospheric transmittance including gaseous absorption and scattering on aerosols. The latter includes the diffuse contributions S and L_{path}.

Atmospheric Transmittance

The transmittance of the atmosphere t is parametrized in the following way:

$$t = t_{\mathrm{noscat}} \cdot f \ , \tag{3.1}$$

where t_{noscat} accounts for the absorption only due to water vapour and f is the scattering factor that corrects for the influence of scattering on aerosols and molecules. The separate consideration of absorbing and scattering processes in the forward model allows

an straightforward adaption to new sensor setups and reduces computational costs due to reduction in dimensions of the individual LUTs.

f is defined as the ratio of total atmospheric transmittance including scattering t and t_{noscat}. f is usually larger than one, as atmospheric scattering causes a shortening of the average photon path length and reduces the amount of TCWV, by preventing a fraction of photons from traversing the humid lower troposphere. The scattering factor increases above dark surfaces, as the majority of photons are reflected by atmospheric scatterers and thus do not travel through the whole vertical column of water vapour. Consequently, f is mostly dependent on aerosol loading, type and vertical distribution. Figure 3.2 illustrates the sensitivities of f, derived from radiative transfer simulations. In the top left panel of Figure 3.2 f is shown as a function of the albedo at 900 nm (presuming a lambertian reflector) and the aerosol optical thickness (AOT) of an aerosol layer with exponential increase from 1000 m to the bottom, for a fixed water vapour value of 42.4 mm, sun zenith angle of 37°. It reveals that for bright surfaces (albedo greater than 0.5), the scattering factor is around one, but increases significantly with higher AOT and lower albedo. On the top right panel the dependency of f to the AOT and the air mass factor (AMF) is shown. The AMF (μ) is defined as:

$$\mu = 1/\cos(\theta_i) + 1/\cos(\theta_r) \ . \tag{3.2}$$

Here, a TCWV of 28.6 mm, an albedo of 0.2 and a relative azimuth of 0° is preconditioned. The plot represents the increase of f with higher AMF due to the longer path through the atmosphere that increases in turn the likelihood of scattering. The increase of f with higher AOT is more recognisable for AMFs greater than 4. On the lower left panel of Figure 3.2 f is shown as a function of albedo and AMF at a TCWV of 28.6 mm. f is increasing significantly with higher AMF and decreases with higher surface albedo, following the findings from the upper two plots. At the bottom right plot of Figure 3.2 the influence of the hight of the aerosol layer is addressed. Here, the increase of the scattering factor due to a higher aerosol layer around 6000 m with 500 m thickness in percent is shown as a function of AMF and albedo while keeping the TCWV, viewing zenith, AOT and relative azimuth constant. It reveals that for bright surfaces and low AMF, the influence of the scale hight of the aerosol layer is negligible. For realistic conditions for the remote sensing over land (albedo around 0.2 and sun zenith angles below 70°) the increase of f is only 1 % to 2 %. However, for dark surfaces the scale height of the aerosol layer is a significant contributor to the scattering factor.

The transmittance operator, that determines t_{noscat}, uses stored absorption coefficients that were calculated from the HITRAN2008 line database (Rothman *et al.* 2010), using the AER LBLRTM code (Clough *et al.* 2005) and an advanced k-distribution method (Bennartz and Fischer 2000), based on re-sorting the large number of quasi-monochromatic spectral intervals within each band with respect to their optical depth and combining them to a significantly lower number of pseudo-spectral intervals. The optical depths in each pseudo-spectral interval i for a value of WV^* are then obtained from simply multiplying the stored coefficients accordingly: $\tau_i^* = \tau_i \ \frac{WV^*}{WV_0}$, where WV_0 is the reference

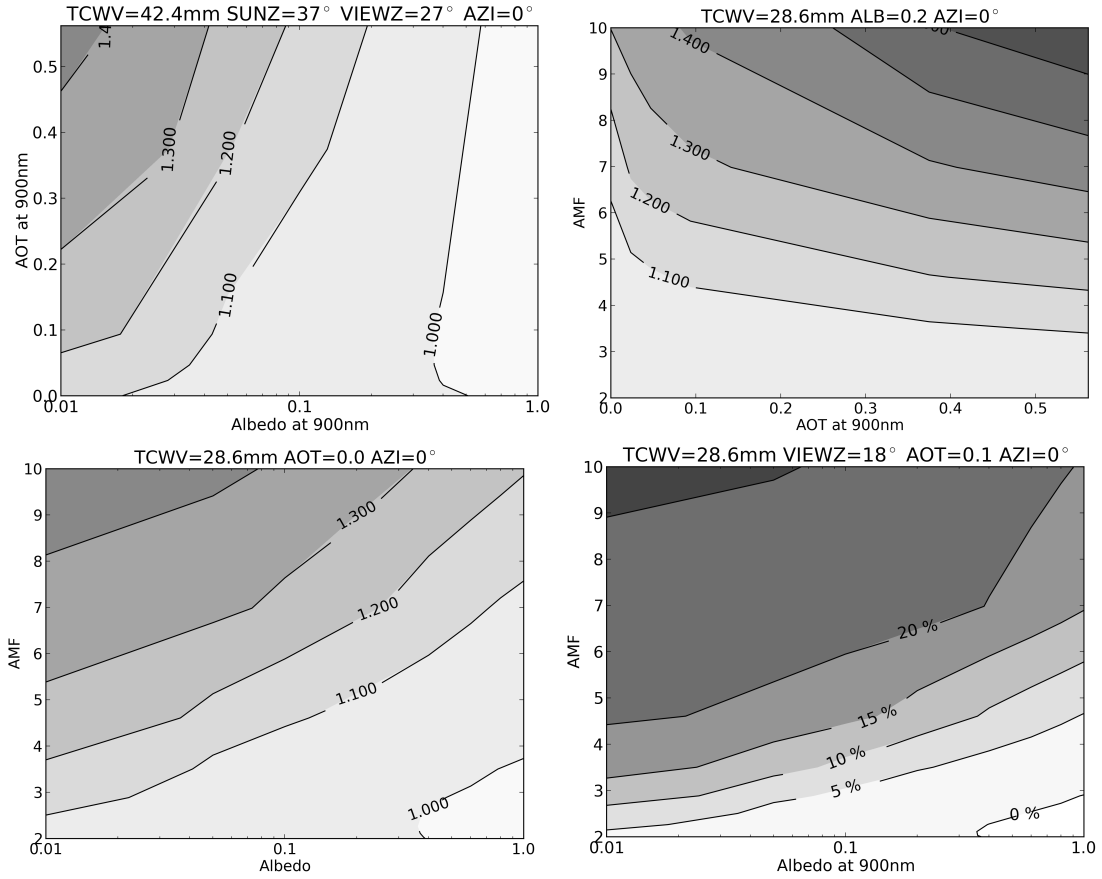

FIGURE 3.2: Sensitivity studies of scattering factor f as a function of AOT and albedo (top left), of AOT and air mass factor (AMF) (top right), and albedo and AMF (bottom left). Bottom right panel shows the difference of f in % between an atmosphere with a presumed aerosol layer at the upper troposphere and one at the lower troposphere as a function of albedo and AMF. The values of all remaining relevant parameters that where kept constant (SUNZ: sun zenith; VIEWZ: viewing zenith; AZI: relative azimuth; ALB: albedo at 900 nm) are shown on the top of each plot. Find detailed description in the text.

TCWV value. In detail, for a given observing geometry and TCWV, the transmittance t_{noscat} in each band is modeled by:

1. calculating the optical depth τ_{ij} for each pseudo-spectral interval i and vertical layer j for the desired value of TCWV,

2. calculating the transmittance in each pseudo-spectral interval from the sum of the optical depth along the line of sight following Equation 2.5 and

3. subsequently summing up all transmittance values with respect to the weights w_i associated to the pseudo- spectral intervals:

$$t_{\text{noscat}} = \sum_{i=1}^{\#intervals} w_i \cdot \exp\left(- \sum_{j=1}^{\#layers} \tau_{ij} \cdot \mu \right) . \tag{3.3}$$

The optical depth values τ_{ij} are stored in look-up tables for 6 standard temperature profiles (McClatchey *et al.* 1972) and 27 different pressure levels. The transmittance is calculated for the four look-up table grid points closest to the actual surface pressure and temperature of the considered scene, hereby assuming that the surface temperature is highly correlated with the actual vertical temperature profile (Lindstrot and Preusker 2012). Finally, the t_{noscat} is stored in LUTs for each absorption band.

The scattering factor f was derived beforehand by radiative transfer simulations and stored to LUTs for wavelength intervals of 1 nm for the wavelength interval between 870 and 1200 nm. For that, the atmospheric transmittance including scattering $t*$ was derived from total TOA-radiance L^* and TOA-radiance L_0^* presuming a TCWV value of 0 mm:

$$t^* = \frac{L^*}{L_0^*} . \tag{3.4}$$

The dependence of f to the temperature profile and the pressure can be neglected. Consequently, the radiative transfer simulations were only performed for a fixed temperature, humidity and pressure profile (U.S.-standard profile). However, as the scattering in a water vapour absorption band is also depended on the absorption itself, the TCWV was varied. Furthermore, f was obtained for different aerosol optical thickness but for a fixed aerosol profile and size distribution.

Generally, the radiative transfer simulations were performed separately for land and ocean surfaces. First, the optical aerosol properties (SSA, phase function, scattering efficiency) were selected and extracted from Hess *et al.* (1998). For water surfaces, a maritime aerosol mixture and for land surfaces a continental mixture, presuming an aerosol layer with an exponential increase of the Aerosol Optical Thickness (AOT) from 1000 m to the bottom for both cases. Secondly, the surface reflectance was treated differently for the two surface types, explained in detail in the following.

Surface reflectance

The surface reflectance in the absorption band is derived in two steps. First, the surface reflectance in the two neighbouring window bands is obtained. Afterwards, these are either inter- or extrapolated onto the absorption band, depending on the band setup of the sensor requiring at least two close by window bands. The determination of the surface reflectances in the window bands depends on the surface type. Over land and coastal- and inland waters, these are part of the state vector and are optimized in the optimal estimation procedure. For open ocean surfaces (so called case 1 waters) the water leaving radiance is zero around 900 nm. However, the roughness of the ocean, triggered by the wind at the ocean surface, introduces reflection features that can result in reflectances up to 100 % (in sun glint areas). Besides the salinity and the temperature of the ocean (Hollstein and Fischer 2012), the wind-speed at the ocean surface is the

dominant parameter for the BRDF of the reflectance of the ocean (Cox and Munk 1954). Consequently, the wind-speed is part of the state-vector for the ocean case. A sub-procedure that is based on LUTs derives the surface reflectance in the window bands after the empirical formulas of Cox and Munk (1954) and Koepke (1985) at every retrieval step. Secondly, the surface reflectance in the absorption band is determined by linear inter- or extrapolation from the window bands, depending on the position of the bands. For the majority of surface types, a linear relationship of the surface reflectance and wavelength can be assumed in the wavelength range between 850 nm and 1000 nm.

Inversion

Remote sensing algorithms often derive the wanted properties from a set of measurements, e.g. radiance measurements in different channels. In order to retrieve the selected quantities, the difference between simulated and measured radiances are iteratively optimised. As discussed in the previous sections, the clear-sky radiance in the NIR measured at the TOA is influenced by a number of parameters, such as surface reflectance, aerosol optical thickness /-height/-type and water vapour. In order to derive the TCWV, either all other quantities have to be known, or are optimised iteratively until the difference between simulations and measurements is sufficient small. For the universal TCWV retrieval, the inversion was performed with an Optimal Estimation (OE) method after (Rodgers 2000). An overview is given hereafter. The forward model (here: radiative transfer model) depends on various variables and environmental parameters. In most cases, it is not a bijective function that converts measurements into state vector variables since it is also dependent on other parameters. The forward model F is thus a function of the state vector $\vec{x}$ and a set of known parameters $\vec{b}$. The measured radiances $\vec{y}$ can be modelled with the following relationship:

$$\vec{y} = \mathbf{F}(\vec{x}, \vec{b}) + \vec{\epsilon}\,, \tag{3.5}$$

where $\vec{\epsilon}$ is the error vector that contains contributions from errors of:

- the measurements (calibration errors and noise of the instrument)
- the forward model (the assumptions that have been made in the RTM)
- the forward model parameters (uncertainties of the background information)

These contributions can be condensed in the error covariance matrix $\mathbf{S}_e$. Rodgers (2000) presented an effective way to account for these uncertainties in the OE. The method is based on the Bayes' theorem and assumes Gaussian distributions of the errors. Besides the error propagation it includes also the possibility to constrain possible solutions with a priori knowledge. Following the OE approach the inversion can be performed by iteratively minimising the cost function J by changing the state vector:

$$J(\vec{x}) = (\vec{y} - \mathbf{F}(\vec{x}))^T \mathbf{S}_e^{-1} (\vec{y} - \mathbf{F}(\vec{x})) + (\vec{x} - \vec{x}_a)^T \mathbf{S}_a^{-1} (\vec{x} - \vec{x}_a)\ , \tag{3.6}$$

where $\vec{x_a}$ is the a priori state vector and $\mathbf{S}_a$ is the a priori error covariance matrix. Basically, the differences between forward model and measurement and state vector and a priori state vector are weighted by their uncertainties. For example, if the knowledge about the a priori information is reliable (low uncertainties), but the measurements have high uncertainties, the weight of the right part is larger than the left part of the equation. The goal of the iteration process is to find the state with the highest probability given a measurement and an a priori state. The following convergence criterion is applied:

$$(\vec{x}_i - \vec{x}_{i+1})^T \ \hat{\mathbf{S}}^{-1} \ (\vec{x}_i - \vec{x}_{i+1}) < \epsilon_x \cdot n \ , \tag{3.7}$$

The left part of the relation represents the variance of the difference between the states of two iteration steps (i and $i+1$). ϵ_x represents the threshold in fraction of the variance (in the retrieval 1 % is applied ($\epsilon_x = 0.01$)). n is the number of dimensions of the state vector. $\hat{\mathbf{S}}$ represents the retrieval error covariance matrix that is derived by:

$$\hat{\mathbf{S}} = (\mathbf{S}_a^{-1} + \mathbf{K}_i^T \ \mathbf{S}_e^{-1} \ \mathbf{K}_i)^{-1} \ . \tag{3.8}$$

$\mathbf{K}_i$ is the forward model Jacobian that is the partial derivative of the forward model to the state at the iteration step i, $\mathbf{S}_a$ is the a priori error covariance matrix and $\mathbf{S}_e$ is the measurement error covariance matrix. The retrieval returns the current state vector if either the convergence criterion or the predefined maximal number of iterations is reached.

In the following, details of the state vector for the two surface types are given. For both surface types, the TCWV a priori information was extracted from reanalysis data (ERA-Interim; Dee *et al.* (2011)).

Land Surfaces

Over land, the state vector contains the TCWV and the surface reflectance in the window bands. For the estimation of the atmospheric transmittance, a priori information are required:

- The surface pressure is derived from converting land elevation to pressure using the GTOPO30 digital elevation model (GTOPO 1996).
- The surface temperature is extracted from reanalysis data (ERA-Interim).
- If no information about the AOT is available, a climatological standard value is taken (AOT_{550}=0.1).

The prior surface reflectance (ρ_{prior}) is derived from the TOA reflectance by: $\rho_{\mathrm{prior}} = L_{\mathrm{TOA}}/\pi$.

Ocean Surfaces

Over ocean surfaces, the state-vector contains the TCWV, wind-speed and AOT because these are the parameters that influence the TOA radiance where the wind-speed is representative of the surface reflectance. For a priori wind-speed, reanalysis data is extracted (ERA-Interim) and for the AOT a standard value of 0.1 is used.

Uncertainty Estimate

After the iteration procedure the retrieval uncertainty is calculated, taking into account the following sources of uncertainty:

- residual model error ($\vec{x}_i - \vec{x}_{i+1}$)
- measurement uncertainty (SNR) ($\mathbf{S}_e$)
- model parameter uncertainties

For the model parameter uncertainties the following contributions are assembled in the model parameter error covariance matrix $\mathbf{S}_b$:

- uncertainty of the aerosol optical depth
- uncertainty due to the missing information of the aerosol type and scale height.
- uncertainty of the surface pressure and -temperature
- uncertainty due to the missing information about the true temperature profile
- uncertainty due to the estimation of the surface reflectance and its spectral slope

For the quantification of the error of the retrieved state, $\mathbf{S}_b$ is first propagated into the measurement space using the standard error propagation and added to the measurement error covariance matrix:

$$\mathbf{S}_y = \mathbf{S}_e + \mathbf{K}_b^T \; \mathbf{S}_b \; \mathbf{K}_b \tag{3.9}$$

where $\mathbf{K}_b$ is the model parameter Jacobian. The resulting error covariance matrix $\mathbf{S_y}$ is then propagated into the state vector space using the forward model Jacobian $\mathbf{K}$. The resulting error covariance matrix $\hat{\mathbf{S}}$ is a direct measure of uncertainty in state vector space (equivalent to Equation 3.8):

$$\hat{\mathbf{S}} = (\mathbf{S}_a^{-1} + \mathbf{K}^T \mathbf{S}_y^{-1} \mathbf{K})^{-1}. \tag{3.10}$$

In the following, it is described, how the individual error sources are estimated. As outlined in Section 3.3, the scattering factor f is affected most by the surface reflectance, aerosol height and aerosol optical thickness. For each of these parameters a perturbed f^* is calculated from the LUTs, by perturbing the input accordingly. There is no

information available about the aerosol scale height and the type (size distribution, absorption and scattering properties). Consequently, a f^* was calculated presuming an aerosol layer at 6000 m with a thickness of 500 m. Additionally, a f^* was calculated from simulations supposing another aerosol model. These f^* were used to derive perturbed TOA-radiances L^*_{TOA}. Finally, the difference $(\Delta L)^2 = (L_{\mathrm{TOA}} - L^*_{TOA})^2$ is added to the measurement error variance $\mathbf{S}_e$.
The error due to differences between the simulation- and the real temperature and humidity profile was evaluated by comparing the atmospheric transmittances derived from a real example radiosonde profile to transmittance using the standard profiles. This effect introduces an error to the pure absorption transmittance of around 2 % (depending on the band). To estimate the uncertainty due to the surface background information, the surface temperature was shifted by 5 K and the surface pressure was perturbed by 20 hPa and subsequently committed to the transmittance forward operator. Again, $(\Delta L)^2$ is calculated and added to $\mathbf{S}_e$.
The spectral dependency of the surface reflectance is parametrized with the Normalized Differenced Vegetation Index (NDVI) (for further details see Lindstrot *et al.* (2012)). The uncertainties of the surface reflectance range from 0.5 % to 1.2 %. Similar to the approach pictured above, a perturbed TOA radiance is calculated and the resulting deviation is contributed to $\mathbf{S}_e$.

3.4 Validation data sets

The universal TCWV retrieval applied to MODIS and MERIS and validated against different TCWV data sets such as space borne and ground based MicroWave Radiometer (MWR) data, Global Navigation Satellite System (GNSS) water vapour monitoring data, radiosonde data, and Aerosol Robotic Network (AERONET) sun photometer data. Figure 3.3 presents the spatial distribution of stations of the ground based observations.

ARM microwave radiometer

A TCWV data set of ground based MWR (software version 4.13) for the years between 2002 and 2012 was used for the assessment of the TCWV retrieval. Three ARM (Atmospheric Radiation Measurement) sites where considered: North Slope of Alaska (NSA), Southern Great Plains (SGP), Tropical Western Pacific (TWP). MWR instruments measure the radiation emitted by the atmospheric water vapour and liquid water at frequencies of 23.8 GHz and 31.4 GHz (Turner *et al.* 2007). The background of the measurement is the cosmic background temperature. Consequently, it is one of the most accurate methods to determine the TCWV from ground. The uncertainty of the measured TCWV from MWR is expected to be in the range of 0.3 mm (Turner *et al.* 2003). This data set was used to calculate the correction coefficients (see Section 3.5).

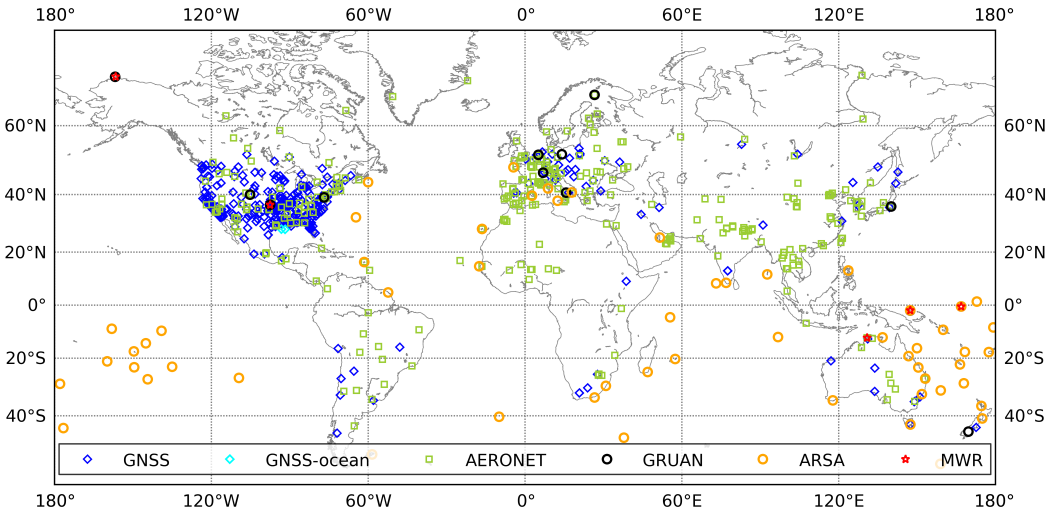

FIGURE 3.3: Location of stations of the used ground based validations data sets.

Ground based GNSS

The global two-hourly GNSS TCWV data set is based on three different resources: the International GNSS Service (IGS), U.S. SuomiNet (UCAR/COSMIC) products and Japanese GEONET data (Wang *et al.* (2007)). Data from 942 stations for the years between 2003 and 2011 were extracted. The uncertainty of this data is not precisely stated by the authors but a similar data set provides an accuracy of 1 mm to 2 mm (Ning *et al.* 2015).

Additionally, for the validation over ocean surfaces we used TCWV GNSS data from two offshore oil platforms in the Gulf of Mexico (John Forsythe, personal communication). The one-hourly data set ranges from July 2010 to December 2011.

Radiosonde

The uncertainty of TCWV derived from most operational radiosondes ranges between 1 % and 10 % for the most radiosonde stations (Turner *et al.* 2003). Over land surfaces this uncertainty is exceeds the sought accuracy of the universal TCWV retrieval. Consequently, a TCWV data set provided from the GCOS (Global Climate Observing System) Reference Upper-Air Network (GRUAN), was used to compare to the MODIS TCWV retrieval for the years 2007 to 2014. GRUAN is devoted to quality assessment and providing data with high accuracies in the measured profiles of relative humidity and temperature. The data set (version 002) contains 14 stations (Dirksen *et al.* 2014, Immler *et al.* 2010). Antón *et al.* (2015) provides an uncertainty of TCWV of about 3.5 %. For the validation of TCWV from MERIS over ocean surfaces, radiosonde data from coastal stations of the Analyzed RadioSoundings Archive (ARSA) has been extracted from the Integrated Global Radiosonde Archive (IGRA) data set (Durre *et al.*

2006) for the years 2002 to 2012. The representative ground coverage of the radiosonde measurement can be up to 50 km in the boundary layer (Seidel *et al.* 2011). Consequently, at coastal stations, integrated radiosonde measurements carry information of TCWV over coastal waters.

AERONET sun photometer

A global set of TCWV values from AERONET sun photometer measurements from the years between 2003 and 2014 was used for validation (Direct Sun Algorithm version 2)[1] (Bruegge *et al.* 1992, Reagan *et al.* 1986). Pérez-Ramírez *et al.* (2014) stated that the retrieval produces TCWV values with a consistent dry bias of approximately 5 %–6 % and an estimated uncertainty of 12 %–15 %.

Space borne microwave radiometer on ENVISAT

ENVISAT carried a nadir-looking Microwave Radiometer (MWR) that measured emitted radiation from the Earth and atmosphere in two channels at 23.8 GHz and 36.5 GHz that allows for the simultaneous retrieval of TCWV and cloud liquid water path over water surfaces. As part of the ESA Long Term Data Preservation (LTDP) framework, the ERS/Envisat MWR Recalibration and Water Vapour Thematic Data Record Generation (EMiR)[2] project group published a MWR TCWV data set that has been derived from a recalibrated and bias corrected ERS-1, ERS-2 and ENVISAT MWR L1-data (Ralf Bennartz, personal communication). MWR TCWV data was collocated with MERIS TCWV for the validation above ocean surfaces for the whole MERIS time series (2002 to 2012).

3.5 Correction coefficients

In order to evaluate the performance of the retrieval, TCWV values from MODIS and MERIS were compared to ground based MWR measurements. These data are considered as ground truth and compared to retrieved TCWV from collocated MODIS and MERIS scenes. In order to assess the behaviour of each MODIS band, an one-band-retrieval has been established that iteratively fits the simulated to the measured radiance for one band using the same architecture and look-up tables as the three-band algorithm.

The comparison of MODIS derived TCWV against MWR data reveals different deviations in each band (Figure 3.4). On the one hand, the data sets correlate linearly and the spreading is low. On the other hand, there are significant differences, with a maximum of about 10 % in case of the retrieval using only band 17 and a minimum in case of the band 19 of about 1 %. The retrieval underestimates the TCWV for every

[1] downloaded from: `http://aeronet.gsfc.nasa.gov`

[2] `www.esa-mwr.org`

channel. These deviations accumulate to a dry bias in the three-band MODIS retrieval of 0.7 mm.

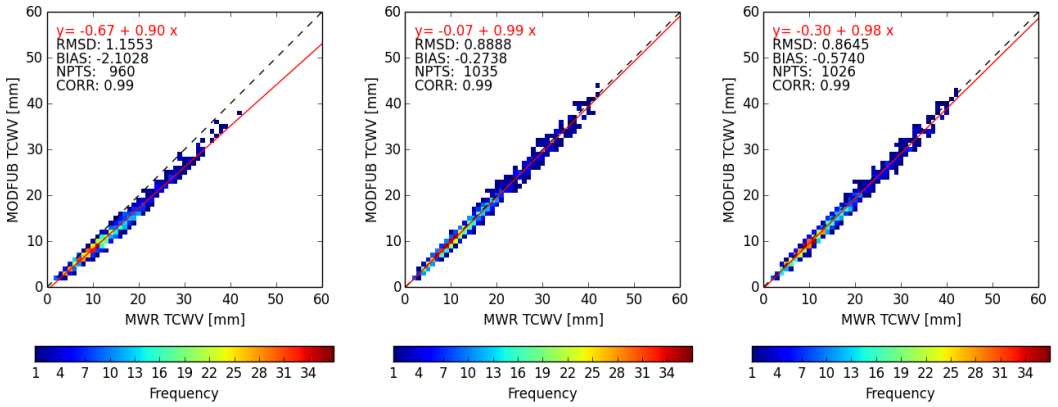

FIGURE 3.4: Normalized frequencies of occurrence for comparisons of TCWV from the MODIS retrieval only using one absorption band against MWR TCWV data in mm (left: band 17, center: band 18, right: band 19); see text for detailed description.

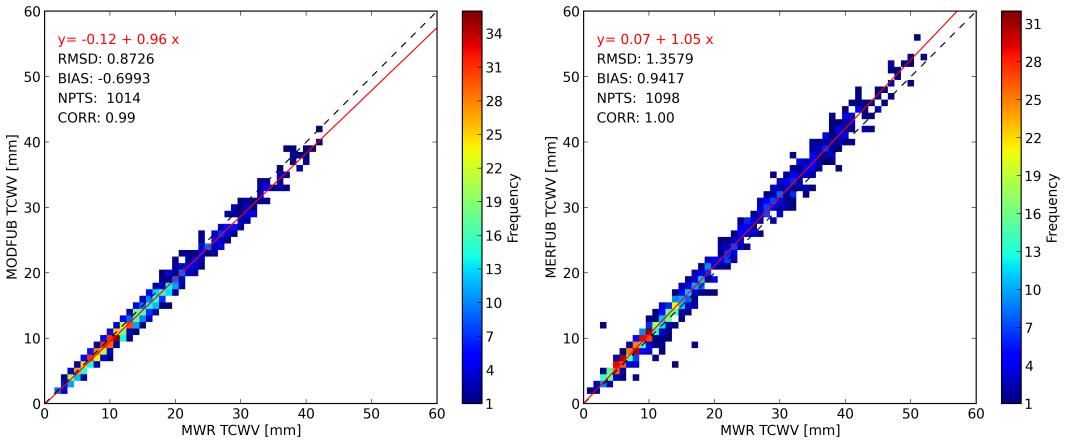

FIGURE 3.5: Normalized frequencies of occurrence for comparisons of the TCWV from the uncorrected MODIS retrieval on the left and uncorrected MERIS-retrieval on the right against MWR TCWV data.

Reasons for the differences could be:

a) systematic errors of MWR

b) wrong spectral calibration of MODIS or MERIS bands

c) errors in the forward model.

First, the MWR data is very precise. Turner *et al.* (2003) quantified a measurement uncertainty of 0.3 mm and secondly a bias in the MWR data would introduce the same

TCWV shift to every band.
MODIS features a SpectroRadiometric Calibration Assembly (SRCA) that calibrates all bands on-orbit and keeps track of all radiometric changes and degradation of the optics (Xiong and Barnes 2006). Xie *et al.* (2006) stated an uncertainty of the central wavelength of maximal 0.1 nm for band 17. Nevertheless, the influence of a shifted central wavelength for all absorption bands was tested (not shown here). It turns out that the shifts that are necessary to cancel out the differences in the TCWV exceed by far the accuracy given by Xie *et al.* (2006).

Another source of the differences between simulated and measured radiances could be the forward operator of the retrieval. The values in the following discussion are only valid for the MODIS retrieval, but in general, is also applicable to the MERIS retrieval.

As presented in the previous section, the backbone of the forward operator is the determination of the atmospheric transmission due to water vapour absorption, t_{noscat}, and the the scattering factor f. The latter is primarily dependent on the surface reflectance which is sufficient constant for the validation data set. At the same time, aerosol properties such as AOT, scale height and aerosol type vary substantially over the year. First of all, this fact would not introduce a systematic bias but rather an increased spreading. Secondly, the sensitivities of AOT and scale height in respect to the simulated TCWV do not explain the deviations: Table 3.3 shows the influence of a doubled AOT, and Table 3.4 shows the influence of the aerosol scale height to the simulated TCWV for different surface reflectances. The error due to the different aerosol type is maximal about 0.5 % (not shown here). The sensitivities were calculated by deriving the difference of transmittance between an unperturbed and a perturbed AOT, and scale height, respectively. The difference in transmittance has been transformed into an equivalent TCWV value using a partial derivative of transmittance with respect to TCWV. Supplementary, Diedrich *et al.* (2013) stated the low impact of the AOT on the error of a TCWV retrieval. However, the scattering-absorption interaction can be over- or underestimated in the radiative transfer simulations. The other potential source of error could be the determination of the absorption coefficients. In this case either the database of absorption coefficients or the binning method could be wrong. Furthermore, a wrong representation of the water vapour continuum or the isotopes could explain the differences.

There is a 5 % wet bias for the MERIS retrieval in comparison to the MWR data (Figure 3.5). MERIS spectral calibration can be performed on-board. The issues concerning the differences between the central wavelengths of each camera and detector (spectral smile effect), stray-light effect, sensor degradation have been quantified in Bourg *et al.* (2008), Delwart *et al.* (2007). Here again, the influence of a shifted wavelength in the absorption band has been determined. Although the difference of the central wavelength between the MERIS cameras can be up to 1.5 nm, the necessary shift of the response functions exceeds this range.

TABLE 3.3: Influence of a doubled AOT to the simulated TCWV for different surface reflectances in units of TCWV (mm) for a MODIS retrieval using only one absorption band.

surface reflectance	band 17	band 18	band 19
0.1	-0.110	-0.344	-0.255
0.3	0.153	0.018	0.076
0.9	0.442	0.328	0.376

TABLE 3.4: Influence of the aerosol scale height to the simulated TCWV for different surface reflectances in units of TCWV (mm) for a MODIS retrieval using only one absorption band.

surface reflectance	band 17	band 18	band 19
0.1	-0.463	-1.035	-0.793
0.3	-0.017	-0.288	-0.172
0.9	0.279	0.074	0.153

In summary, the origin of the deficiency of the retrieval is not exactly known yet. Hence, we introduce correction coefficients in order to adjust the atmospheric transmittance t_{noscat} in the optical thickness space. The corrected transmittance t_{corr} is then calculated by:

$$t_{\mathrm{corr}} = exp(a + b \cdot ln(t_{\mathrm{noscat}})). \tag{3.11}$$

The coefficients a and b were obtained by optimizing the difference between simulated and measured atmospheric transmittance $(t_{\mathrm{corr}} - t_{\mathrm{meas}})$ using the MWR validation data set as a reference. The uncorrected transmittance t_{noscat} was calculated by the absorption forward operator taking viewing geometries from the sensor and the TCWV information from the corresponding MWR measurement. t_{meas} was derived by:

$$t_{\mathrm{meas}}(\lambda) = L_{\mathrm{meas}}(\lambda)/L_0(\lambda) \tag{3.12}$$

where L_{meas} is the measured radiance in the absorption band. L_0 is the radiance presuming no absorption of water vapour. It is derived from inter- or extrapolating the measured radiances (corrected for water vapour) in the window bands onto the position of the absorption band. For MODIS channel setup it is derived accordingly:

$$L_0(\lambda) = [(L_2/t_2 - L_5/t_5) \ / \ (\lambda_2 - \lambda_5)] \ \cdot \ (\lambda - \lambda_2) \ + L_2/t_2. \tag{3.13}$$

This was done for each band and for MODIS-*Aqua* and MODIS-*Terra* and MERIS, respectively. Figure 3.6 shows the flow of the correction and validation process for the MODIS retrieval. As a consequence, the difference to ground based measurements is reduced to a minimum, as can be seen in the next section.

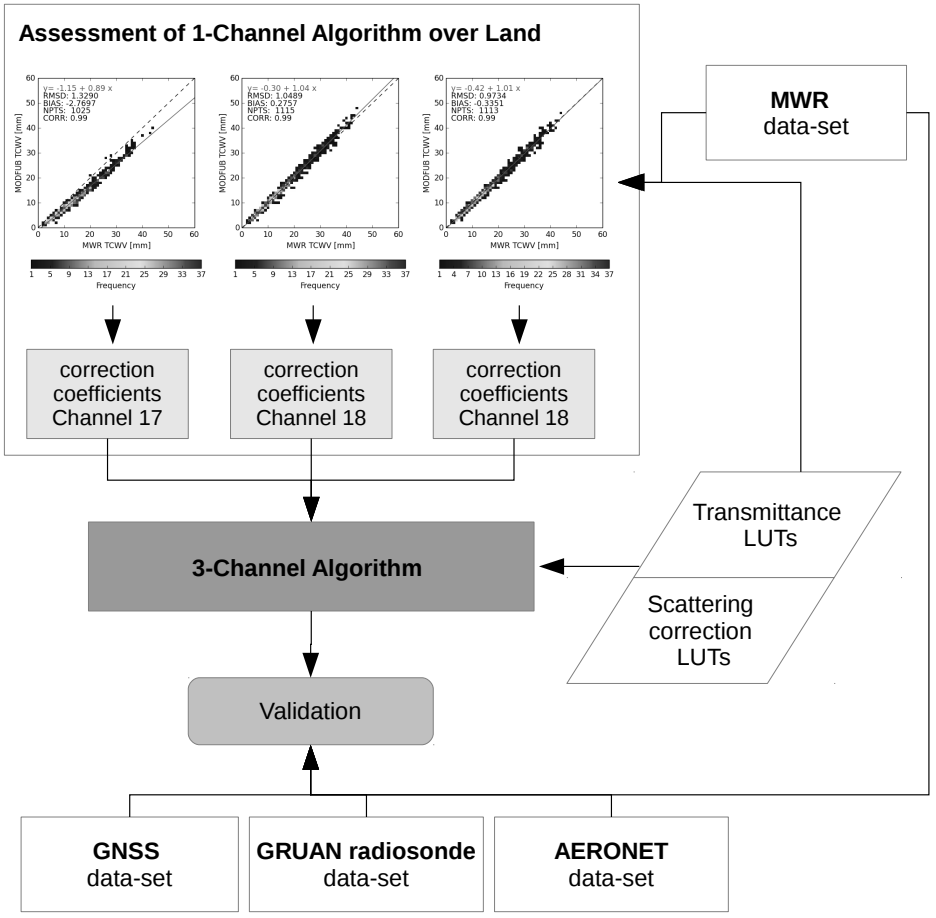

FIGURE 3.6: Flowchart of the correction and validation process for the MODIS retrieval.

3.6 Validation with ground based data sets over land surfaces

Validation of the MODIS TCWV retrieval

The validation results are shown in Figure 3.7. In every plot, the normalized relative frequency of occurrence is shown with high occurrences plotted in red to yellow, and low occurrences in dark blue. In the top left corner of each plot the offset and slope of the linear regression, the bias corrected root mean square deviation (RMSD), the bias, the correlation coefficient, and the sample size as number of points (NPTS) are given.
The operational MODIS cloud-mask from the MOD35-L2-product was used to filter out cloudy and cloud contaminated pixels. Only pixels with bit-value "100% clear"

were used for the study. MODIS measurements were spatially averaged over an area of 20 km x 20 km (20x20 pixel) to account for e.g. the radiosonde displacement, and the time gap between satellite overpass and ground based measurement. The location of all considered sites from different data sets are displayed in Figure 3.3.

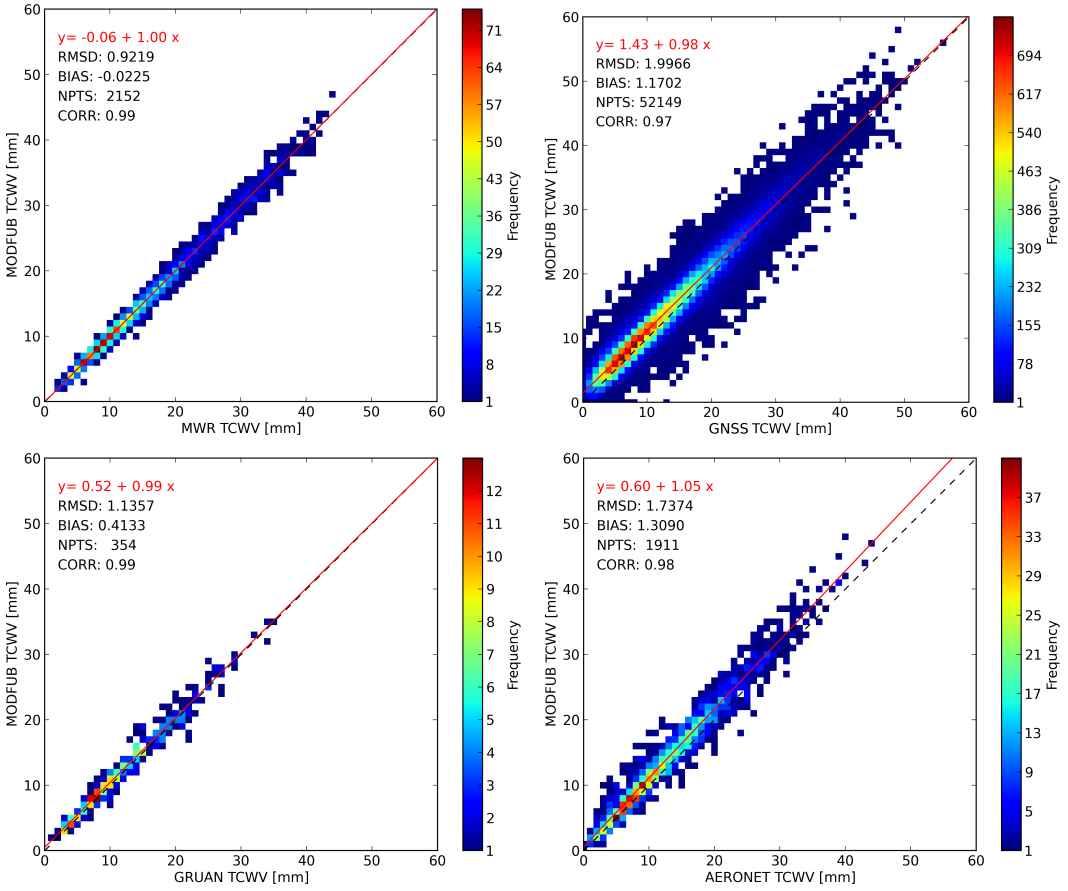

FIGURE 3.7: Normalized frequencies of occurrence for the comparison of the MODIS TCWV-retrieval against ground based microwave radiometers (upper left panel) and global ground based GNSS-data (upper right panel), GRUAN Radiosonde data (lower left Panel) and AERONET sun photometer data (lower right Panel). For detailed description see text.

ARM MWR

In the top left panel of Figure 3.7 the comparison of the corrected retrieval for both MODIS Aqua and Terra and the MWR is shown, where only cases with 90 % valid MODIS pixels were considered to exclude the influences of clouds. As expected in Section 3.5, both data sets show almost perfect agreement, although the number of samples is relatively low due to cloud contamination at the NSA and TWP sites. Thus, SGP provides 70 % of the number of points. Nevertheless, the data set is representative

for global observations because dry northern, wet tropical and mid latitude conditions are contained.

ground based GNSS

We extracted GNSS-TCWV-data for all collocations with a time difference less than one hour between measurement and satellite overpass. Only cases with 90 % valid MODIS pixels were considered. The upper right panel of Figure 3.7 shows the comparison between GNSS- and MODIS-Aqua and Terra derived TCWV values. Although the filtering was very strict, the number of samples is still very high due to the high number of GNSS-stations. The bias is -1.2 mm, the RMSD is 1.9 mm indicating a slight overestimation of MODIS TCWV values, especially for the high number of dry cases.

Figure 3.8 shows the bias between the two data sets for each station on a world map. Generally, the biases are between 1 and 2 mm. The majority of stations has a negative bias meaning that MODIS TCWV values are larger on average than the GNSS values, which corresponds to Figure 3.7. Although GNSS stations are not distributed equally over the world, Figure 3.8 shows that there is no dependency of the location of the station and the bias, such as a dependency to latitude, altitude or distance to the ocean.

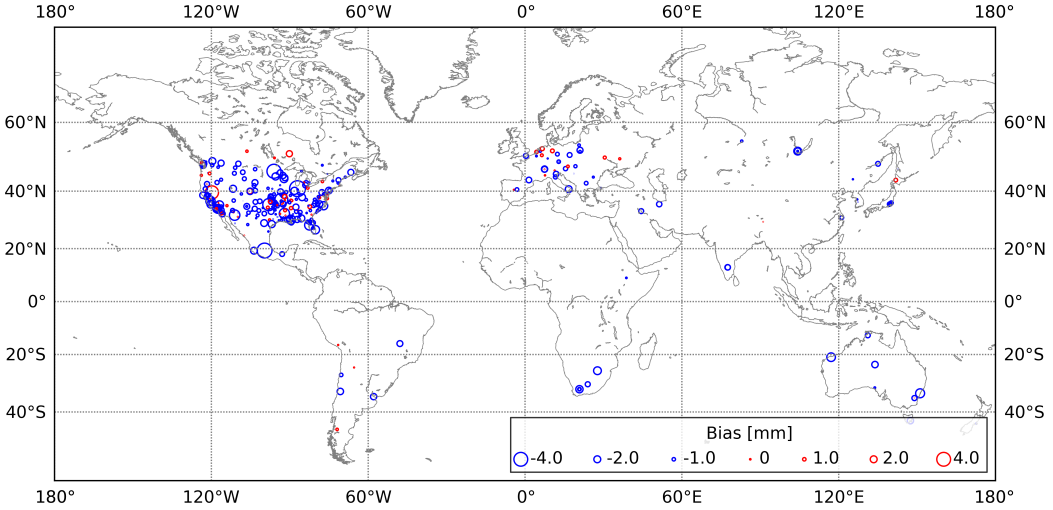

FIGURE 3.8: Map of the bias between MODIS TCWV values and GNSS TCWV in mm. Positive values (red circles) imply that TCWV values on that GNSS stations are generally larger than the MODIS TCWV values. Blue circles show station where the bias is negative.

GRUAN Radiosonde

In order to account for the displacement of the radiosonde during its ascent only cases with a time difference of maximum two hours between radiosonde and MODIS measurement were considered. In order to account for cloud contamination but also preserve a sufficient high number of data-points, only cases with less than 70 % valid MODIS pixel were rejected, resulting in 354 cases. The comparison of TCWV from MODIS Aqua and Terra and GRUAN reveals a very good agreement, a bias of -0.4 mm and a RMSD of 1.1 mm, shown in the lower left panel in Figure 3.7.

AERONET sun photometer

On the lower right panel of Figure 3.7 the comparison to the sun photometer measurements is shown. Only cases with 90 % cloud-free MODIS pixels are taken into account. The agreement between the data sets is very good because the spreading is in the range of the uncertainty of AERONET, although there is a small but significant wet bias. However, this is most likely due to the dry bias in the sun photometer data stated by Pérez-Ramírez *et al.* (2014).

Validation of the MERIS TCWV Retrieval

In order to evaluate the accuracy of the application to MERIS measurements and the derived correction coefficients, MERIS TCWV was also compared to ground based MWR and GNSS TCWV data. Figure 3.9 shows the comparison where only cases with 90 % cloud-free MERIS pixels were considered. The comparison to GRUAN TCWV could not be performed due to only a small number of cloud-free collocations. There is hardly any systematic difference to MWR TCWV and very small spreading. For the comparison to GNSS, the spreading is increased, similar to the MODIS retrieval. Here, a bias of 0.6 mm was derived.

Time Dependency

In order to study the temporal constancy of the accuracy of the retrieval the annual bias between the retrieved TCWV from MODIS and MERIS and GNSS / MWR was calculated as function of time (year) and plotted in Figure 3.10. In case of MWR, the time series ranges from 2003 to 2009 and from 2003 to 2011 for GNSS, respectively. The annual absolute difference between MWR and the TCWV retrieval output (upper panel) varies around 0 mm for all instruments and is constant over the years, considering the variation represented by the boxes and whiskers of around 2 mm. Due to the low number of coincidences, the number of cases per year ranges only between 50 and 150.

The GNSS data set provides ten times more cases (lower panel). Considering the large variance of around 5 mm, there is no annual dependency in comparison to GNSS values,

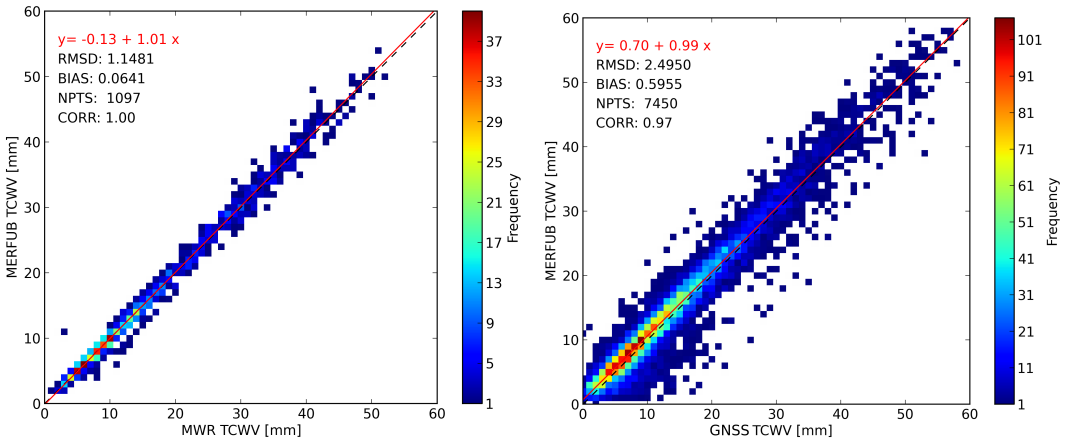

FIGURE 3.9: Normalized frequencies of occurrence for the comparison of the MERIS TCWV-retrieval against ground based microwave radiometers (left panel) and global ground based GNSS-data (right panel).

although the medians tend to be around -1 mm to -2 mm which is consistent with the negative bias in the scatterplot in Figure 3.7.

The large area of whiskers and the large number of outliers in the GNSS data is presumably due to some sources of error in the GNSS TCWV retrieval (see Chapter 2). However, the spreading is not time dependent. Generally, there is no significant difference between Modis Aqua and Terra and MERIS in both comparisons.

3.7 Comparison to operational MODIS L2-product over land surfaces

The MODIS L2-product (MOD05) from NASA (National Aeronautics and Space Administration) provides TCWV on a pixel basis from (Gao and Kaufman 2003). This operational product exists since 1999. Unfortunately, the accuracy of this product is limited and it has not been improved since then. Therefore, we validated the data with global ground based measurements for the first time. Figure 3.11 shows the comparison of MOD05 TCWV values to MWR and GNSS stations. The same cases as in Figure 3.7 were used for better comparison. It reveals that the operational algorithm overestimates the TCWV by about 20 % and the spreading (RMSD) is higher in comparison to the universal retrieval.

3.8 Evaluation of MERIS TCWV over ocean surfaces

The adaption of the universal TCWV retrieval to ocean surfaces has just recently been done. Consequently, extensive validation could not be performed yet. Although space

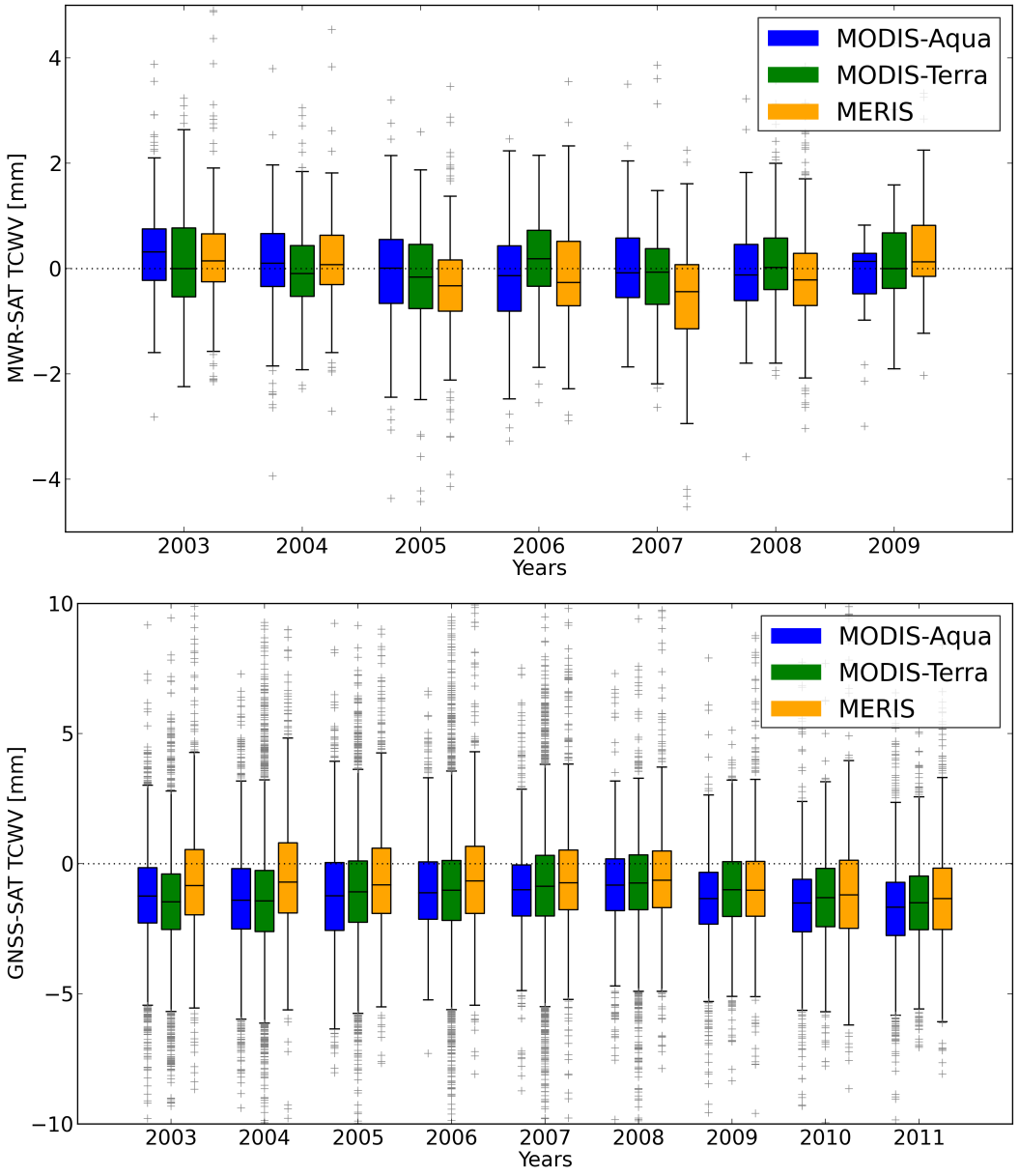

FIGURE 3.10: Boxplot of the annual bias in mm between TCWV retrieved from MODIS (blue boxes: Aqua, green boxes: Terra) and MERIS (orange boxes) and ground based measurements (upper panel: MWR, lower panel: GNSS); The range of the boxes indicate the interquartile range (IQR), containing 50 % of the data-points. Horizontal bars within the boxes show the median, vertical bars (whiskers) indicate the reach of approximately 95% of the data-points, and grey pluses show all outliers.

borne observations of TCWV over ocean are plenty, the collocation coincidences are rare. Only the MWR data set can provide a good comparison with no time-lag. However, the TCWV data set has not yet been validated extensively, for the same reason: Independent ground based observations over the ocean with high accuracy are sparse. Nevertheless, first results of the comparison to MERIS TCWV are presented in the following.

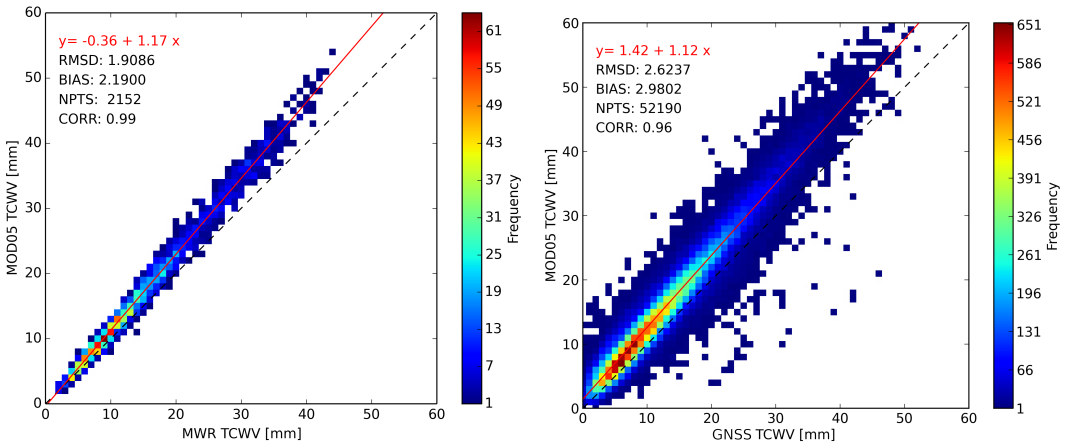

FIGURE 3.11: Normalized frequencies of occurrence for the comparison of the MODIS L2 TCWV product (MOD05) to MWR (left panel) and GNSS data (right panel).

EMiR MWR

TCWV over open ocean, derived from space borne observations from MWR on ENVISAT, were compared to MERIS omitting coastal regions and large lakes. Due to the footprint of around 20 km and the signals of the side-lobes of the MWR, MERIS TCWV was averaged over an area with a radius of 50 km for each MWR observation. Only cases with 90 % clear-sky pixels were considered in the comparison. Figure 3.12 shows the evaluation for all collocations in the MERIS time series (2002-2012). Although the correlation is very high with 0.97 and the RMSD is only 2.9 mm, there is a systematic wet bias of 3.8 mm. This can also be recognized in Figure 3.13, where the relative difference between MERIS and EMiR MWR TCWV in percent is presented on a 1°-grid as an average over the entire time series. Generally, TCWV from MERIS is higher than from EMiR MWR (indicated by red colors). White pixel indicate grid-cells with no collocations resulting from first, high cloud cover, in particular in the high latitudes and second, from a strict threshold that was set to the outcome of the cost function, excluding areas of low surface reflectivity at high latitudes. There are pixels with negative differences (blue pixels) at equatorial regions indicating an average underestimation of the MERIS TCWV. This could possibly result from undetected clouds (cirrus or thin low level clouds or aerosol layers). There is a stripe of no collocations close to the Date line, due to missing data in the EMiR data set.

ARSA radiosondes

The upper right panel in Figure 3.12 shows the comparison to TCWV from coastal radiosonde stations of the ARSA database. Cloud-free TCWV values over an area of 200 km were averaged and compared to the corresponding ARSA values if the scene has 70 % ocean pixels of which are also 70 % cloud-free. The first striking feature is the

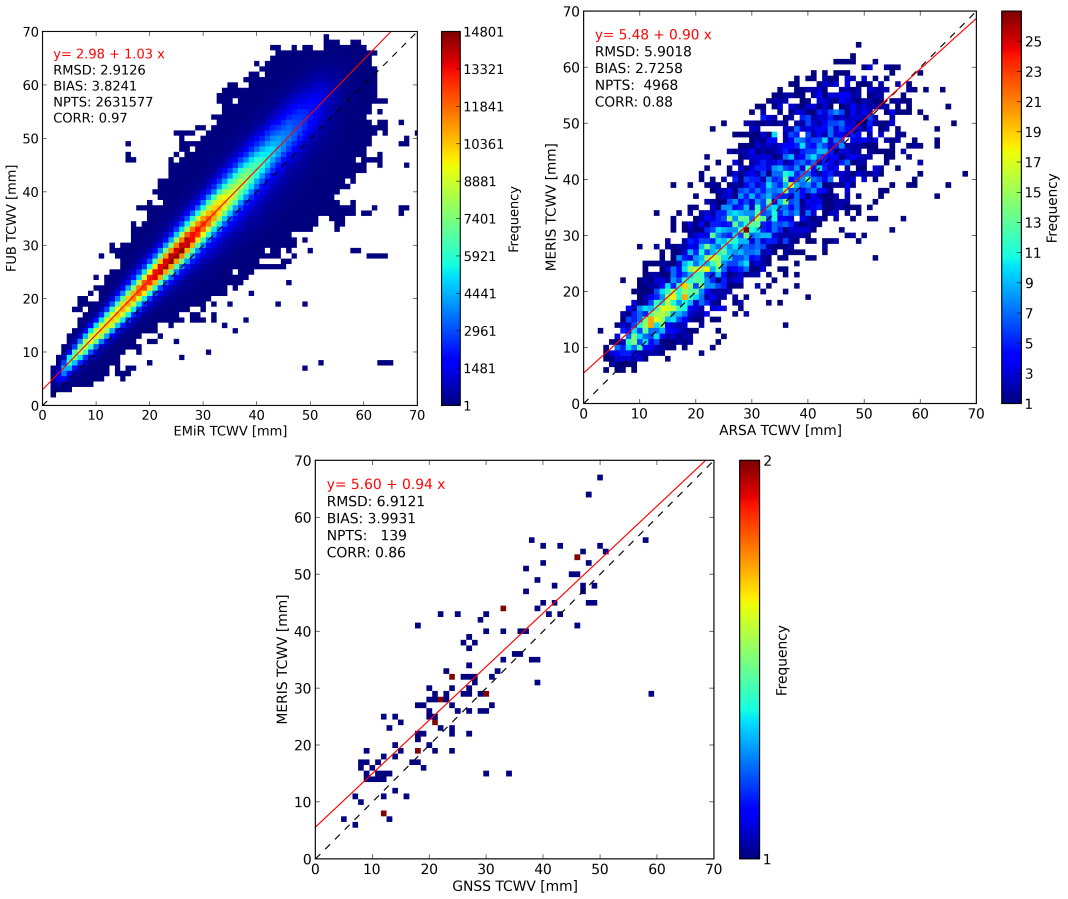

FIGURE 3.12: Normalized frequencies of occurrence for the comparison of the MERIS TCWV-retrieval against space borne MWR (upper left panel), ARSA radiosonde data (upper right panel) and GNSS-data from two offshore oil platforms. See text for detailed information.

large spreading, that is presumably due to the large averaging area and the maximal time difference between radiosonde launch and satellite overpass that was set to 3 hours. However, the correlation between both data sets is high with 0.88. There is a systematic offset of 2.7 mm, about 10 % that is in the range of the outcome of the comparison to EMiR MWR.

Offshore GNSS

Due to the fact, that data from only two offshore oil-platforms were available only for 1.5 years, the number of collocations in the comparison of GNSS TCWV and MERIS TCWV over the ocean is very low (see lower panel in Figure 3.12). For the MERIS TCWV only cases with 70 % cloud-free pixels were considered and the data was averaged over an area with a radius of 20 km. The comparison reveals again a systematic bias of 4 mm with a large RMSD of 7 mm.

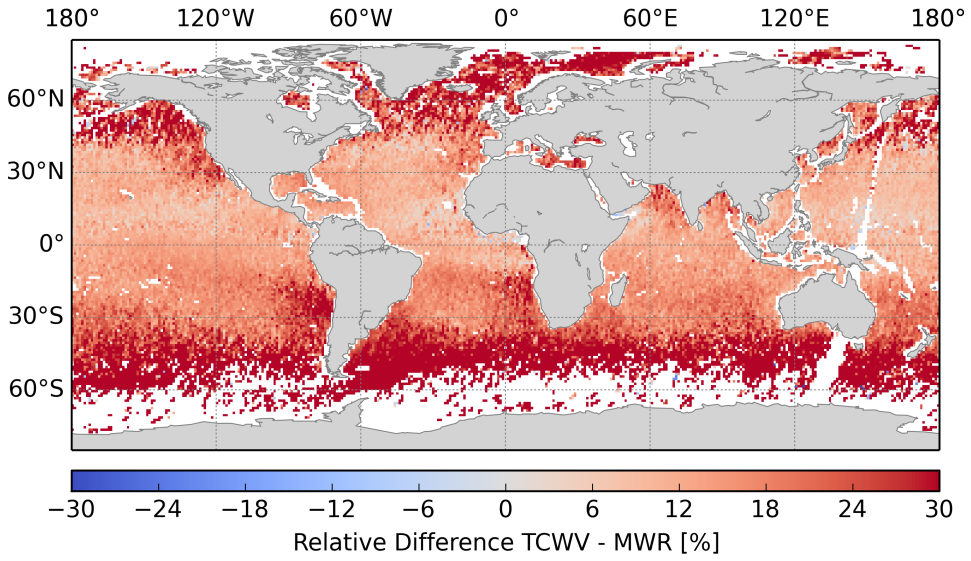

FIGURE 3.13: Difference between MERIS and EMiR MWR TCWV in % on a regular 1°-grid (all corresponding observations for each grid-cell were averaged for the whole ENVISAT time series (2002-2012).

3.9 Example of derived TCWV field

Figure 3.14 shows an example of a MERIS scene: On the left an RGB picture and on the right the corresponding retrieved TCWV. The sequence of the MERIS orbit from July 4, 2005 is about 1000 km x 1000 km wide and shows most parts of Madagascar on the left part of the scene. The right section contains only water surface (Indian Ocean) but is largely covered by clouds. The TCWV field shows a lot of typical features and local climatological characteristics:

- The height-dependency of TCWV can be observed by low TCWV values (indicated by dark purple and black colors) in the center of the island that shows elevations up to 2000 m.

- On the one hand, the south-west part of Madagascar is featured by dry and semi-arid areas. On the other hand, the eastern coastal area is dominated by tropical rainforest. This opposing characteristic is due to south-east trade winds that are dominating the weather in the dry season (May to October). Typically, the advected humid air is lifted on the east side of the central mountains. Subsequently, water vapour condenses that can be observed by convective clouds at the right part of the image, and falls out as precipitation. Consequently, most of the humidity remains on the east coast of the island. This characteristic can also be observed for the case in Figure 3.14. High TCWV values around 25 mm on the east coast (for the few cloud-free pixels) and low TCWV around 10 mm were obtained in the mainly cloud-free western part.

- Rivers are emphasized through TCWV values that are higher than the surrounding environment in the western part, presumably caused by enhanced evaporation due to the higher availability of water.

The homogeneous TCWV values of ocean and land areas at the north-west coast of Madagascar shows consistency between ocean and land processor. However, there are some pixels with higher TCWV values at coast boarders that are probably due to a wrong land-sea-mask. Here, the land processor was applied to ocean pixels or vice versa. Another frequent feature is visible at the top left part of the TCWV field. The boarder between two MERIS cameras is visible through a sharp vertical line of different TCWV values. This lining results from the different spectral calibration, in particular the different central wavelength of the detectors. The effect is stronger over the dark ocean than over land surfaces due to the decreased SNR.

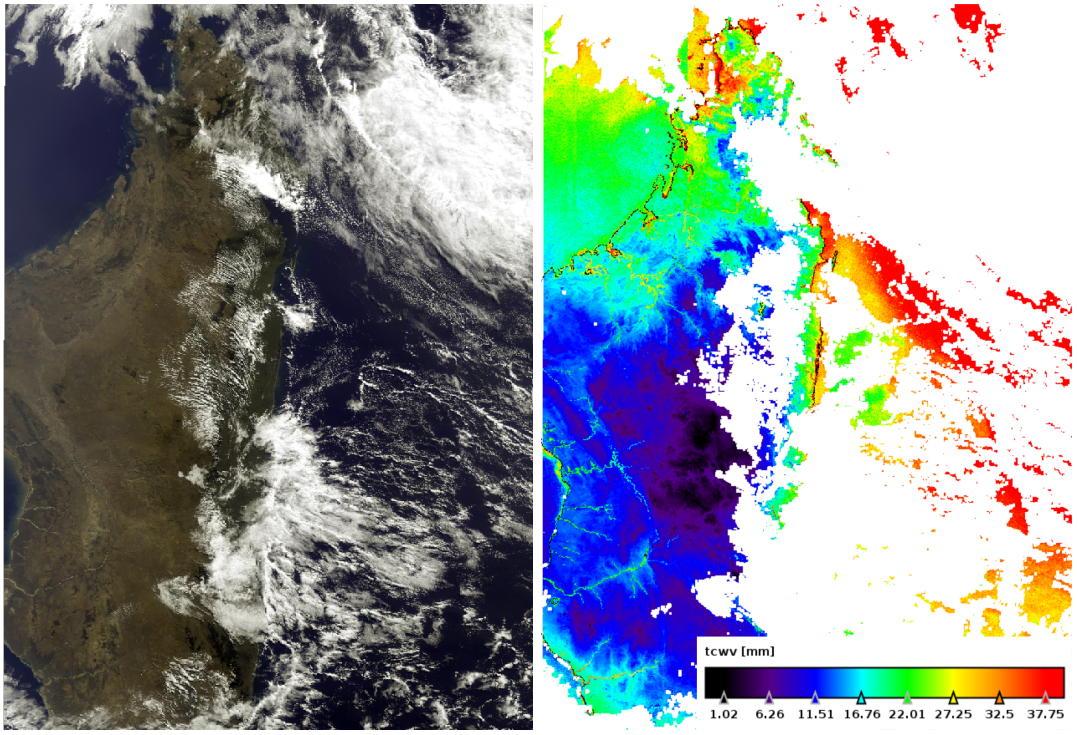

FIGURE 3.14: Left panel: RGB picture of a MERIS scene over Madagascar recorded on July 4, 2005, Right Panel: Corresponding derived TCWV in mm. The black line indicates the cost-line.

3.10 Application: Observing horizontal convective rolls

MERIS data in full resolution mode (260 m x 290 m at nadir) allows studies about the small-scale variability of boundary layer water vapour in relation with convective initiation. The case study on horizontal convective rolls shows that TCWV derived from

MERIS observations can give hints for locations of initiation of dry or moist convection over land. The case was found in the frame of my bachelor thesis[3], further investigated and published in Carbajal Henken *et al.* (2015). A summary is presented in the following.

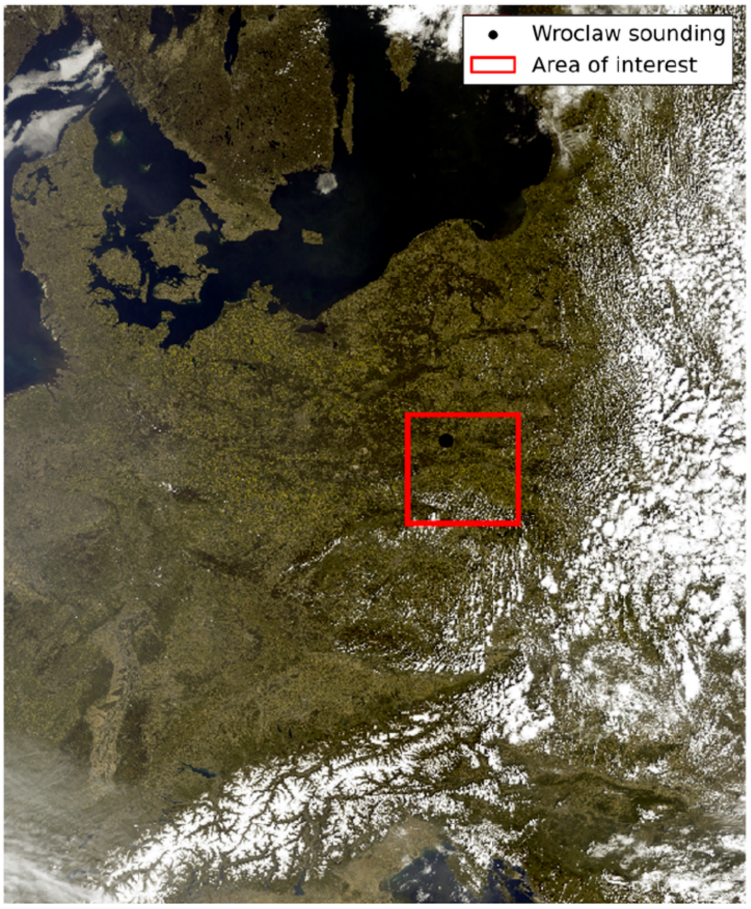

FIGURE 3.15: MERIS full-resolution RGB for the case study of horizontal convective rolls on 9 May 2008 at 09:42 UTC. The area in the red box is shown in Figure 3.17.

The case study focusses on an area in central Europe including southern Scandinavia, Germany, Poland and the Czech Republic on 9 May 2008. The terrain is fairly flat, and on this day meteorological conditions were present that benefit the development of horizontal convective rolls (HCRs). A blocking high pressure system dominated the general circulation and the weather in central Europe the days before and after. Figure 3.15 shows a MERIS RGB image of the ENVISAT overpass at 9:42 UTC. The TCWV field for the same segment is presented in Figure 3.16 as well as the boundary layer mean wind computed from ERA-Interim data. Three interesting features can be spotted in the TCWV field:

1. A clear minimum of TCWV is noticeable along a boundary ranging from the Baltic sea to Saxony, Germany that is moving to the west during the day.

[3]Diedrich (2009), "Untersuchung kleinräumiger Strukturen im Wasserdampffeld ", Freie Universität Berlin

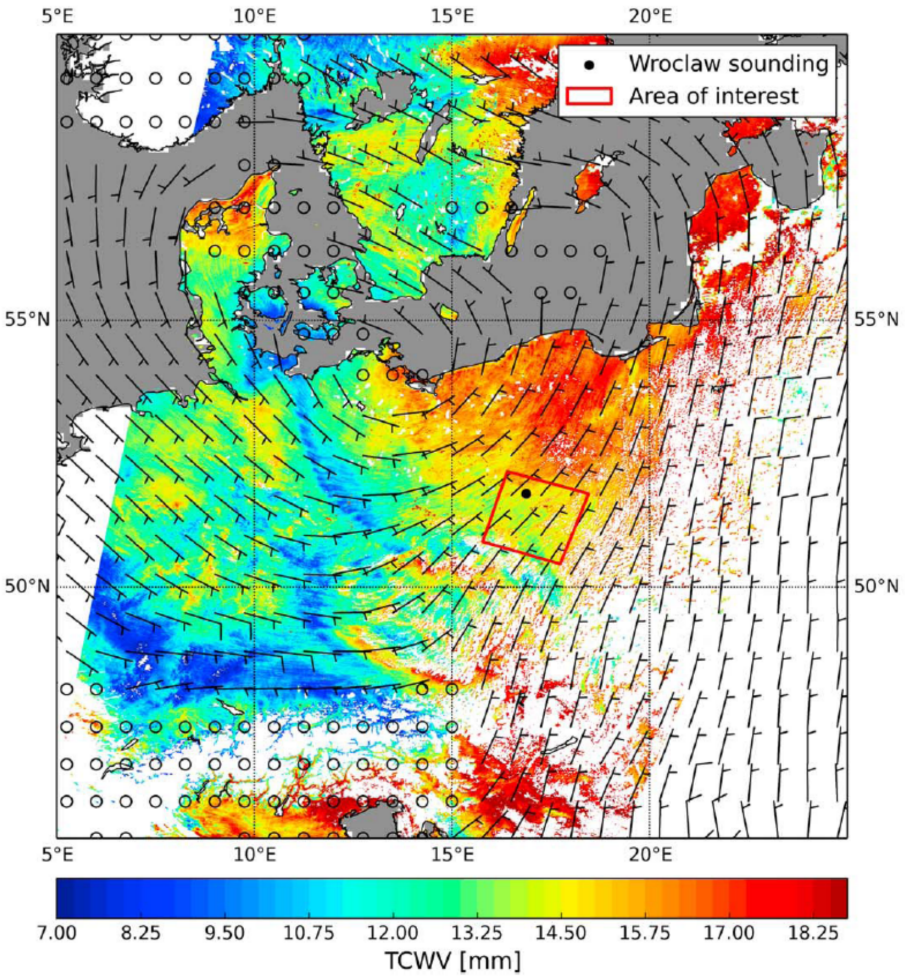

FIGURE 3.16: MERIS TCWV field overlayed with ERA-Interim wind barbs computed from the mean boundary layer wind field.

2. TCWV is increasing to the east, where clouds are present. Closer examination of these areas reveal that high TCWV values occur adjacent to cloudy pixels.

3. Parallel bands of alternating low and high TCWV values can be observed that appear aligned with the cloud streets and the mean boundary layer wind (also shown in Figure 3.17).

The last features indicates the presence of HCRs, which are organized convective structures in the shallow boundary layer and can occur regularly over both water and land surfaces. They are quasi two-dimensional counter-rotating air rolls, that cause horizontal small scale variation in moisture. Upward branches transport warm and moist air from the surface. Hence, these regions are associated with an increase in TCWV. Downward branched transport dry and cold air from above to the surface where low TCWV amounts occur. Over land, surface heating combined with turbulent movements in the boundary layer in a fairly steady wind (shear), often occurring in high pressure systems,

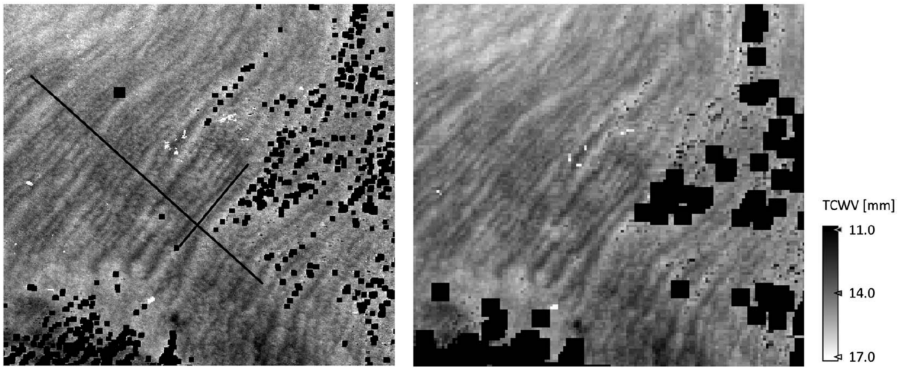

FIGURE 3.17: TCWV field for the area of interest as indicated by the red box in Figure 3.15. Left panel: MERIS full-resolution mode; right panel: MERIS reduced-resolution mode; black areas indicate cloudy regions for which no TCWV retrievals are performed.

field is favourable for the development of HCRs. They can be considered as boundary layer convergence zones that can trigger deep convection (Weckwerth 2000). HCRs are potentially related to environmental conditions and can be described quantitatively by their:

(1) orientation relative to the wind field in the boundary layer

(2) wavelength, which is the spacing between the rolls in the cross-roll direction

(3) aspect ratio, which is the ratio of roll wavelength to boundary layer depth

This quantitative description of HCRs can be performed with the MERIS full-resolution TCWV field combined with other data. Figure 3.17 shows the TCWV on full-resolution on the left and reduced–resolution on the right for a zoomed section in Figure 3.15 which has the size of approximately 160 km x 160 km. In both resolutions the banded structure of TCWV field can be observed. However, in full-resolution individual bands of high and low TCWV as well as the variability along the bands can be distinguished much easier. The bands mark the position of the upward and downward branched of the HCRs. A detailed look at the power spectrum of the transection, indicated as black line perpendicular to the bands in Figure 3.17, reveals that the wavelength of the roll features is approximately 17 pixels in full resolution mode that corresponds to 6.5 km in length. In combination with the boundary layer hight of 1545 m, determined from ERA interim reanalysis data, an aspect ratio of 4.2 is obtained. These findings are in good agreement with the results presented in Weckwerth *et al.* (1997) and Young *et al.* (2002).The structures in the TCWV field along the bands also show significant variation, although no dominating horizontal spacing.

In summary, this study demonstrates the high potential of using high resolution TCWV fields from satellite observations to assess small-scale organized convective features. Although the coverage of observation of TCWV is usually limited in space and time, model

simulation might have relatively coarse resolutions, thus are likely unable to correctly simulate small scale variability of the water vapour field. Many studies have shown, that small scale variability of water vapour field can trigger or enhance convection. The representation of water vapour variability in the models is thus of great importance. The investigation of observations of high resolution TCWV fields can help to improve the understanding of the connection between water vapour and convective initiation.

3.11 Summary and outlook

A universal TCWV retrieval was established that can be adapted for space borne instruments measuring radiances in the $\rho\sigma\tau$-water vapour absorption band. The procedure derives TCWV for cloud-free scenes with an optimal estimation technique and provides uncertainty estimates on a pixel basis. The algorithm was adapted to the MERIS and MODIS channel setup. Comparisons to TCWV data sets from global distributed ground based observations over land reveal a small wet bias for MERIS and a dry bias for MODIS. For MERIS these deviations result probably from errors in the spectral calibration or the optical degradation of the sensor. For MODIS a number of reasons are likely, most presumable uncertainties in the derivation of the absorption. However, due to the fact that the actual reasons still remain unclear, correction coefficients were derived that are applied to the transmittance operator in the forward operator. These coefficients were selected for each absorption channel considering the difference between TCWV from ground based MWR and TCWV from MODIS or MERIS repetitively is minimal. The subsequent validation of the corrected retrieval against independent TCWV data from ground based observations shows high correlations (between 0.88 and 0.99) and low spread (between 0.9 mm and 1.9 mm). A time dependency of the difference between MERIS/MODIS TCWV and ground based observations to location, in particular to latitude as a temporal trend of the bias could be precluded as well.

First evaluation results of the MERIS ocean algorithm were presented. The comparison to space borne MWR and radiosondes reveals a systematic wet bias between 3 mm and 4 mm that is constant with increasing TCWV. In the near future, possible reasons for the differences have to be found and consequent changes have to be applied in the processor. If a sufficient ground truth for ocean surfaces can be found, the calculation and application of absorption correction coefficients is feasible. In addition, the validation of the MODIS retrieval over ocean surfaces has to be performed, that is expected to reveal smaller biases due to the higher information content of the MODIS band setup.

Generally, more data set for validation have to be found (e.g. TCWV from SSM/I), and the existing data set can also be used for the validation above ocean (e.g. coastal GNSS stations).

Additionally, it is planned to adapt the retrieval to OLCI measurements (launched February 16, 2016). The spectrometer has an additional channel at 940 nm reducing the uncertainty of the retrieval especially over the ocean (see Chapter 4). The high

spatial resolution of MERIS and OLCI can support studies of the quantification of small scale variability of TCWV, which is used by models for the parametrisation of cloud development (see Chapter 6).

The Flexible Combined Imager (FCI) on the geostationary MTG will also measure radiance in the $\rho\sigma\tau$-band, that will enable studies of the TCWV field on temporal resolutions up to 2.5 minutes and spatial resolutions up to 1 km. Studies of the diurnal cycle of TCWV will benefit from these MTG TCWV data (see Chapter 5). The data will contribute information of the temporal evolution of TCWV structures in Carbajal Henken *et al.* (2015).

Chapter 4

Quantification of uncertainties of water vapour column retrievals using future instruments

Abstract This study presents a quantification of uncertainties of total column water vapour retrievals based on simulated near-infrared measurements of upcoming instruments. The concepts of three scheduled spectrometers were taken into account: OLCI (Ocean and Land Color Instrument) on Sentinel-3, METimage on an EPS-SG (EUMETSAT Polar System - Second Generation) satellite and FCI (Flexible Combined Imager) on MTG (Meteosat Third Generation). Optimal estimation theory was used to estimate the error of a hypothetical total water vapour column retrieval for 27 different atmospheric cases. The errors range from 100 % in very dry cases to 2 % in humid cases with a very high surface albedo. Generally, the absolute uncertainties increase with higher water vapour column content due to H_2O-saturation and decrease with a brighter surface albedo. Uncertainties increase with higher aerosol optical thickness, apart from very dark cases. Overall, the METimage channel setting enables the most accurate retrievals. The retrieval using the MTG-FCI build-up has the highest uncertainties apart from very bright cases. On the one hand, a retrieval using two absorption channels increases the accuracy, in some cases by one order of magnitude, in comparison to a retrieval using just one absorption channel. On the other hand, a retrieval using three absorption channels has no significant advantage over a two-absorption channel retrieval. Furthermore, the optimal position of the absorption channels was determined using the concept of the 'information content'. For a single channel retrieval, a channel at 900 or 915 nm has the highest mean information content over all cases. The second absorption channel is ideally weakly correlated with the first one, and therefore positioned at 935 nm, in a region with stronger water vapour absorption.

This Chapter is entirely adopted from Diedrich *et al.* (2013).

4.1 Introduction

This work focuses on concepts of retrievals which analyse measured radiation in the near-infrared (NIR) between 800 nm and 1000 nm. As mentioned in Chapter 2 there are several reasons for that, e.g the influence of Rayleigh scattering and scattering on atmospheric particles, and the spectral dependency of the surface reflectance are comparably low. At higher wavelengths, saturation effects are too dominant to retrieve high water vapour columns. At lower wavelengths, the absorption lines are too narrow and the sensitivity of the transmittance with respect to water vapour is too low.

There are already several instruments and retrievals which operationally retrieve water vapour over cloud-free land surfaces in the NIR, for example MERIS on ENVISAT (Lindstrot *et al.* 2012) or MODIS on Aqua and Terra (Diedrich *et al.* 2015). The existing retrievals are various but use a basic principle, the differential absorption technique (Albert *et al.* 2001, 2005, Bartsch *et al.* 1996, Gao *et al.* 1993). The comparison of radiances in a window channel with radiances in an absorption channel provides information about the TCWV.

However, there are a number of error sources for the retrieval of water vapour from NIR-measurements: one part of the uncertainty is due to technical constraints, such as instrumental noise or spectral and absolute calibration of the spectrometers. On top of that, the retrieval is based on various assumptions with respect to, e.g. scattering in the atmosphere or the vertical temperature profile. One goal of this study is the quantification of uncertainties of a hypothetical water vapour retrieval using three future concepts of spectrometers. We selected only concepts of image sensors whose plans include water vapour absorption channels in the NIR. Additionally, we aim to find out how to improve the accuracy of such retrieval by determining the optimal channel setting for the water vapour remote sensing. Although there is no information about the measurement accuracies and the actual retrieval, one can estimate the uncertainties using the optimal estimation theory and the concept of information content.

4.2 Instruments

OLCI

The *Ocean and Land Color Instrument* (OLCI) is planned to be the sequel of MERIS. It will be installed on the Sentinel-3 orbiter, which is part of the GMES (Global Monitoring for Environment and Security) program. It is scheduled to be launched in 2016 with a lifetime of approximately more than 12 years (fuel for five more years is going to be available). To provide a better temporal resolution, it is planned to operate two identical platforms which orbit the Earth on sun-synchronous tracks at about 815 km height with a delay of 180 degrees. OLCI will be comprised of five identical cameras in a fan shape alignment (role model: MERIS). It will measure the radiation reflected from the Earth in the visible and near-infrared spectrum. The spatial resolution of the spectrometer will

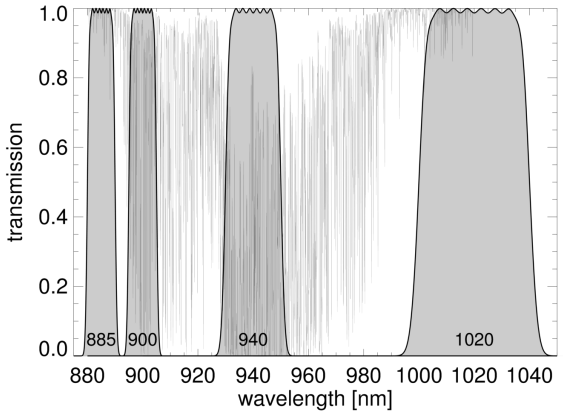

FIGURE 4.1: OLCI channel constellation in the NIR (normalized response functions) and total transmittance of the atmosphere in ρστ-band.

be 300 m (full resolution), which can be downscaled to reduced resolution (1200 m), and will be able to sample a line of 1300 km (field of view: 68.5°) at once. The observation geometry will be tilted by 12 degrees to reduce sun glint effects. With a two-satellite composition, global coverage will be achieved within 4 days. Every 27 days, a cycle will be repeated. OLCI will be upgraded in comparison to MERIS from 15 to 21 spectral channels in the wavelength range of 0.4 to 1.02 μm [1]. The planned channels in the near-infrared, relevant for water vapour retrievals, are shown in Figure 4.1.

METimage

METimage will be a multi-spectral radiometer, mounted on the second generation of EUMETSAT Polar SYSTEM (EPS-SG) satellites. This framework consists of 3 polar orbiting MetOp satellites and its prime objective is to provide continuous, long-term data sets of meteorological quantities. Metop-A was launched in 2006, Metop-B in 2012 and Metop-C will follow in 2016. The center of the METimage concept is a rotating telescope developed by *Jena-Optik*. The Visual/Infrared Imager (VII) will detect sunlight, reflected by the Earth, in the VIS and NIR spectrum from 0.4 to 14 μm. A spatial resolution of maximum 250 m and a field of view of 110° (swath approximately 2800 km) is expected. The radiometer scans 20 pixel simultaneously with a field of view of 1° $(20\,\text{km})^2$. The channel constellation and the number of channels has not yet been finally decided between a 20-channel or a 30-channel concept. The Institute for Space Science at the Free University Berlin was asked to ascertain the best channel position and combination for the water vapour remote sensing. The planned channels in the NIR, relevant for water vapour retrievals, are shown in Figure 4.2.

[1] `http://www.ioccg.org/sensors/olci.html`.
[2] `http://www.eumetsat.int`.

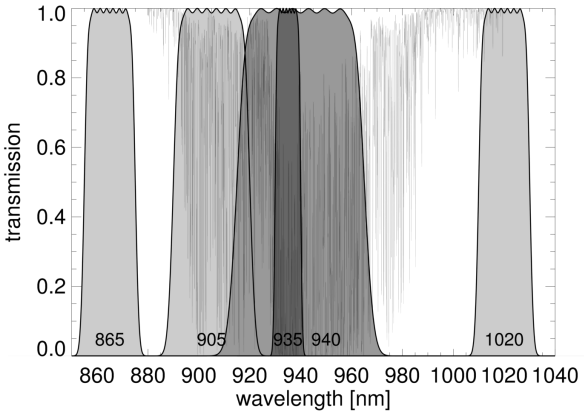

FIGURE 4.2: METimage original channel constellation in the NIR (normalized response functions) and total transmittance of the atmosphere in $\rho\sigma\tau$-band.

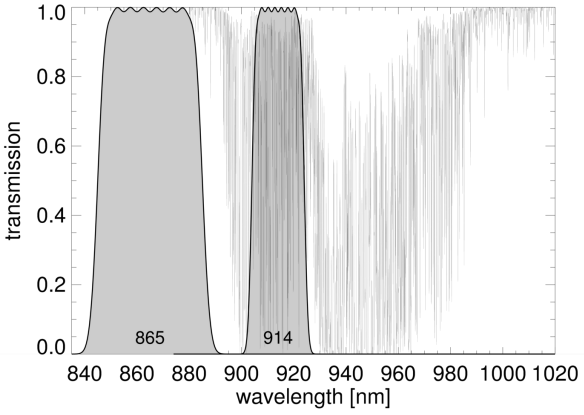

FIGURE 4.3: MTG-FCI original channel constellation in the NIR (normalized response functions) and total transmittance of the atmosphere in $\rho\sigma\tau$-band.

MTG-FCI

The *Meteosat Third Generation* (MTG) system is going to replace the *Meteosat Second Generation* (MSG). The concept of geostationary satellites is based on two three-axis-stabilized platforms, the MTG-I (imager) and the MTG-S (sounder). The scheduled launch will be in 2018. A spectrometer will be installed on MTG-I, the *Flexible Combined Imager* (FCI). It can detect the electromagnetic radiation in 16 channels rather than 12 on MSG between 0.4 and 13.3 μm with an expected spatial resolution of maximal 1 km between 0.4 and 2.1 μm and a spatial resolution of 2 km between 3.8 and 13.3 μm [3]. The planned channels in NIR, relevant for water vapour retrievals, are shown in Figure 4.3.

[3] `http://www.eumetsat.int`.

4.3 Quantification of uncertainties

Best estimate error

Any measurement (y) has an associated uncertainty (σ_y). In case of remote sensing, measurements are generally TOA radiances. The determination of the measurement error of the instrument is realizable by calibration and comparison measurements. Most techniques retrieve physical properties from radiance measurements through the use of sophisticated inversions. This means that the retrieved quantities (combined in the state vector $\vec{x}$) will also be uncertain (σ_x is the error of the retrieved quantity). These inversions commonly iteratively optimize the result of a forward model F, which uses considerable additional (prior-)information (model parameters p) that are also contaminated with errors σ_p:

$$\mathbf{y} \pm \sigma_{\mathbf{y}} = \mathbf{F}(\mathbf{x} \pm \sigma_{\mathbf{x}},\ \mathbf{p} \pm \sigma_{\mathbf{p}}) \ . \tag{4.1}$$

As an example, the TOA radiance reflected from the Earth depends on parameters such as the surface albedo, the aerosol load, the water vapour content, and clouds, the temperature of each which can be measured only to a certain accuracy. The question is, how can we determine the uncertainty of the retrieved atmospheric property σ_x without knowledge of the exact retrieval technique? One method was introduced by Rodgers (2000), and uses the Bayes' with an assumption of normally distributed errors. An overview of the method is presented here; for detailed derivation we refer to the book by Rodgers (2000).

The influence of an individual parameter on the retrieved state can be calculated, assuming that the sensitivity of the measurement to the parameter is known. For example, in cases where the uncertainty of a model parameter is large but the sensitivity of the measurement to the parameter is negligible, there is no significant increase in the uncertainty of the retrieved state. The influence of individual parameters on the measurement can be simulated with a radiative transfer model (e.g. MOMO). The Jacobian of the radiance according to a certain parameter can be approximated by the change in radiance in response to a small change in the parameter, while keeping all other parameters constant.

A matrix $\mathbf{K}^p$ is constructed, which contains information about the sensitivity of the parameters to the measurement and whose size depends on the number of channels and parameters. The entries in the matrix are effectively the derivatives of the radiance in a channel i to the variation of the j model parameter:

$$\mathbf{K}^p_{i,j} = \left\{ \frac{\delta y_i}{\delta p_j} \right\} \ . \tag{4.2}$$

In this case, local linearity must be assumed. The uncertainty of the prior knowledge of each model parameter is stored in a covariance matrix $\mathbf{S}^p$:

$$\mathbf{S}^p_{i,j} = \{ c_{i,j} \sigma_{p,i} \sigma_{p,j} \} \, , \tag{4.3}$$

where $\sigma_{p,i}$ is the uncertainty in units of standard deviation of the i model parameter and $c_{i,j}$ is the linear correlation coefficient between the i and j parameter. For many applications this correlation is zero, resulting in a diagonal matrix $\mathbf{S}^p$. The measurement error covariance matrix $\mathbf{S}^y$ is defined as

$$\mathbf{S}^y_{i,j} = \{c_{i,j}\sigma_{y,i}\sigma_{y,j}\}\,, \tag{4.4}$$

where $\sigma_{y,i}$ is the measurement error in units of standard deviation for the i channel of the spectrometer and $c_{i,j}$ is the correlation between the error in the i and j channel, which is zero for standard spectrometer. So $\mathbf{S}^y$ has the diagonal elements: where L_i is the radiance measured in channel i, SNR_i the signal to noise ratio ($\mathrm{SNR} = y/\sigma_y$) and Δ_i the uncertainty of the absolute calibration of channel i. The matrix $\mathbf{K}$ carries information about the sensitivity of the measurement in the i channel to the j element of the state vector $\vec{x}$, so the derivatives of radiance to the retrieval quantity are

$$\mathbf{K}_{i,j} = \left\{\frac{\delta y_i}{\delta x_j}\right\}\,. \tag{4.5}$$

Finally, the error covariance matrix of the state vector is defined by

$$\mathbf{S}^x = \{c_{i,j}\sigma_{x,i}\sigma_{x,j}\}\,. \tag{4.6}$$

This matrix describes the uncertainties of the retrieved quantity. The square route of the diagonal elements of $\mathbf{S}^x$ specifies the error in the unit of the retrieved value, and is thus the sought after quantity

According to Rodgers (2000), the approach to calculate $\mathbf{S}^x$ is as follows. First, the model uncertainty $\mathbf{S}^e$ is derived by propagating the model parameter uncertainty $\mathbf{S}^p$ into the measurement space, and adding the measurement uncertainty $\mathbf{S}^y$:

$$\mathbf{S}^e = \mathbf{S}^y + \mathbf{K}^p\mathbf{S}^p{\mathbf{K}^p}^T\,. \tag{4.7}$$

The second step is the propagation of $\mathbf{S}^e$ into the state vector space, which is different from standard error propagation. The inverse model uncertainty is combined with the Jacobian of the forward operator ($\mathbf{K}$):

$$\mathbf{S}^x = (\mathbf{K}^T{\mathbf{S}^e}^{-1}\mathbf{K})^{-1}\,. \tag{4.8}$$

Prior or background knowledge of the retrieval quantity is not included in this approach.

Information content

Another way of evaluating the retrieval error is the information content (Shannon 1948), which is analogous to the concept of entropy in thermodynamics. The information content H provides the "value" of a measurement. It is the reduction in entropy S:

$$H = S(P_1) - S(P_2), \tag{4.9}$$

TABLE 4.1: Sensitivity simulations input parameter cases.

Property	low	medium	high
Water vapour column	1 mm	30 mm	70 mm
Aerosol optical thickness	0.1	0.4	1.0
Surface albedo	0.05	0.2	0.8

where P_1 is the uncertainty before and P_2 after the measurement. For a Gaussian distribution, the information content is calculated by Eq. (4.10):

$$H = 0.5 \log_2(\sigma_a^2) - 0.5 \log_2(\sigma_x^2), \tag{4.10}$$

where σ_a is the standard deviation due to the natural variability of the parameter and σ_x is the uncertainty of the retrieved parameter. H determines the number of possible states of the measurement in binary bits. For example, the water vapour column content normally varies between 1 and 70 mm. If the retrieval can only derive the water vapour content with an accuracy of 10 mm, H is very low because the uncertainty is in the range of the natural variation. According to simple logarithm laws, Eq. (4.10) implies the quotient of the variances of the retrieval value and its uncertainty, which is similar to the concept of the signal-to-noise ratio. Thus, the higher the uncertainty of the retrieval, the lower the information content and the smaller the number of possible states that can be resolved based on the measurements.

4.4 Atmospheric cases and assumptions

In this work, the quantification of uncertainties was performed for a number of different cases. As already mentioned, the ratio of TOA radiances from an absorption and a window channel (L_{abs}, L_{win}) provides information about the TCWV and is hereafter referred to as the apparent transmittance R:

$$R = L_{\text{abs}}/L_{\text{win}}. \tag{4.11}$$

In the NIR spectrum, the apparent transmittance is most sensitive to the water vapour column content and is influenced mainly by the surface albedo and the aerosol optical thickness. Consequently, three cases were considered for each parameter (low, medium and high values) (see Table 4.1). This results in a total number of 27 atmospheric cases.

Additionally, three other model parameter sensitivities were determined: the influence of a cirrus cloud (varying the cirrus optical depth between 0.1 and 1.6), the change of the temperature profile (shifting the temperature profile by a constant offset of ±10 K), and the scale height of an aerosol layer (varying the scale height between 1000 m and 4000 m, homogeneous aerosol layer with 500 m thickness).

TABLE 4.2: Sensitivity simulations input parameter uncertainties in unit of standard deviation for each case (see Table 4.1).

Property	low	medium	high
Aerosol optical thickness	0.05	0.05	0.05
Surface Albedo	0.02	0.03	0.05
Cirrus optical depth	0.1	0.1	0.1
Aerosol scale height	3000 m	3000 m	3000 m
Temperature profile	20 K	20 K	20 K

The theory of optimal estimation requires the knowledge of the uncertainties of the model parameters. The assumed accuracies are given in Table 4.2 as standard deviations. These parameters were considered to account for the error influences on the TCWV. The sensitivity to cirrus clouds was considered to include the influence of sub-pixel cloud contamination. Also, present cloud detection algorithms are not accurate enough to detect thin clouds. The height of the aerosol layer (see below) and the natural change in the temperature profile are significant error influences. The uncertainties of the parameters were assumed. For the aerosol optical thickness, cirrus optical depth, aerosol scale height, and temperature profile, the accuracies were kept constant for each of the 27 cases. For the surface albedo, Carrer *et al.* (2010) was taken into account. This validation report is very comprehensive and includes a large number of results for the uncertainties of the albedo. The inter-comparisons between different procedures show a spread between 0.02 and 0.05. On the one hand, the uncertainties were determined as constant with higher albedo, but on the other hand, constant in percentage, depending on the assumption regarding the bidirectional reflectance distribution function. In this study, an increasing error with larger surface albedo was assumed (see Table 4.2). However, the exact values do not influence the general outcome of this study.

Furthermore, the influences of the profile shape of water vapour, aerosol or temperature were not considered in the determination of the uncertainties. Again, only the temperature profile was altered equally in every layer. The US Standard atmosphere profile was used. The calculated uncertainties refer only to the whole vertical column of the atmosphere. Nevertheless, the profile shape plays an important role when interpreting the influences of the albedo and aerosol optical thickness. The peak altitude of the sensitivity for the water vapour column at the TOA can be understood from Figure 4.4. Here, the sensitivities of the apparent transmittance R (window channel at 885 nm, absorption channel at 900 nm) is shown as a function of height for five different surface reflectances. The sensitivities for each layer were derived from the difference between the reference ratio and the ratio simulated with an increased water vapour content (+0.1 mm) in that layer divided by the change in water vapour. For reference, the US standard water vapour profile was chosen and a homogeneous continental aerosol layer at 700 hPa (3000 ± 250 m) with an optical thickness at 900 nm of 0.1. As the figure clearly shows, the peak altitude of the sensitivity is governed by the surface reflectance and the aerosol layer height. The lower the surface reflectance, the more information originates from the layer above the aerosol layer. The influence of the aerosol layer increases with

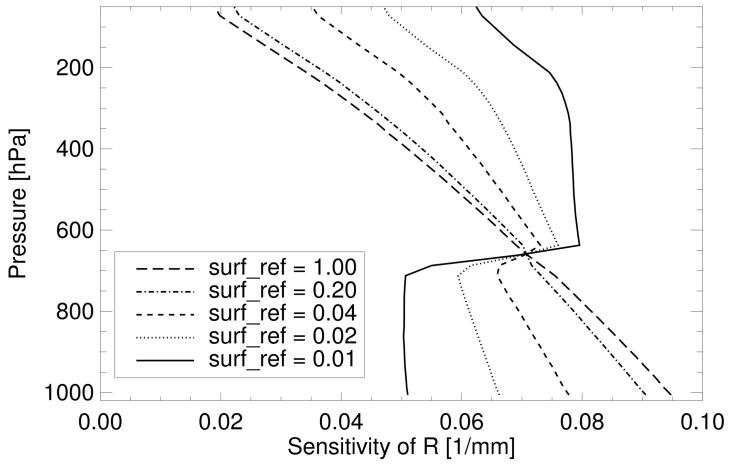

FIGURE 4.4: Sensitivity in 1 mm of the apparent transmittance R to the water vapour column content as a function of pressure (height levels) for five different surface reflectances (surf_ref). A constant aerosol layer at 700 hPa is present.

higher optical thickness (not shown here). This is a significant error influence for surface reflectances below 0.2. Nevertheless, we only accounted for that in the parameter uncertainties (see Table 4.2).

The influence of other atmospheric properties, such as the Rayleigh optical thickness, carbon dioxide and amounts of other greenhouse gases, etc., was assumed to be very low in the wavelength range of interest. Consequently, these parameters were not regarded in this study and kept constant in the simulations. The aerosol optical thickness is highly dependent on the considered wavelength. In this work, the specified aerosol optical thicknesses are always defined at 900 nm. In every case a continental aerosol was predefined. The size properties and refractive indices of the aerosol were taken from Hess *et al.* (1998).

The albedo of natural surfaces is a function of wavelength. In cases of real measurements, a common approach to account for this effect is to linearly extrapolate the surface reflectance in the window channels to estimate the surface reflectance in any spectrally close absorption channel. Within the framework of this study, the so-called albedo slope was not considered in the simulations, meaning that for a fixed case the same albedo was used for all simulated channels. However, when calculating the uncertainties, this phenomenon was included with the help of the following. The surface reflectance uncertainty affects the retrieval in two ways, the uncertainty of the absolute albedo and its spectral slope:

1. The uncertainty of the assumed surface reflectance in the window channels, resulting from uncertainties in the atmospheric correction, directly propagates to the uncertainty of the surface reflectance in the absorption channel. However, this error has the same sign in all channels, since the scattering properties hardly vary

within the considered spectral ranges. Since the information used for the water vapour retrieval is provided by the ratio of absorption and window radiances, there is hardly any additional error contribution by the uncertain surface reflectance in the absorption channel. This is reflected by a high correlation of the uncertainties of both reflectance values in the error covariance matrix $\mathbf{S}_e$.

2. The correlation of the surface reflectance uncertainties is reduced in cases of a strongly varying albedo slope, resulting in a higher error contribution by the absorption channel. A spectral surface albedo database was analysed with respect to the correlation of the surface reflectance values for different surface types and channel positions. Not surprisingly, the correlation is lower for spectrally distant channels, resulting in errors that are less correlated and higher retrieval uncertainties. The error covariance matrix $\mathbf{S}_e$ of the model parameters (Eq. 4.11) was adapted accordingly.

Since the instruments are not built yet and calibration errors or signal-to-noise ratios (SNR) are not determined, the measurement errors can only be assumed (guided by the specifications of the concepts). For this reason, a standard SNR of 400 was preconditioned for each channel, which is in the approximate range of a NIR radiance measurement. The SNR is dependent on the channel width because more energy is coming in with a broader spectral range. However, this quantity turned out to have a non-significant influence and was kept constant. No absolute calibration uncertainties or systematic measurement errors were assumed.

Additionally, the instrument-specific response functions are not available yet. Nevertheless, the shape of response functions has a very low impact on the measured radiance. For convenience, the response function of the MERIS channel 15 was used. It was adapted to the different scheduled positions and widths (see Figures 4.1, 4.2, 4.3). In the investigation of the optimal channel distribution, this response function was also used.

4.5 Results

Uncertainties

Uncertainties in mm of possible water vapour retrievals using the channel distributions of the original concepts of the three planned instruments are shown in Figure 4.5. For OLCI and METimage, two window channels close to the $\rho\sigma\tau$-band were chosen. For MTG only one window and one absorption channel were considered. For the OLCI retrieval, two absorption channels, and for the METimage retrieval, three absorption channels, will be provided. The uncertainties of the 27 cases of a combination of three atmospheric properties are plotted. The legend for these cases is displayed below the plot as coloured bars of total water vapour column (TCWV) in blue, surface albedo (ALB) in yellow and aerosol optical thickness (AOT) in black. Although the uncertainties are

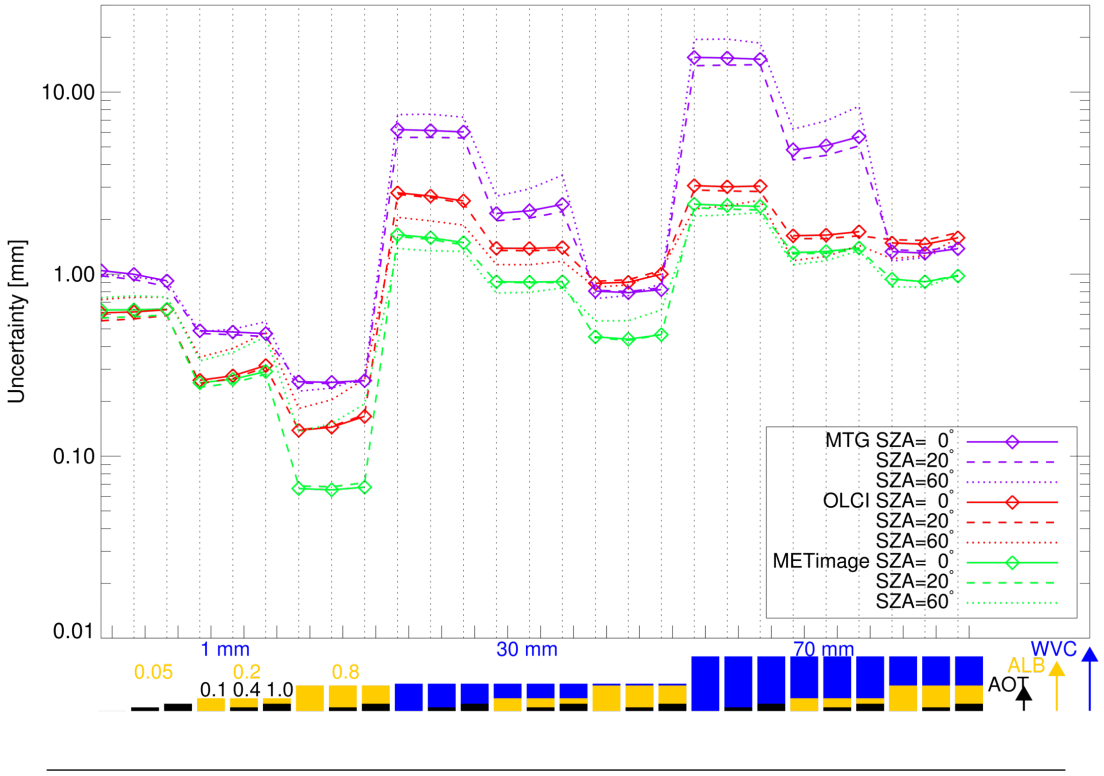

FIGURE 4.5: Uncertainties of water vapour retrievals in mm of three channel combinations of future instruments (OLCI, METimage, MTG) for 27 different cases of a combination of three atmospheric properties: total column water vapour (TCWV), albedo (ALB), and aerosol optical thickness (AOT) – for three different sun zenith angles (SZA).

discrete points, for better clarity a line was drawn between the points of each albedo class for sun zenith angle (SZA) of 0 degrees. Additionally, uncertainties for SZA of 20 and 60 degrees were calculated and plotted in dashed lines for each instrument.

The most striking feature is that the original METimage channel combination (in green) is more certain in almost every case (apart from dark surfaces with low water vapour content) than the others. The four-channel retrieval of OLCI in red has slightly larger uncertainties than METimage but less than the two-channel retrieval of MTG in purple (apart from cases with a bright surface and medium and high water vapour values). Generally, the uncertainties increase with higher water vapour content. This is due to the fact that absorption lines eventually reach saturation. In other words, the change of the transmittance in a water vapour absorption band approaches zero for higher values. Thus, sensitivity of the measurements to TCWV decreases with increasing humidity.

Another finding is the reduction of uncertainties with brighter surfaces, in some cases with one order of magnitude. Brighter surfaces reflect more radiation. Thus, the measurement is dominated by photons that have not been scattered at atmospheric particles. Above dark surfaces, a large number relative to the total amount of photons gets scattered back in the atmosphere and consequently does not travel through the whole

vertical column of water vapour (Lindstrot *et al.* 2012) (see also Figure 4.4). Hence, the uncertainty is higher for dark than for bright surfaces.

The dependency of the accuracy of the retrievals to the aerosol load is more dissimilar. In cases of a bright surface, the uncertainty slightly *increases* with a larger optical thickness of the aerosol layer. In contrast, in cases of a dark surface, the uncertainty slightly *decreases* with higher aerosol load. This is due to the fact that the aerosol layer, located in the lower troposphere, reflects a part of the radiation. Although this radiation does not reach the surface, the presence of the aerosol layer increases the fraction of measured photons that originate from the lower troposphere and thus decreases the error in the water vapour path (see Sect. 4.4 and Figure 4.4).

To interpret the influence of the errors on the measurement, it is more enlightening to examine the uncertainties relative to the simulated amount of TCWV (not shown here). Generally, the relative uncertainties decrease with higher water vapour value. This is consistent because the sensors have limited measurement sensitivities. A very small change in transmittance due to a small TCWV amount can only be determined with low accuracy. In cases of MTG, the relative uncertainty exceeds 100 %; and in cases of METimage and OLCI, it is around 70 % over dark surfaces. The lowest values can be examined over bright surfaces. Again, higher intensities provide more information for the sensor and therefore the uncertainties are smaller. For medium water vapour amounts around 30 mm, one has to expect a relative error of around 1 to 10 %, depending on the surface and atmospheric circumstances.

To determine the influence of the different viewing geometries, uncertainties for two exemplary sun zenith angles were calculated and plotted. The impact of a SZA of 20 degrees on the accuracy is negligible. For dry cases, the uncertainties of all retrievals is higher at a SZA of 60 degrees than for a SZA of zero degrees. This applies also for MTG in the humid cases but not for OLCI and METimage.

Retrievals with one and two absorption channels

In the previous paragraph the behaviour of the scheduled channels was illustrated. The question arises as to whether this is the optimal distribution and combination of channels. As seen in Figure 4.5, it seems that not only the location but also the number of absorption channels have an impact on the accuracy of the retrievals. MTG with only one absorption channel has larger uncertainties than the OLCI and METimage with two and three absorption channels.

In the following, the exemplary METimage channel locations were used in order to assume the optimal absorption channel. Figure 4.6 has the same format as Figure 4.5. The original METimage retrieval is plotted in green again. The other colors account for one-absorption-channel retrievals with two window channels at 865 and 1020 nm and one of the three absorption channels, respectively (905 nm in red, 935 nm in purple, 940 nm in dark grey). Obviously, the retrievals using only one absorption channel have

larger uncertainties than the original METimage setup, in some (dark surface) cases even one order of magnitude. For cases with medium- and high water vapour, the lowest uncertainties were found for the retrieval using the absorption channel at 905 nm. The other two have a very low accuracy, especially in the humid cases. This is due to the fact that they reach saturation more easily because they are located in a strong absorbing wavelength range. However, this behaviour benefits their accuracy in the dry cases. For low water vapour contents, the uncertainties are quite similar. Here, the retrievals with the absorption channels 935 and 940 have lower uncertainties.

Figure 4.7 shows the results of the uncertainty calculation of retrievals with two window channels and a combination of two absorption channels (see the legend on the right bottom of the plot). Again, the original METimage retrieval is plotted in green. The most evident feature in comparison to Figure 4.6 is that the uncertainties are lower (see the scale) in nearly all cases and close to the retrievals using all scheduled channels. The one with the best accuracy is the combination of absorption channel at 905 nm and 935 nm because the difference to the original retrieval is very low in every case. However, the combination of absorption channel at 905 and 940 nm is best in cases of bright surfaces. In dry cases, the different combinations only differ minimally. In medium and humid cases, the combination of 935 nm and 940 nm (the strong absorbing channels) is the poorest. These latter medium and humid cases also seem to have the strongest sensitivity to the aerosol load.

In summary, retrievals with two absorption channels are more accurate than with only one. The best combination seems to be 905 nm and 935 nm; it is nearly as certain as the original combination of all three absorption channels. The combination of a channel close to the first window channel and one in the strong absorbing range appears to be a good choice.

Optimal channel setting

In the following, our aim is to ascertain whether the channel positions, widths, and their combinations can be improved in order to decrease the uncertainties of a potential TCWV retrieval. For this purpose it is more convenient to examine the information content because it is similar to the relative error and indicates the quality of a measurement on a linear scale. The example shown is for the METimage build-up.

One absorption channel retrieval

First, the optimal location for a one absorption channel retrieval was sought. To this end, the information content for a retrieval with two window channels (865 and 1020 nm) and one variable absorption channel with a width of 10 nm was calculated. Figure 4.8 shows the information content as a function of the wavelength (ordinate) and the cases of the atmospheric state, which are equivalent to the ones in the last paragraph (abscissa). Each pixel represents the information content of a certain case and a certain center

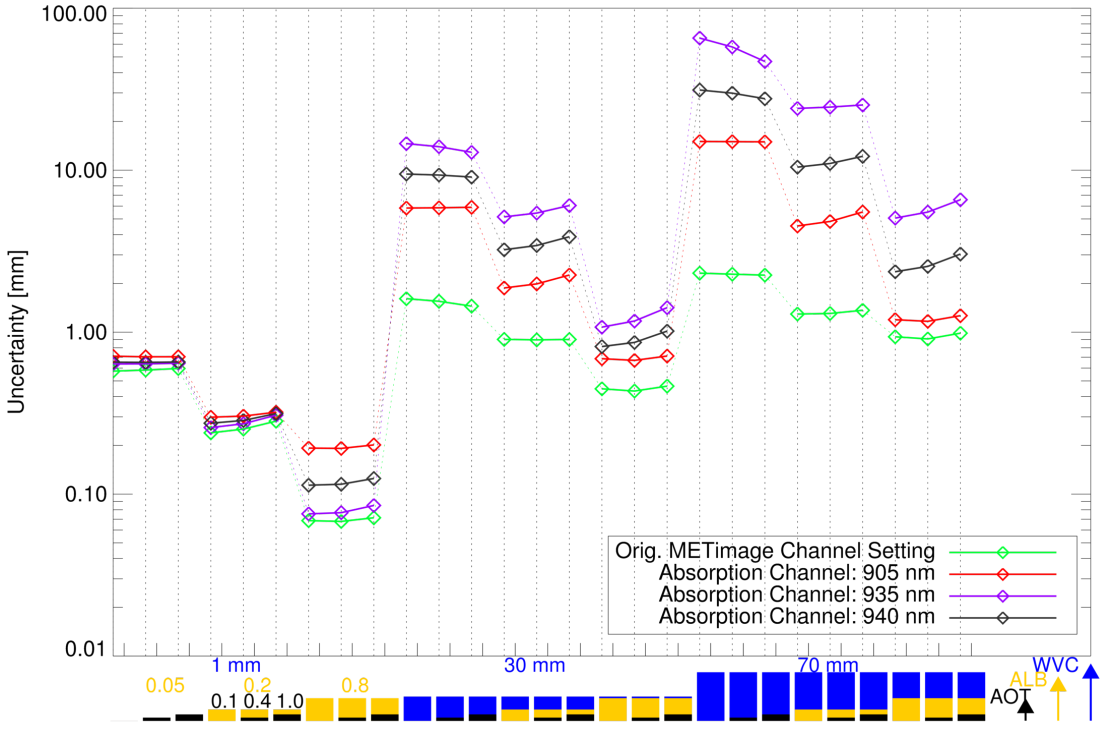

FIGURE 4.6: Uncertainties in mm of water vapour retrievals using one absorption channel and two window channels (METimage concept) for 27 different cases of a combination of three atmospheric properties: total column water vapour (TCWV), albedo (ALB), and aerosol optical thickness (AOT).

wavelength. Dark blue pixels account for low and red for high information content. Again, in short, the higher the information content, the higher the number of possible states that can be resolved and the lower the uncertainty of the model.

The most noticeable feature is again the decrement of information content with higher water vapour values. The strong connection between information content and surface albedo is also clear and is represented by the vertical bars of similar color. The highest information content (around 11 bits) was calculated in the dry cases at the strong absorbing channels represented by the deep red pixels. Reasons for that were mentioned in the last chapter. The lowest information content (represented by dark blue pixels) was determined for cases with a high water vapour content and in the strong absorbing wavelength range higher than 925 nm. In changing atmospheric cases, the information content behaves as described before (apart from 880 nm and 885 nm); only the magnitudes differ between the channels. If based exclusively on the findings from Figure 4.8, it is difficult to decide which channel is the best for a water vapour retrieval. On the one hand, the maximum information content can be seen at 935 nm and 950 nm, but only for dry cases. On the other hand, these give only a small amount information for humid cases. Hence, it is more convenient to analyse the information content averaged over all cases.

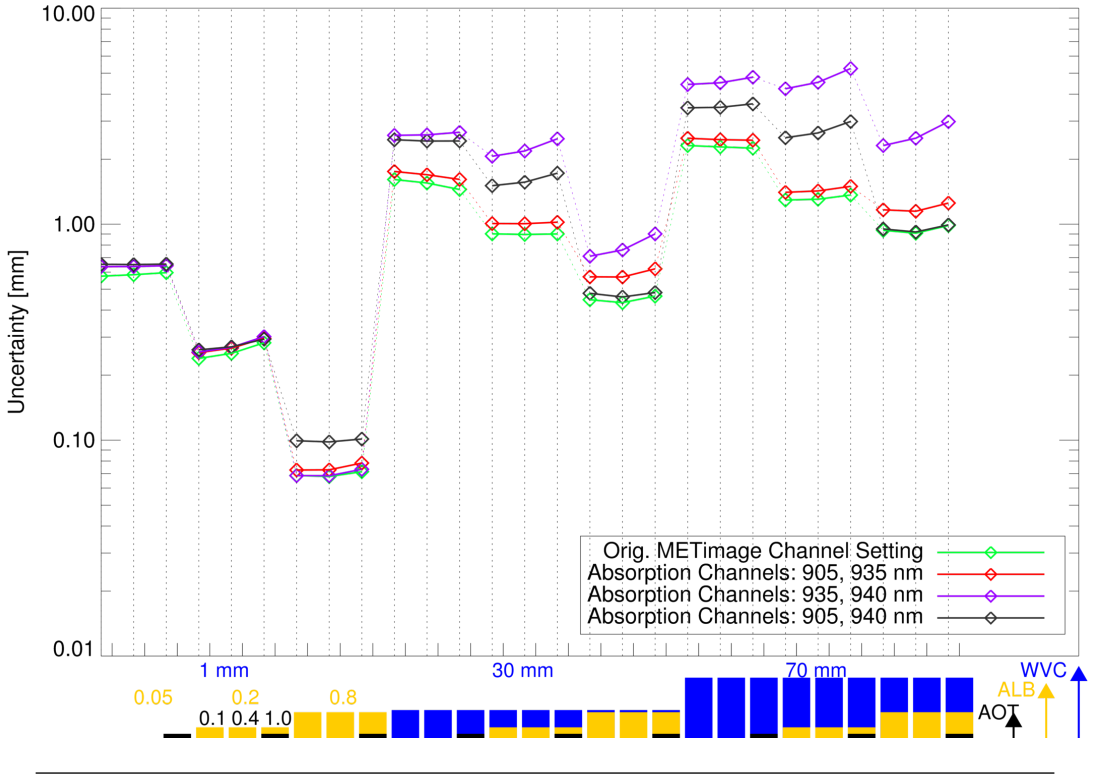

FIGURE 4.7: Uncertainties in mm of water vapour retrievals using two absorption channels and two window channels (METimage concept) for 27 different cases of a combination of three atmospheric properties: total column water vapour (TCWV), albedo (ALB), and aerosol optical thickness (AOT).

The mean, minimum and maximum information content of all cases as well as the standard deviation is displayed in Figure 4.9 as a function of the simulated channels. As before, the strongly absorbing channels show the highest information content but at the same time provide almost no information for humid cases, which is contrary to the desired behaviour of a TCWV retrieval. The goal is to use an absorption channel which is least dependent on the atmospheric case. Looking at the mean, which is represented by the dashed line, two maxima appear at 900 nm and 915 nm, both indicating a relatively high information content over all cases. The information content in these channels have a much smaller standard deviation than the other relative maximum at 950 nm. This leads to the conclusion that for a one absorption channel retrieval, either 900 or 915 can serve as the best choice and the MTG-FCI channel selection is optimal.

Two absorption channel retrieval

The information content of a two absorption channel retrieval is displayed in Figure 4.10 with similar logic as in Figure 4.9. One absorption channel is at 900 nm (width 10 nm) and the other is at the location indicated at the ordinate (width again 10 nm). Overall, the information content is increased in comparison to Figure 4.9. The highest mean,

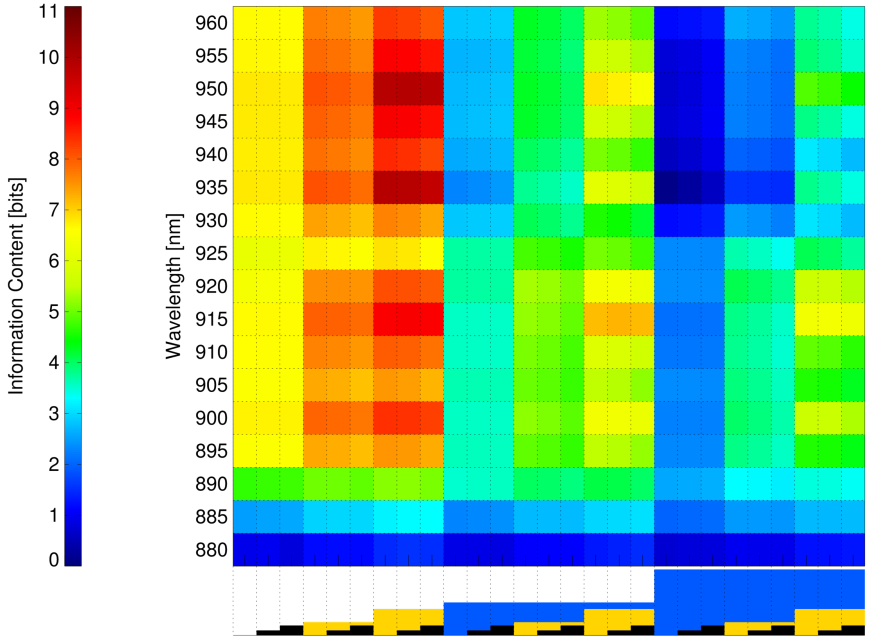

FIGURE 4.8: Information content concerning water vapour of a retrieval using two window channels (METimage: 865, 1020 nm) and one absorption channel (width 10 nm, nadir view) for 27 cases of different atmospheric circumstances (abscissa with legend equivalent to Figure 4.5).

maximum and minimum information contents were determined for wavelengths above 925 nm. The maxima at 935 and 950 nm are outstanding (with a mean of 6.5 respectively 6 bits over all cases). At these wavelengths, the minimum and maximum information content is maximal as well. Thus, the optimal second absorption channel for this case is at 935 nm.

The information content for a two absorption channel retrieval with a fixed first absorption channel at 915 nm is plotted in Figure 4.11. Generally, the information contents are in the same range as in Figure 4.10. Here, only one maximum in the mean information content at 950 nm is evident and is in the same range as the combination 900 and 935 nm. Consequently, the combination of 915 nm and 950 nm is a good choice for a two absorption channel retrieval as well. Comparing Figures 4.10 and 4.11 reveals that the combination of 900 nm and 935 nm gives slightly higher information contents than 915 nm and 950 nm. The water vapour channels of METimage are therefore well designed. The 940 nm channel does not improve the retrieval uncertainties significantly (see Figure 4.7). This is probably due to the fact that it is planned to have a width of 50 nm and therefore overlap with the 935 nm and 905 nm (see Figure 4.2). Generally, a two absorption channel retrieval is more reliable if the absorption channels are least correlated. This was confirmed by cross-correlating all simulated radiances in the different channels (not shown). The lowest correlation coefficient was calculated for the combination of 900 and 935 nm.

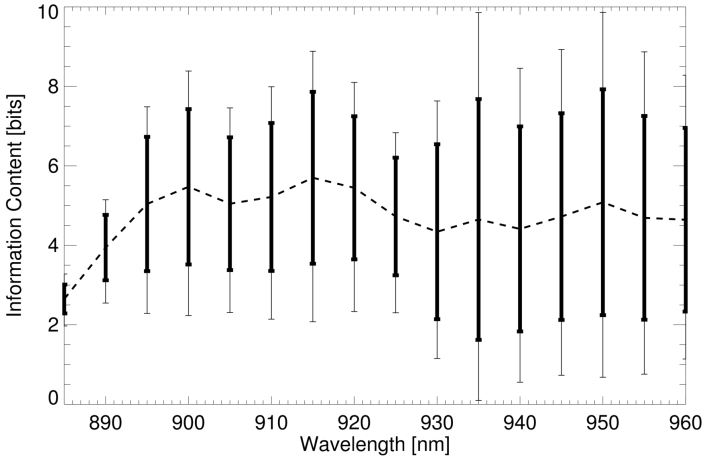

FIGURE 4.9: Mean information content in 27 cases of different atmospheric circumstances concerning water vapour of a retrieval using two window channels (METimage: 865, 1020 nm) and an absorption channel (width 10 nm) (broad bars account for the standard deviation of the cases).

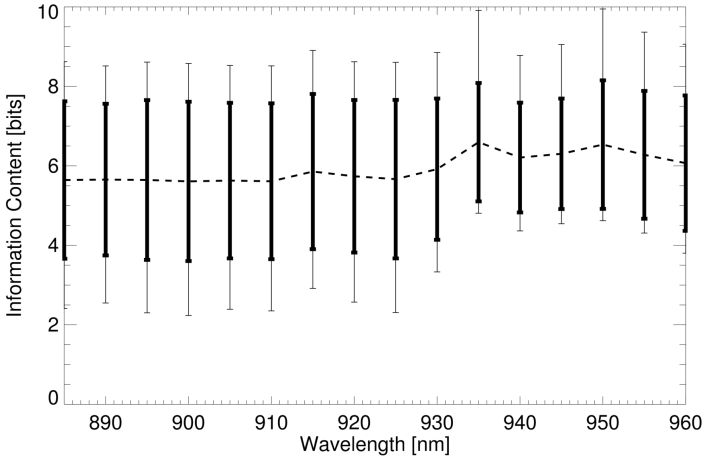

FIGURE 4.10: Mean information content in 27 cases of different atmospheric circumstances concerning water vapour of a retrieval using two window channels (865, 1020 nm), a fixed first absorption channel at 900 nm and a second absorption channel (width 10 nm) (broad bars account for the standard deviation of the cases).

4.6 Discussion

This study analyses the behaviour and the quantities of the uncertainties of possible TCWV retrievals using TOA radiance measurements from future instruments. Depending on the atmospheric state, relative errors of up to 10 % for medium water vapour values and up to 100 % for very dry cases can be expected. The absolute uncertainties

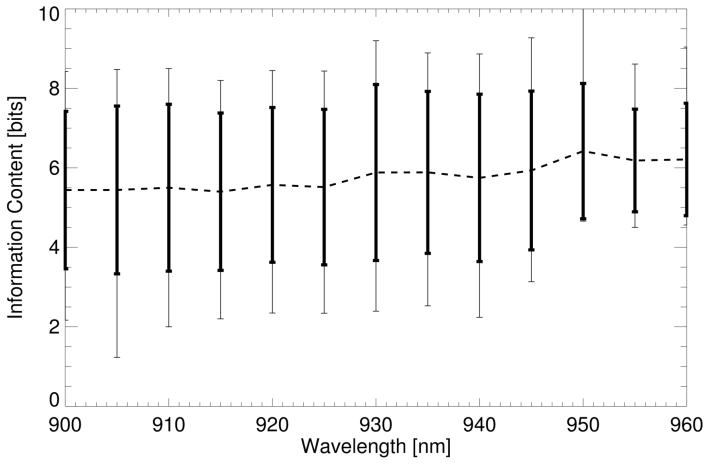

FIGURE 4.11: Mean information content in 27 cases of different atmospheric circumstances concerning water vapour of a retrieval using two window channels (865, 1020 nm), a fixed first absorption channel at 915 nm and a second absorption channel (width 10 nm) (broad bars account for the standard deviation of the cases).

increase with higher water vapour content because of H_2O saturation. Brighter surfaces reflect more radiation and thus the uncertainty decreases with higher surface albedo. The accuracy decreases slightly with higher optical thickness over medium and bright surfaces. In cases of a very dark surface, a thick aerosol layer can increase the accuracy slightly because of the increased amount of radiation that has been reflected in the lower troposphere. The overall uncertainty over all cases turns out to be a function of the number of considered absorption channels. The METimage channel setting with three absorption channels was more accurate than the OLCI setting with two absorption channels and the MTG-FCI with one absorption channel for most cases.

The determination of the optimal position of the absorption channels was done in two steps. First, a retrieval using one absorption channel and the instrument-specific window channels were used to calculate the information content for each atmospheric case. The case-dependent behaviour of the information content is similar to the characteristics of the uncertainties: the information content decreases with higher water vapour values (due to H_2O-saturation), increases with higher surface albedo, and decreases slightly with a higher aerosol load. However, there are differences in magnitude between the used absorption channels. The optimal position for the "first" absorption channel was determined to be at 900 or 915 nm. The second step was to calculate the accuracy of a retrieval using the window channels, one fixed absorption channel and a second absorption channel with varying position. It turned out that the second absorption channel is optimally placed in the strong absorbing range above 930 nm. The highest information contents were determined for the combination of 900 nm and 935 nm. This was explained by the low correlation between theses wavelengths. The channel width, which had been varied between 10 and 20 nm, did not seem to have a strong influence on the information content. A second absorption channel of 20 nm width slightly improved the accuracy

of the retrievals (not shown). Consequences for the schedules of the instruments are comparably minor. For the METimage concept, the broad 940 nm absorption channel should not be considered. In the OLCI schedule, the location of the second absorption channel should be changed to 935 nm. The 914 nm channel of the MTG-FCI concept seems to be a good choice. In general, though, many retrievals and applications already use the 900 nm to determine TCWV. To continue the time series of, e.g. MERIS on ENVISAT, with the same retrievals, the 900 nm channel is the recommended choice.

Chapter 5

Representativeness of total column water vapour retrievals from instruments on polar orbiting satellites

5.1 Introduction

Water vapour plays a key role in the hydrological cycle of the Earth's atmosphere. The Total Column Water Vapour (TCWV) is a good indicator/tracer of atmospheric transport of water vapour. The diurnal cycle of TCWV over land is influenced by evapotranspiration as a source, condensation and precipitation as sinks, and additionally by atmospheric advection (Trenberth 1999). Over the years, multiple techniques have been established to determine the TCWV from ground and from space. TCWV from measurements of radiosondes, microwave radiometers and GNSS receivers are examples for sophisticated ground based sources of TCWV values on a high temporal resolution that are hardly affected by clouds (e.g. Radiosonde: Seidel *et al.* (2009), microwave radiometer: Turner *et al.* (2007), GNSS: Dick *et al.* (2001)). Unfortunately, the ground based measurements do not resolve the spatial structures of water vapour fields. Further, they are usually limited to land areas. However, satellite remote sensing allows observations of TCWV on a high spatial resolution. Over land surfaces, TCWV derived from radiance measurements in the near-infrared (NIR) from space borne spectrometers meets the requirement needed for weather forecasts and climate studies, due to high accuracy and high spatial resolution (up to 300m) of the TCWV products. Observations from the MEdium Resolution Imaging Spectrometer (MERIS) (Bennartz and Fischer 2001, Lindstrot *et al.* 2012) on ENVISAT and the Moderate Resolution Imaging Spectroradiometer (MODIS) on Aqua and Terra (Diedrich *et al.* 2015, Gao and Kaufman 2003) can provide long time series of TCWV. These data sets such as described by Lindstrot *et al.* (2014) benefit global trend analysis or investigations of small scale phenomena as

described by Carbajal Henken *et al.* (2015). However, there are two major drawbacks of observations by polar orbiting satellites:

- Most areas are sampled only once per day or even less depending on the latitude and the swath-width of the instrument.
- Clouds are opaque in the visible and NIR spectrum. Consequently, the observations of TCWV are limited to cloud-free areas.

For the observation of the diurnal variability of TCWV ground based microwave radiometer and GNSS measurements are appropriate. The influence of clouds and precipitation can be neglected. TCWV can be derived from measurements of the Zenith Path Delay (ZPD) of ground based GNSS receivers even under cloudy conditions and on temporal resolutions up to a few minutes. We utilized 9 years of a 2-hourly TCWV data set derived from GNSS measurements in order to answer the following questions:

1. How large is the variability of the TCWV in comparison to the daily mean TCWV?
2. How representative is the TCWV at the time of the satellite overpass to the daily mean TCWV?
3. How representative is the climatology of the cloud-free TCWV to the TCWV climatology including cloudy conditions at the time of the satellite overpass?

There are few studies that examine the diurnal cycle of water vapour such as Li *et al.* (2007), Ortiz de Galisteo *et al.* (2011), Radhakrishna *et al.* (2015). However, these works are usually focused on certain regions. In this study we like to highlight the potential of a global TCWV data set and present a global analysis of the diurnal cycle of TCWV. We want to give an overview of the variability of TCWV that is needed for the interpretation of water vapour fields derived from remote sensing.

5.2 Satellite TCWV datasets

As mentioned above, the daily coverage of imaging spectrometers on sun-synchronous polar orbiting satellites is limited by the field of view of the specific instrument. MERIS on ENVISAT has a swath width of 1150 km which leads to global coverage in about 2 to 3 days. MODIS on TERRA scans the Earth in 1 to 2 days with a swath width of 2330 km. Consequently, in the lower latitudes observations take place only once every 3 days, in the middle latitudes about once per day. Information about the daily cycle of TCWV can not be retrieved from this kind of observations. However, climate monitoring requires trend analysis which is performed with the aid of TCWV from space borne spectrometers due to the global coverage. ENVISAT and Terra cross the equator at about 10:30 a.m. local time, both at descending note. TCWV retrievals that are based on radiance measurements in the NIR (Diedrich *et al.* 2015, Lindstrot *et al.* 2012) are limited to cloud-free areas where high accuracies can only provided over land surfaces (Diedrich *et al.* 2013).

5.3 GNSS TCWV dataset

Basis of our investigation is a 2-hourly TCWV data set from Wang *et al.* (2007) for the years 2003 to 2011. The TCWV was derived from ground based GNSS measurements of Zenith Path Delay (ZPD) using three different resources, including the International GNSS (Global Navigation Satellite Systems) Service (IGS) tropospheric products, U.S. SuomiNet (UCAR/COSMIC) products and Japanese GEONET (GNSS Earth Observation Network) data. All GNSS TCWV retrievals are based on the same procedure, explained shortly in the following. The TCWV is derived from the delay of the GNSS signal, that is introduced by interactions with the atmosphere. By subtracting the ionospheric, and hydrostatic attenuation, and accounting for the elevation angle of the satellites, the Zenith Wet Delay (ZWD) can be approximated, that is in the range of a few centimetres (Bevis *et al.* 1992). Subsequently, the ZWD is converted to TCWV. Although there are a number of error influences, the uncertainty of TCWV derived from GNSS is about 1 mm–2 mm (Ning *et al.* 2015).

TCWV observations from about 1000 global distributed stations for the period between 1995 to 2011 are available in the data set. However, the majority of stations did not contribute continuously over the whole time and the number of stations increases with time. In order to have a relatively complete time series of TCWV for each station, we selected only locations that provided at least 5 years of data in the period of 2003 and 2011. Figure 5.1 shows the spatial distribution and the elevation of the selected 296 stations. There is a high density in Europe and the USA and only a few stations in South America, Africa and Central Asia. Nevertheless, the spectrum of the locations is diverse. The stations are located in very dry and humid conditions at continental and coastal locations range from sea level to 1200 meters. Besides other influences, the diurnal cycle of water vapour in the lower troposphere is hypothetically linked to the diurnal cycle of temperature that is in turn mainly driven by the position of the sun. Therefore, we converted the time information in the GNSS data set (given in UTC) to the local time (LT) that is used hereafter and was derived as follows:

$$\mathrm{LT} = \mathrm{UTC} + (\varphi/15) \quad \varphi \in [-180, ..., 180] \ , \tag{5.1}$$

where φ is the longitude of the location of the corresponding station.

5.4 Diurnal cycle of TCWV

The main part of the column integrated water vapour is located in the boundary layer. Consequently, TCWV can represent the processes related to water vapour that take place in the lower troposphere. There are several mechanisms that influence the TCWV. The most important ones are: Evaporation and condensation, large-scale and local advection of moist or dry air. Considering averages over a large number of days, the large scale advective part is usually represented at all times of a day, leaving only the variations that are connected to the diurnal cycle in air temperature. With increasing surface

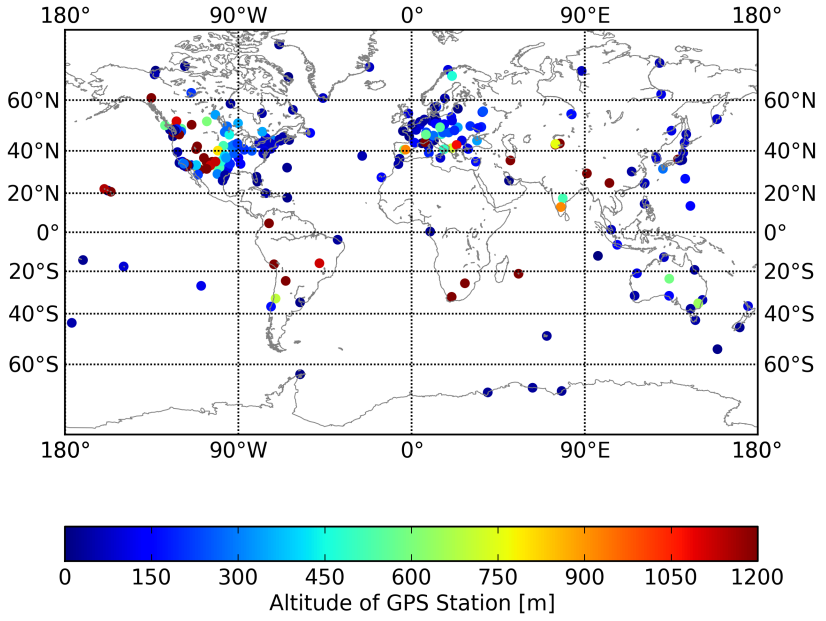

FIGURE 5.1: Global distribution and height in meters of selected GNSS stations.

temperature over the day, the evaporation can increase. At night water vapour condensates and consequently, TCWV will be decreased on average. Another influence is the advection of humid or dry air masses. Winds originate from synoptic situations or orographic circumstances. The wind is generally higher at daytime because of convection that in turn will also influence the water vapour amount. Local geographic conditions can result in circulation patterns that occur almost every day such as land- and sea breeze and mountain breeze. The differential warming between land and ocean carries moisture onshore at daytime. At night-time this circulation is reversed due to the faster cooling of the land surfaces. The climatic and geographic conditions are various for the number of stations we have selected. In some cases, these influences are dependent on the time of the year due to the annual variability of the circulation pattern. To analyse every single station concerning its diurnal cycle would exceed the frame of this paper. Consequently, a statistical approach of the evaluation of the diurnal cycle is presented in the following.

An evaluation of the diurnal variability of the TCWV anomaly from the daily mean for the 296 considered stations averaged over 9 years (2003-2011) is represented in Figure 5.2 as box plot. Black boxes and whiskers indicate a histogram of the TCWV anomaly including all stations for each 2-hour time-step. The inner quartile range (IQR) is varying between +2 % and -2 % of the daily mean TCWV (indicated by the horizontal dashed line). There is a significant minimum of the station mean TCWV (indicated by the horizontal bar in the boxes) between 6 LT and 10 LT and a maximum between 16 LT and 20 LT with an amplitude around 1 %. The variation of 95 % of the stations is ranging between +5 % and -5 %.

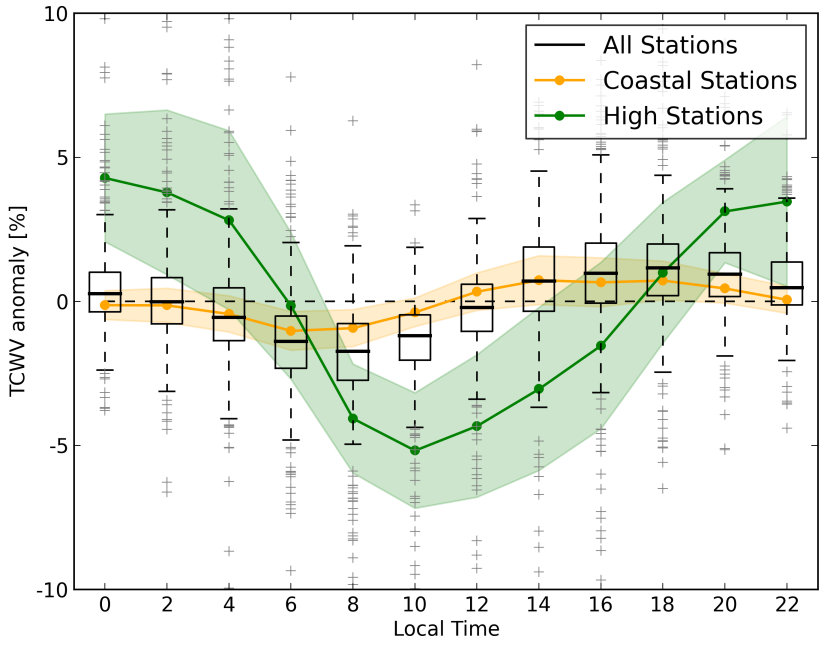

FIGURE 5.2: Boxplot of TCWV anomalies from the daily mean in % for all stations and the period between 2003 and 2011. The range of the black boxes indicate the interquartile range (IQR), containing 50 % of the data points (each point represents one stations). The horizontal bar within the boxes represent the median; vertical bars (whiskers) indicate the reach of 95 % of the data points; and grey pluses show outliers. Green line: Mean daily cycle of TCWV of all high stations (greater than 800 m altitude); Orange line: Mean daily cycle of TCWV for coastal stations. See text for detailed description.

In order to analyse the influence of the location to the averaged daily cycle of TCWV, two subgroups of stations were selected: 52 Coastal stations that are situated within 5 km of a coast of the ocean or large lakes and below 800 m elevation (indicated orange in Figure 5.2, 5.3), and 44 high GNSS stations that are situated above 800 m (indicated green). The coloured lines in Figure 5.2 show the mean diurnal TCWV anomaly of the two groups including the range of the standard deviation as coloured shading. The diurnal variability of the high stations is most pronounced in this comparison, peaking at 0 and 10 LT with an amplitude of about 5 %. The coastal station diurnal mean TCWV anomaly is following the overall mean TCWV anomaly of about 1 %. The variation of the averaged diurnal cycle between the high stations is larger than between the coastal stations, represented by the standard deviation.

In order to get the global view on the averaged daily variability of TCWV we derived measures that indicate the shape and amplitude of the mean diurnal cycle of each GNSS station. In Figure 5.4 the season-averaged amplitude, meaning the difference between the maximal TCWV and the daily mean TCWV, of the daily cycle of TCWV is plotted for each station. The first obvious feature is that the amplitude of the diurnal cycle is increasing with decreasing latitude and the maximum of the zonal mean amplitude is

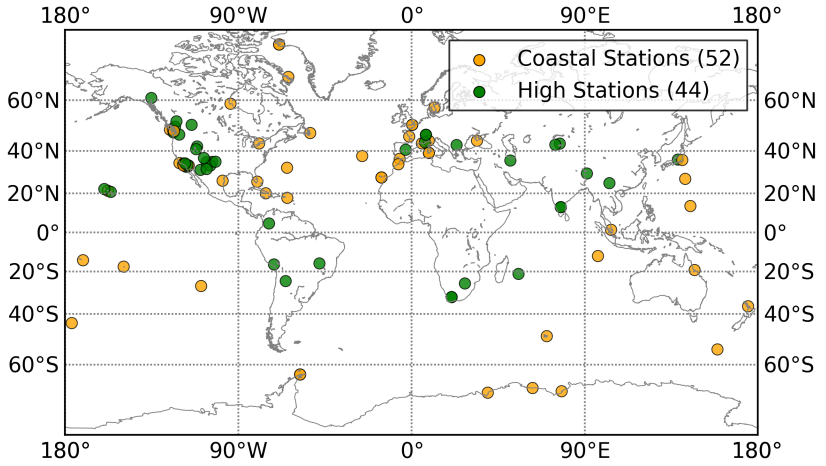

FIGURE 5.3: Location of the stations that where selected for coastal (orange) and high stations (green).

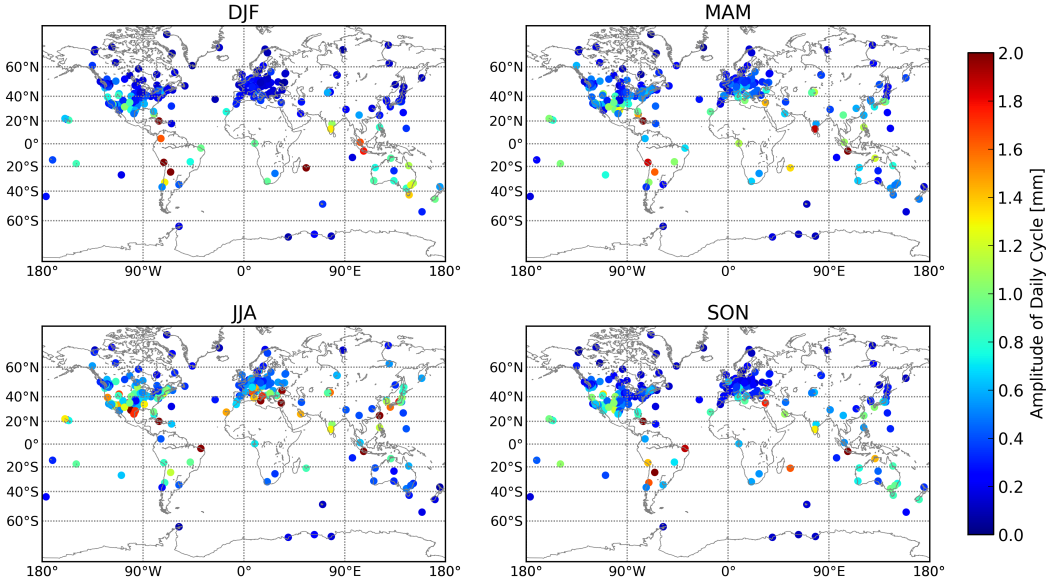

FIGURE 5.4: Season averaged amplitude of the daily cycle of TCWV for each GNSS station in mm.

moving north in the north-summer and south in north-winter. This can be explained by the annual variation of the lower tropospheric temperature. Furthermore, the amplitude ranges from 0.1 mm to 0.8 mm in the middle and high latitude to 2 mm for stations in the tropics and mid-west of the USA. In order to study how much the daily cycle constitutes to the daily mean TCWV, the anomalies from the daily mean are presented in Figure 5.5, averaged again over the seasons. It shows, that for most of the stations, the daily variability is only in the range of 1 %–5 %. For most of the stations with higher altitudes the anomalies are increased and range up to 20 % that is consistent with the findings in

Figure 5.2. In general, the amplitude of the daily anomalies is not following the global temperature distribution.

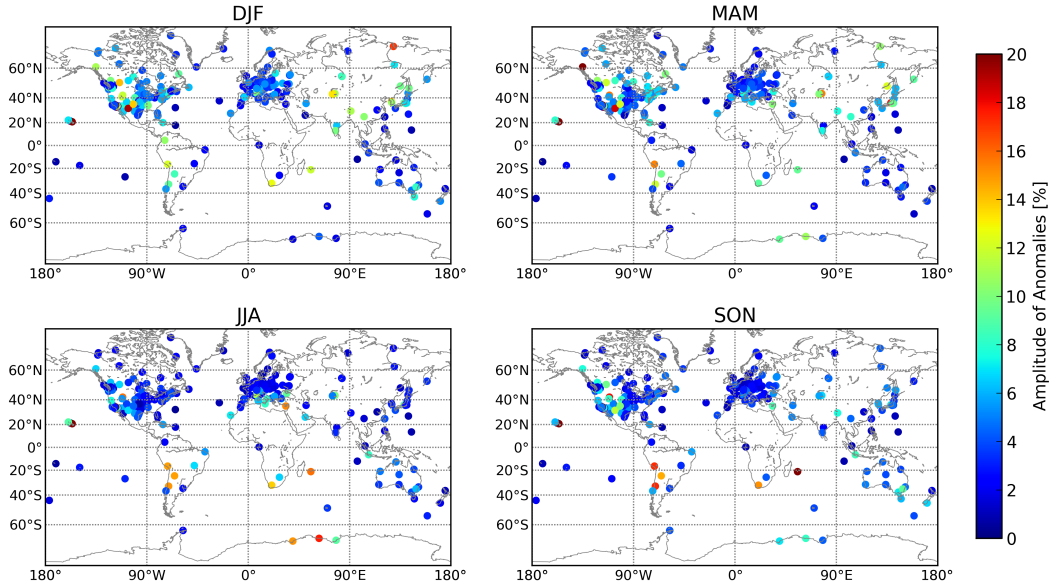

FIGURE 5.5: Season averaged amplitude relative to the daily cycle of TCWV for each GNSS station in %.

Another interesting feature of the diurnal cycle of TCWV is the time, when the TCWV reaches its maximum or minimum. In Figure 5.6 and 5.7 the local time of occurrence of the maximum TCWV respectively the minimum TCWV of the averaged daily cycle for every season is shown. At the majority of the stations a similar shape of the diurnal cycle appears resulting in the same times of the maximum and the minimum in each season. This is demonstrated by the reddish and pinkish colors on the maximum plot and dominating green colors in the minimum-plot leading to a mean daily TCWV variation that is minimal in the morning between 5 LT and 9 LT and that is maximal at night between 19 LT and 1 LT that again is consistent with the mean daily cycle for all stations in Figure 5.2. However, there are stations with different characters, e.g. in the southern Rocky Mountains that peak between 3 LT and 4 LT for the maximum and between 13 LT and 16 LT for the minimum. This shape is reverse to the other stations. Additionally, most of the European stations and some stations in the mid west of the US detect a maximum that is slightly shifted to earlier times (12-17 LT) in the north spring and summer time. At the ENVISAT and Terra overpass the average TCWV for the majority of stations is still slightly below the daily mean. This is the main reason for the negative bias between the TCWV derived at 10:30 LT and the daily mean. Although only valid for cloud-free conditions, the deviations in Figure 5.10 are in the range of the absolute amplitude of averaged diurnal oscillation of TCWV.

In general, the variation of the averaged diurnal cycle of TCWV between the stations is large concerning the time of the maximum or minimum and the amplitude and is mainly dependent on the location of the GNSS station. This is consistent with Figure

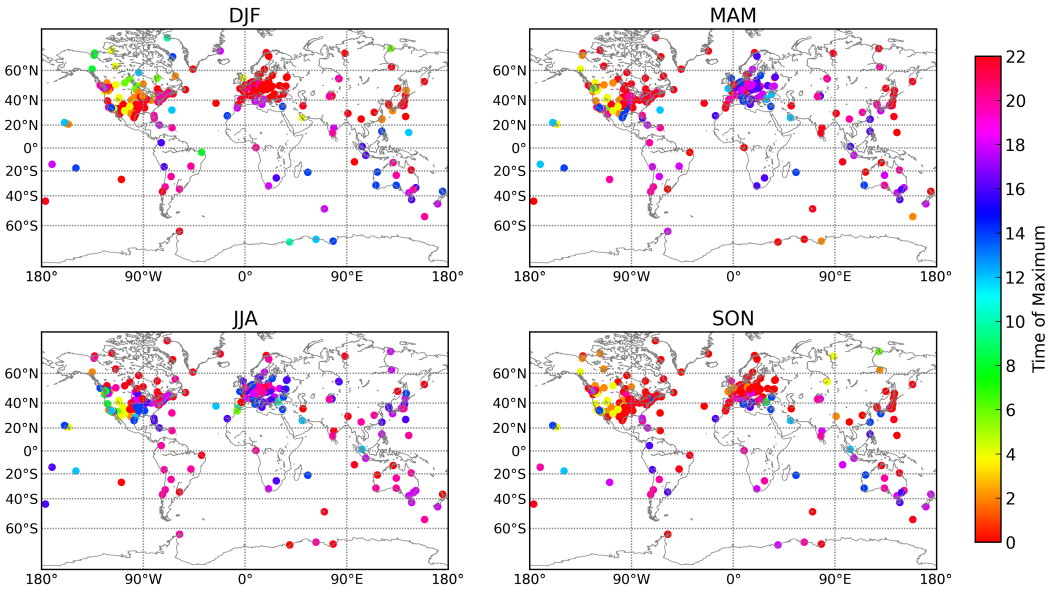

FIGURE 5.6: Local time of occurrence of the maximum of the seasonal averaged daily cycle.

5.2, where the spread of the standard deviations, boxes and whiskers indicate that the averaged diurnal cycle is varying by more than ±10 % between the stations. The averaged amplitude is only in the range of a few percent of the mean TCWV, which is again consistent with Figure 5.2.

However, this information does not quantify the individual daily variability of the TCWV. Figure 5.8 shows the TCWV for 16 days in January 2003 for the GNSS station Potsdam as dashed line. Additively, the daily mean TCWV is plotted. For better visibility, the positive difference between the curves are filled red and the negative areas are filled blue. The comparison reveals that the daily cycle of TCWV is different for every day. In order to quantify this variability, the daily standard deviation (DSD) of the TCWV as anomaly from the daily mean, averaged for each station is plotted on the right panel in Figure 5.9 as frequency density plot. The DSD for each station ranges between 5 % and 35 %. The median is at 15.1 % (equivalent to 2 mm TCWV; indicated by the dashed vertical line) and 80 % of the stations show a DSD between 11 % and 21 % (indicated by the green color). Additionally, the location of the percentile groups is plotted in the left panel of Figure 5.9. GNSS stations with low DSD (10th percentile; indicated blue) are generally distributed in the tropical region. This region is known to have a low daily variability of temperature and humidity. The outliers with high SDS (red) are not limited to special climatological regions.

Summarizing, the averaged anomaly of the daily mean TCWV varies only between 1 % and 5 % for the majority of stations. This is an important information for the interpretation of climatologies of TCWV from observations of polar-orbiting satellites

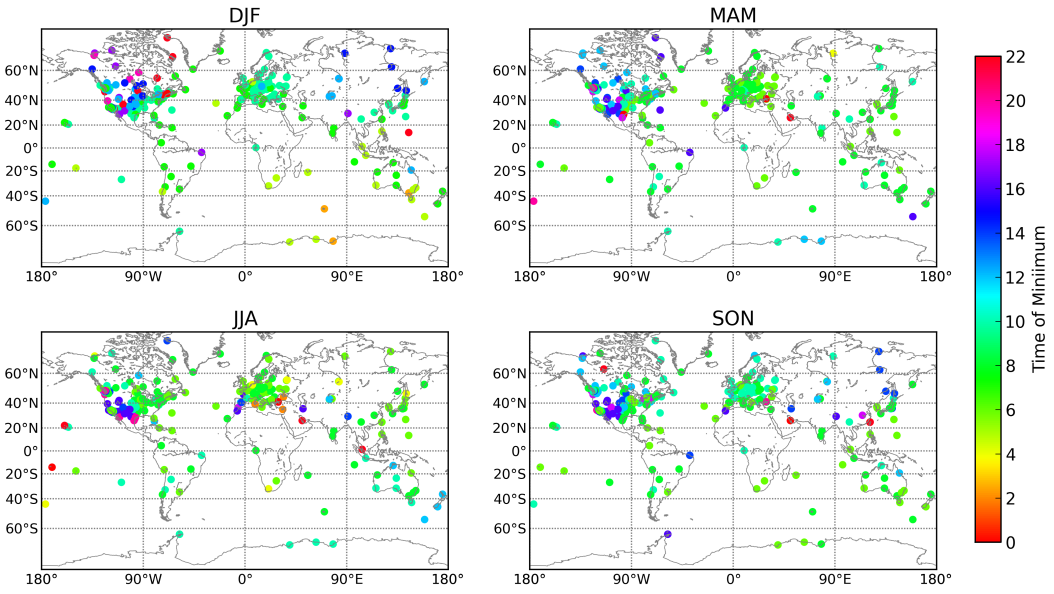

FIGURE 5.7: Local time of occurrence of the minimum of the seasonal averaged daily cycle.

(see next section). However, the variability around the daily mean for an individual day is significantly higher, on average up to 35 %.

5.5 Representativeness of TCWV at 10:30 LT to daily mean TCWV

Whether one observation at the overpass time of the satellite is representative for the daily mean TCWV has been investigated. The bias between the TCWV (observed at 10:30 LT) and the daily mean TCWV (for all days, that were cloud-free at 10:30 LT) was averaged for each GNSS station and shown in Figure 5.10. The right plot represents the distribution of frequency of the bias for each station. Blue bars indicate the bias classes that are within the 10th percentile of the distribution and red bars above the 90th percentile. The spatial distribution of the GNSS stations is shown in the left plot. A negative bias indicates that the 10:30 LT is lower than the daily mean. The number of considered stations is reduced to 202 because some stations where mostly cloud covered at 10:30 LT. Figure 5.10 shows a station-mean-bias of -0.63 mm (illustrated by the vertical dashed line in the histogram) that is within the measurement accuracy of the GNSS measurements and within the uncertainty ranges of a typical TCWV retrieval from observations in the NIR (Diedrich *et al.* 2013). Here again, the station with low biases are distributed in the tropical region, where the variability of TCWV is smaller than in other regions. In general, negative biases were derived for nearly all stations. This is consistent with the findings of the last section, where the averaged anomaly of the diurnal cycle of TCWV is negative at 10:30 LT.

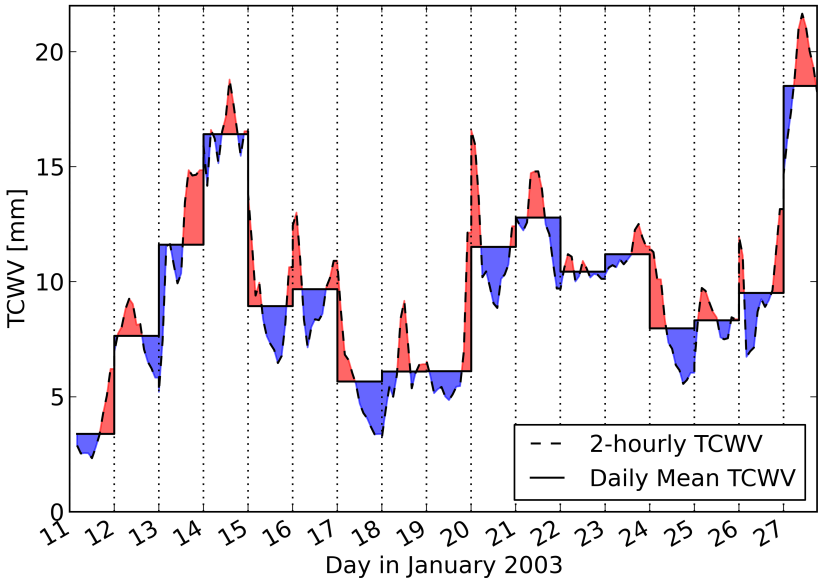

FIGURE 5.8: GNSS TCWV vor 16 days in January 2003 at the station Potsdam (POTS) in blue. Daily average TCWV in black. Anomalies are coloured (positive: red, negative: blue).

5.6 Representativeness of cloud-free monthly-mean TCWV to monthly-mean TCWV at 10:30 LT

The fact that TCWV derived from instruments like MERIS and MODIS is limited to cloud-free areas has to be accounted for in the interpretation of trend analysis. Figure 5.11 shows monthly mean TCWV derived at 10:30 LT of all considered GNSS stations for the period 2003-2011 in blue including all cases and cloud-free cases in red. There is a clear difference in TCWV between all cases and non-cloudy cases. On average, TCWV is about 25 % (about 5 mm) higher for all scenes than for clear scenes. This expected increase in TCWV for cloudy cases has been detected also in the study by Gaffen and Elliott (1993). Concerning climatological studies of absolute TCWV values, the TCWV observed at cloud-free cases is not representative for the TCWV including all cases. Nevertheless, the cloud-free and all-case TCWV are highly correlated.

5.7 Conclusions

In this investigation the representativeness of the TCWV derived from imaging spectrometers that measure radiance in the NIR on polar orbiting satellites is discussed. A TCWV data set derived from GNSS delay measurements that is hardly influenced by clouds has been used. It turns out that on average the TCWV observed at 10:30 LT on cloud-free cases is generally lower than the daily mean TCWV. The bias of -0.65 mm (-4 %) is in the range of the mean amplitude of the diurnal cycle. The monthly mean

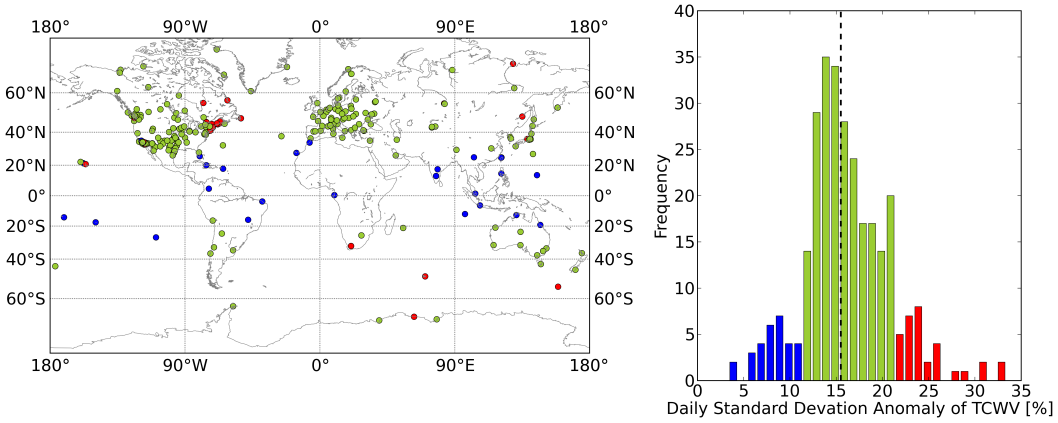

FIGURE 5.9: Mean daily standard deviation anomaly from the daily mean TCWV in %. Right plot: Histogram of the bias, red bars indicate the classes that are in the 10th percentile, red bars indicate classes that are above the 90th percentile; the vertical dashed line illustrates the position of the station-median of the standard deviation anomaly. Left plot: Spatial distribution of stations coloured with the three percentile classes.

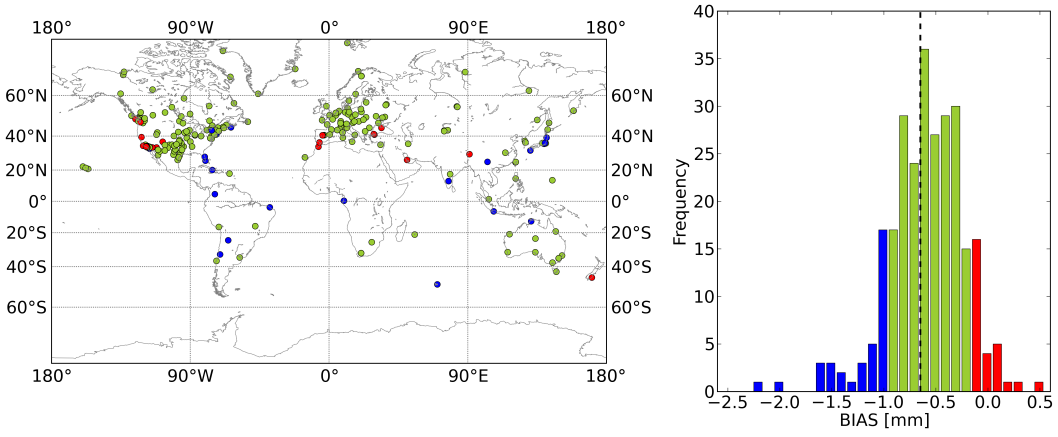

FIGURE 5.10: Bias for each station between the TCWV observed at 10:30 LT and the daily mean TCVW for all cases, that were cloud-free at 10:30 local time. Right plot: Histogram of the bias, red bars indicate the classes that are in the 10th percentile, red bars indicate classes that are above the 90th percentile; the vertical dashed line illustrates the position of the station-median of the bias. Left plot: Spatial distribution of stations coloured with the three percentile classes.

TCWV observed at 10:30 LT constrained to cloud-free case is significant lower than the monthly mean TCWV of all cases by about 25 % (5 mm). Nevertheless, the diurnal cycle is only a few percent of the daily mean TCWV for most of the stations. On average, for the majority of stations, TCWV peaks at the evening and is minimal in the early morning local time. However, the variability on an individual day is much higher. The daily standard deviation averaged for every station is about 15 % of the daily mean.

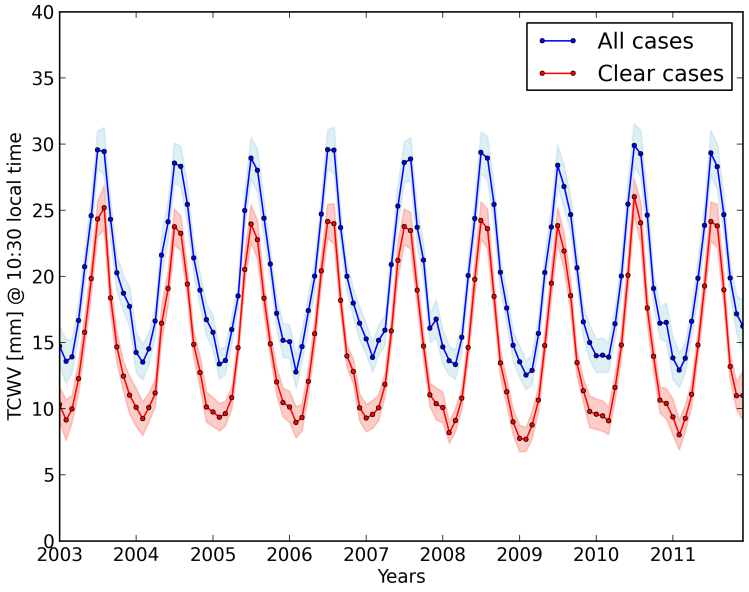

FIGURE 5.11: Monthly mean TCWV of all selected stations for cloudy scenes in blue and non-cloudy scenes in red lines.The shading indicates the 95 %-significance interval.

Summarizing, the biggest influence on the representativeness of observed TCWV from polar orbiting satellites is the constraint to cloud-free areas. The time of observation is a minor factor and in case of the MODIS and MERIS overpass negligible, when averaging over time. The used GNSS-TCWV data set, collocated with cloud information data from satellites, offers a lot of potential for studies concerning for example the interaction between clouds and water vapour. As precipitation is also strongly influencing the water transport and consequently to TCWV, the collocation of rain gouge data can also serve a more detailed view of the reasons for the individual diurnal viability of TCWV.

Chapter 6

Statistical relationship between cloud properties and total column water vapour

6.1 Introduction

In Chapter 5, the impact of clouds on the observation of TCWV derived from measurement in the NIR has been assessed briefly. Clouds significantly influence the remote sensing of TCWV, especially in the VIS to IR spectral range. These satellite products of TCWV are used for the monitoring of the Earth's climate. Furthermore, they are assimilated into NWP models. Additionally, TCWV data sets are used to evaluate the outcome of the models although they are constrained to cloud-free cases. Trend analysis of TCWV with observations is also influenced by the presence of clouds.

On average about 70 % of the Earth's surface is covered by clouds (Stubenrauch *et al.* 2013). Consequently, they play a key role in the climate, especially in the radiation budget of the Earth. The temporal and spatial scales of clouds range from few hundred meters and a few minutes to a hundreds of kilometres and day with high variability. Climate and weather prediction models face the challenge of exactly represent cloud forming processes. Because of the low spatial resolution of the models, small scale atmospheric processes such as cloud evolution can not be resolved and are consequently parametrised as fractional cloud cover , using probability density functions of the specific humidity (Quaas 2012). Generally, evaluation studies reveal that the cloud representations in NWP models is biased and very much dependent on the parametrization scheme of the individual model (Eikenberg *et al.* 2015, Illingworth *et al.* 2007). In order to better understand the cloud processes on a global scale accurate observations of clouds are needed. The remote sensing of clouds and their optical parameters from satellites (Henken *et al.* 2014, Platnick *et al.* 2015) can contribute to that. In the HD(CP)^2 project[1], observation

[1] `http://www.hdcp2.eu`

and model communities are brought together in order to improve the understanding of cloud processes and the representation of clouds and the hydrological cycle in the models. This study intends to contribute to that.

Clouds form from water vapour through convection, which is initiated by heating of the surface or lifting processes and fuelled by the lapse rate of the temperature and the dew point in the boundary layer (Sherwood *et al.* 2010). Only a few percent of the total amount of water vapour in the column is converted into cloud water path (CWP). From this small portion only a few percent can form precipitation. However, an increased TCWV is not automatically resulting in an increased cloud cover or precipitation. Studies about the quantitative relation between TCWV and cloud amount are sparse (e.g. Gaffen and Elliott (1993)).

In this study the L2-Cloud-Product from MODIS measurements was used to quantify the statistical relationship between cloud properties and TCWV from observations. Additionally, data from a high resolution local NWP model COSMO-DE and reanalysis data (ERA-Interim) were collocated in order to compare the statistical relationship between clouds and TCWV found from model data to the observation. These studies can help to improve the cloud parametrizations of the models, which will in turn improve the computation of radiative fluxes, precipitation forecasts etc. As the model data is limited to the larger German area, this study is only valid for this environment and represents a first step to a large-scale evaluation of the relation between TCWV and cloud properties on a statistical level. The analysis is an example of the various applications of observed TCWV

6.2 Data sets and collocation method

On the observation side the MODIS MOD06-L2 product was spatially and temporally collocated with 5 years of TCWV values derived from GNSS ZTD measurements for German stations (see Figure 6.1). On the model side TCWV and cloud parameters where extracted for the same points of time from COSMO-DE analysis and ERA-Interim reanalysis. The data sets will be described in detail hereafter.

MODIS cloud product

The collection 6 of the MODIS cloud product (for Terra: MOD06-L2; for Aqua: MYD06-L2) is a sophisticated and well established data set that contains the cloud mask, cloud-top properties (pressure, temperature, phase, and height), and cloud optical properties (optical thickness, effective particle radius), and water path for both liquid water and ice clouds on a pixel basis (Platnick *et al.* 2015). The MODIS cloud product is based on measurements in the visible, NIR, and IR and is continually improved over the years. However, the retrievals face several challenges such as:

- snow cloud ambiguity

- ice and water cloud ambiguity
- multilayer clouds
- the fact that the satellite only observes the top of the cloud
- sub-pixel clouds

Consequently, the data set does not provide cloud property for every pixel that was detected as a cloudy pixel. This fact has to be accounted for in the interpretation of the data.

Besides the cloud mask, the following cloud properties where used in this study: cloud phase, total cloud water and ice path (CWP) and cloud top pressure (CTP). The CTP is only provided on a 5 km x 5 km resolution and has been interpolated to the 1 km x 1 km grid. MODIS-Data from both Aqua and Terra spacecrafts was used for this study (see Chapter 3 for detailed information about MODIS).

GNSS data set

Five years (2008-2012) of TCWV values derived from measurements of the atmospheric delay of microwave signals from GNSS satellites has been provided by the *Geoforschungszentrum Potsdam*. For detailed description of the general retrieval procedure see Chapter 2. In contrast to the GNSS-TCWV data set that was used in Chapter 5 this record provides TCWV on a 15 minute resolution for stations distributed only in Germany (Figure 6.1) (Dick *et al.* 2001, Gendt *et al.* 2004).

COSMO-DE

NWP analysis data from the COSMO-DE model for five years (2008-2012) were provided by *Universität zu Köln*. COSMO-DE is a non-hydrostatic NWP model, covering Germany and parts of its neighbouring countries (Figure 6.2). Short-range numerical forecasts are provided every 3 hours (00,03,06,09,12,15,18,21 UTC) on a grid with 50 vertical layers ranging from 10 m above ground to 22 km above mean sea level. The horizontal dimension is 421x461 grid points resulting in a resolution of 2.8 km, allowing the prognostic simulation of deep moist convection. However, shallow convection can not be resolved and is consequently parametrized separately in sub-grid variables. COSMO-DE is initialized with the boundary conditions of a 7 km COSMO model (COSMO-EU), which itself is nested into a global model. Besides traditional meteorological variables such as temperature, wind, and humidity, the data assimilation module of COSMO-DE includes high-resolution radar data, snow depth and sea surface analysis. Further description of the model is given by Baldauf *et al.* (2011).

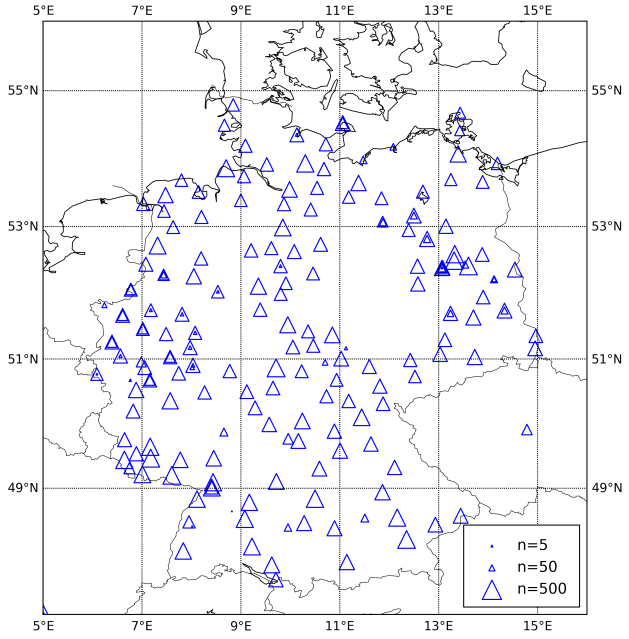

FIGURE 6.1: Location of the considered GNSS stations. The size of the markers indicate the number of contributed cases.

ERA-Interim

The ERA-Interim reanalysis data set ranges from 1929 to present and is being continued in real time. The spatial resolution of the model is about 80 km (T255) in 60 vertical levels ranging from ground to 0.1 hPa (64 km). Several data sets, including satellite data is assimilated into the model using four-dimensional variational analysis (4D-Var). A detailed summary of the model specifics can be found in Dee *et al.* (2011). For this study five years of TCWV and cloud information data was extracted for the analysis time steps 00,06,12,18 UTC and temporally and spatially collocated.

Collocation procedure

Due to the various spatial resolutions of the data sets, the following collocation method was performed.

1. For each GNSS station and each day the matching Aqua and Terra overpass time was found and the corresponding GNSS TCWV value was selected within a 15 minute range.

2. Statistics of the cloud properties of the MOD06-L2 product were performed for the corresponding 21x21 pixels centered at the location. An area of about 20 km

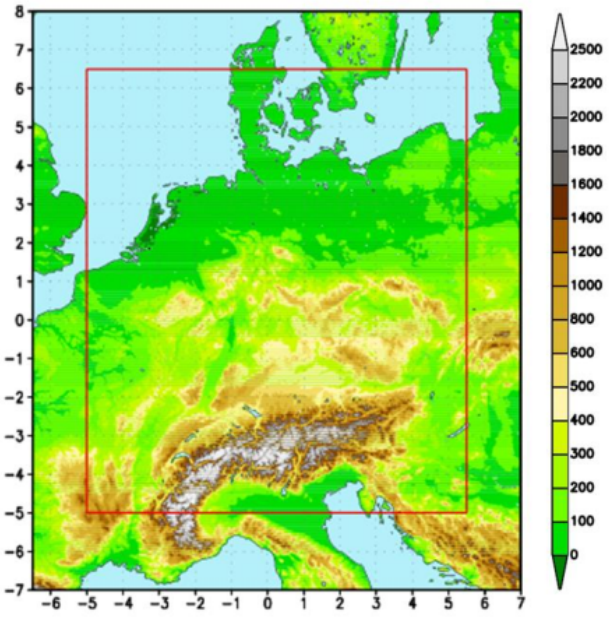

FIGURE 6.2: Topographic map of the COSMO-DE model domain (red box) covering an area of 1200 kmx1300 km of central Europe (`http://www.dwd.de`).

in diameter was chosen in order to account for the footprint of the GNSS measurements due to the viewing zenith angles of the used satellites and to allow the detection of the variability of cloud properties.

3. For the COSMO-DE data set the matching area of 7x7 grid boxes was selected that has approximately the size of the MODIS tile. The data was linearly interpolated between the two corresponding COSMO-DE time-steps to the time of observation of the GNSS TCWV.

4. Due to the large grid box size of the ERA-Interim data, only one grid cell was collocated and temporally interpolated.

A data record of 96150 cases emerges from the collocation of the data sets for the five years from 2008 to 2012 that enables a statistical analysis with sufficient representativeness.

Cloud parameters

The cloudiness of a scene is approached differently in the observations in comparison to the models. Multi spectral measurements in the VIS, NIR and IR are used to derive a cloud-mask. For the majority of cases these procedures provide good confidence. However, the differentiation between clouds and clear snow areas is uncertain. Additionally, sub-pixel clouds are problematic for the determination of a cloud mask, especially at

TABLE 6.1: Model definition of 3 height classes and their vertical range in hPa:

Cloud class	maximum CTP [hPa]	maximum CTP [hPa]
High	100	400
Medium	400	800
Low	800	1000

TABLE 6.2: Overview of used parameters and their original temporal and spatial resolution.

		Resolution	
Parameter	Source	temporal	spatial
TCWV	GPS	15 minutes	$\sim$ 2 km
	COSMO-DE	3 hours	2.8 km
	ERA-Interim	6 hours	$\sim$ 80 km
CWP	MODIS	2 times daily	1 km
	COSMO-DE	3 hours	2.8 km
	ERA-Interim	6 hours	$\sim$ 80 km
CTP	MODIS	2 times daily	5 km
	COSMO-DE	3 hours	2.8 km
	ERA-Interim	6 hours	$\sim$ 80 km
Cloud phase	MODIS	2 times daily	1 km
	COSMO-DE	3 hours	2.8 km
	ERA-Interim	6 hours	$\sim$ 80 km
Cloud-mask	MODIS	2 times daily	1 km
cloud cover	COSMO-DE	3 hours	2.8 km
cloud cover	ERA-Interim	6 hours	$\sim$ 80 km

the boarders of larger clouds. The MODIS L2-product includes information of whether a pixel is partly cloudy. Nevertheless, in this study only the pixels that are full-cloudy were counted as cloudy and divided by the number of clear pixel for each MODIS tile in order to derive a fractional cloud cover .

In most of the NWP models clouds evolve if a certain threshold of relative humidity is reached. A fractional cloud cover is derived from the subgrid-scale variability of the total water content. The cloud cover of a grid cell (ranging from 0 to 100 %) is increasing with higher relative humidity. For both COSMO-DE and ERA-Interim, total cloud cover and a cloud cover for the lowest, medium, and high air layers are provided (see Table 6.1). The cloud water path (CWP) is a measure of the total amount of water present between the bottom and top of the atmosphere that is the vertical integral of the liquid and ice water mixing ratio.

Table 6.2 shows an overview of used parameters and their original temporal and spatial resolution. Nevertheless, the collocated data set contains maximal two cases per day (for the overpasses of Aqua and Terra).

6.3 Results

Annual cycle of TCWV and CWP

In the following, the comparison between observed and modelled annual cycles of different extracted parameters is presented. Figure 6.3 shows a weekly climatology of TCWV of the three data sets for the full time series. The colors of the graphs indicate the data sets, here and in the following figures (Observations in blue, COSMO-DE in red, and ERA-Interim in green). The coloured shading of the graph indicate the 95 % confidence interval for the weekly mean value taking the standard deviation into account. Figure 6.3 clearly shows the annual cycle of TCWV with low values about 10 mm in the winter (weeks 1 to 9 and 49 to 52) and high values about 25 mm in summer (weeks 25 to 35). There are some significant variations modulated onto the annual cycle, presumably resulting from the influences of the oscillating general circulation direction. This circulation transports either mid latitude cyclones loaded with humidity and precipitation from the Atlantic ocean or redirects them due to a stationary high pressure system located over middle Europe. This influence by the general circulation is well captured by COSMO-DE, following the observation curve. Although the ERA-Interim TCWV agrees generally with the other data sets in the characteristic of annual cycle, the weekly or monthly variations are not represented in detail. Direct comparison reveal that COSMO-DE and ERA-Interim have a dry bias in comparison to the observation of about 1 mm whereas COSMO-DE agreement is significantly higher than ERA-Interim (root mean square error for COSMO-DE vs. GNSS 1.9 mm and for ERA-Interim vs. GNSS 5.7 mm; Figure 1 in the Appendix).

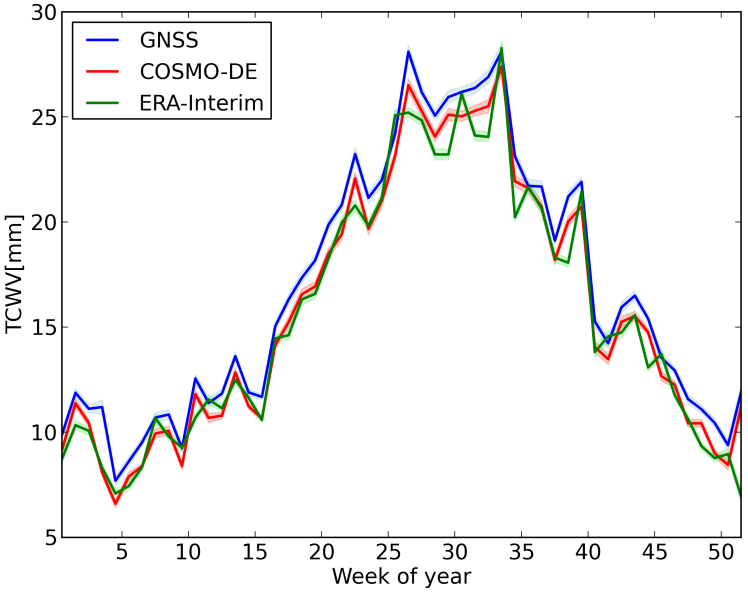

FIGURE 6.3: Weekly climatology of TCWV at the MODIS overpass times for 2008-2012 in [mm]. Shaded areas indicate the range of the 95 % confidence interval.

As mentioned above, the MODIS data set provides the cloud-top phase on a pixel basis. In Figure 6.4 the weekly climatology of TCWV for cases with mostly water clouds (blue line), ice clouds (black line), and cases with uncertain or mixed phases (orange line) is shown. Cases that contain more than 75 % water cloud pixels are flagged as water cloud cases. The same is applied to ice clouds. Pixel with mixed or uncertain cloud phase are condensed in the uncertain phase category. Only cases with minimum 30 % total cloud cover are considered. On average, TCWV is higher for cases with mostly ice clouds than for water clouds. The number of cases for each cloud-top-phase category is plotted at the bottom of Figure 6.4. It reveals, that cases with unique cloud-top-phases are less likely than cases with mixed cloud phases. There is a small increase of ice cloud cases in the winter presumably connected with the increased likelihood of ice particles in clouds due to the lower temperatures.

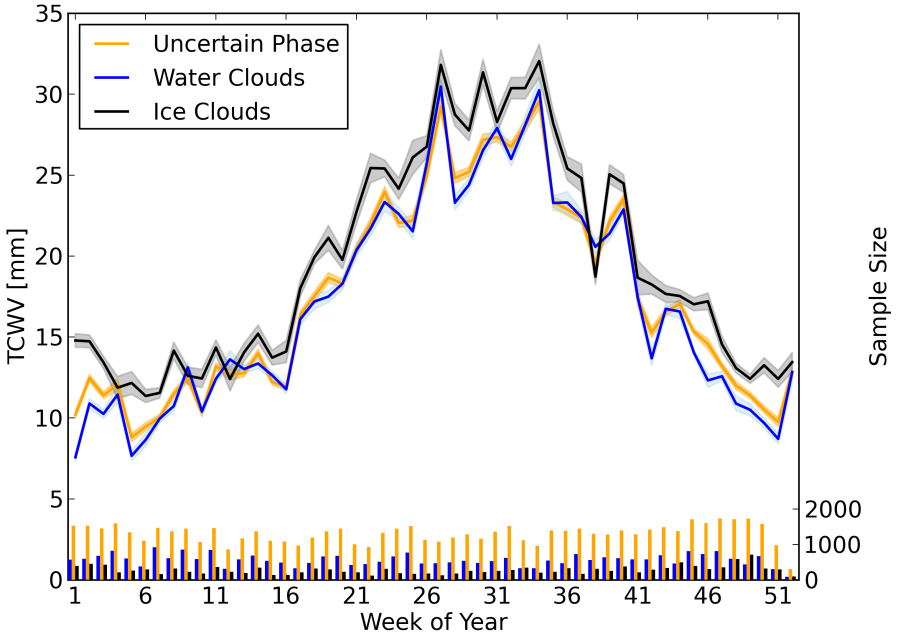

FIGURE 6.4: Weekly climatology of GNSS TCWV at the MODIS overpass times for 2008-2012 for cases with mostly water clouds (blue), ice clouds (black) and uncertain phases (orange) (phase information from MODIS). The bars at the bottom indicate the number of contributed cases for each cloud phase. Shaded areas indicate the range of the 95 % confidence interval. See text for detailed description of the cases.

Figure 6.5 shows the weekly climatology CWP for the three data sets for all cases. For the MODIS record only cases that are flagged as snow-free were regarded in order to exclude cases that are problematic for the retrieval of the CWP. Generally, ERA-Interim and COSMO-DE agree, that there is no significant annual cycle of the weekly mean CWP. For MODIS there is an increase of CWP in the winter months (week 1 to 4 and 48 to 52). This is presumably due to the low sun altitude (high sun zenith angles) in the winter time, especially of the Terra cases (overpass time between 8 and 10 a.m. local time). First, the low illumination increases the SNR of the radiance measurement and second, shadow effects increase the uncertainty of the CWP retrieval. Third and

as a consequence, contamination by snow pixels is more likely. The number of cases (indicated by the bars at the bottom of Figure 6.5) are sufficient high in order to derive reliable mean CWPs and also similar for the three data sets for a fair comparison. The general decrease in the number of cases in the last two weeks of the year is due to the lack of measurements of the GNSS-dataset at the end of the years 2008, 2009, and 2012. The general comparison of the annual mean CWP of the three data sets reveals significant differences. The mean CWP from COSMO-DE fluctuates around 50 g/m^2, whereas the CWP from ERA-Interim is at 100 g/m^2 and the CWP derived from MODIS observations varies around a yearly mean of 150 g/m^2. The largest fluctuations are present for the MODIS CWP ranging up to 300 g/m^2. The deviations between observations and models could result from the fact, that the fraction of sub-grid clouds is not included in the CWP.

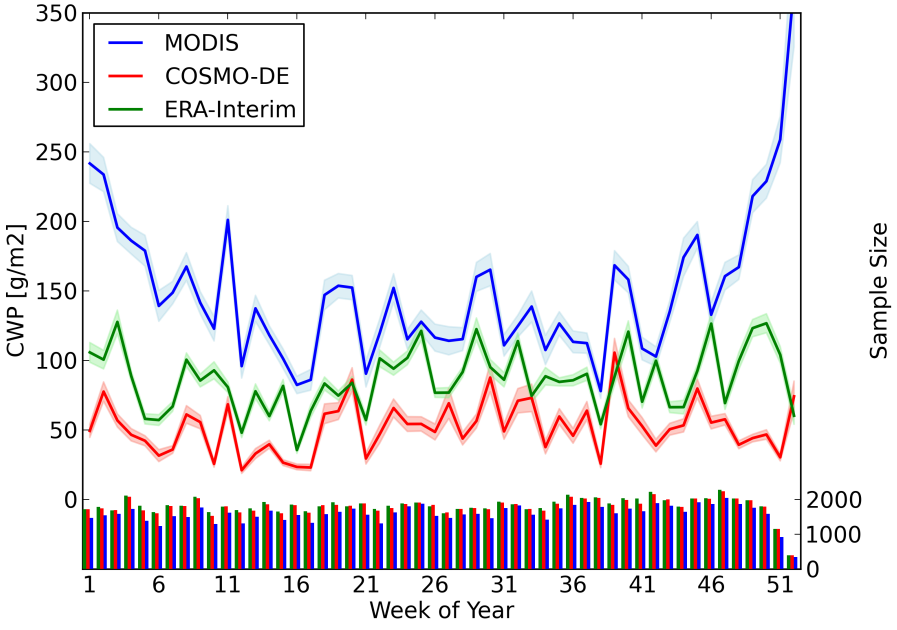

FIGURE 6.5: Weekly climatology of CWP at the MODIS overpass times for 2008-2012 in g/m^2 for all cases at MODIS overpass time. The bars at the bottom indicate the number of cases for the three data sets. For detailed description see the text.

TCWV and clouds

In the following, the statistical relationship between the TCWV and cloud parameters for both observation and models is presented. Figure 6.6 shows a histogram of the TCWV anomalies for all cases in solid lines and for cloudy cases (cloud cover higher than 75 %) in dashed lines. The TCWV anomaly $\mathrm{TCWV}_{\mathrm{anom}}$ for each time step t_d is derived by the division of the TCWV at the time step and climatological $\mathrm{TCWV}_{\mathrm{clim}}$ of the corresponding week t_w (from Figure 6.3):

$$\mathrm{TCWV}_{\mathrm{anom}}(t_d) = \mathrm{TCWV}(t_d)/\mathrm{TCWV}_{\mathrm{clim}}(t_w) \times 100 \tag{6.1}$$

The histograms in Figure 6.6 represent probability density functions (PDF) of the TCWV anomaly that is independent of the annual variation of the TCWV. The solid lines have an asymmetric shape shifted to dryer cases (below 100 % anomaly). All three data sets have a similar shape of the PDFs for all cases.

Slightly different shapes reveal, when considering only cloudy cases (dashed lines). For the observations (TCWV from GNSS and cloud-mask from MODIS) generally the maximum of the histogram is significantly lower due to lower number of cases and is slightly shifted to higher anomalies. At approximately 200 % nearly all cases are cloudy. The PDF for the ERA-Interim data set agrees with this relationship, although there are more cases between 120 and 220 % TCWV anomaly in comparison to the observations. The COSMO-DE statistic reveal that there are significant more cases with cloud cover higher than 75 % and there are more cases with higher TCWV anomalies. At about 200 % TCWV anomaly almost all cases are cloudy. The differences between observations and COSMO-DE model can be either a first clue for the inaccurate cloud formation representation in the COSMO-DE model or could result from the different determination of cloud cover (MODIS cloud mask versus COSMO-DE cloud cover). The latter is rather unlikely because ERA-Interim is agreeing very well with the observations and uses the same description of cloudiness. Böhme *et al.* (2011) found out that COSMO-DE generally produces more clouds and suggests that there is an overestimation of the probability of high clouds in the model. A first hint of this feature was also recognized in this comparison. When extracting the cases where COSMO-DE detects mostly high clouds, the agreement between the PDFs of the cloudy cases is increased distinctly (Figure 2 in the Appendix). Generally, the shift of the maximum of the PDFs between all cases and cloudy cases is related to increased TCWV for cloudy cases (as already captured in Chapter 4). How TCWV is related to cloud cover is presented in the following.

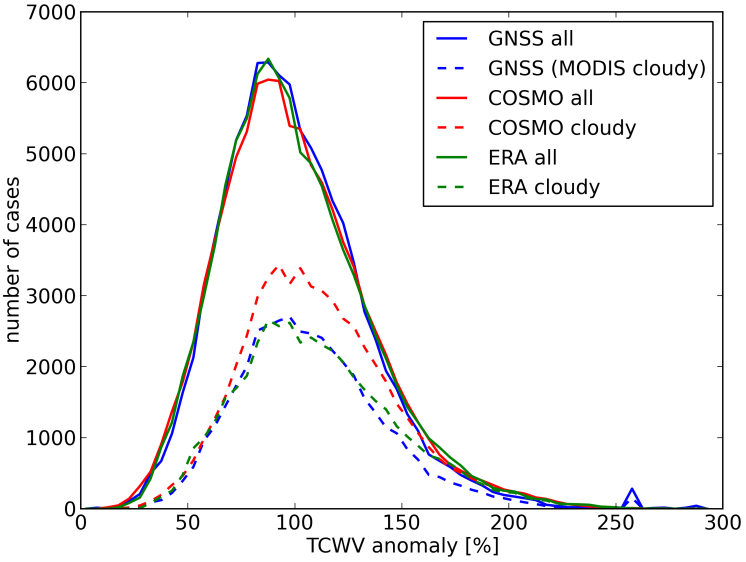

FIGURE 6.6: Histogram of the TCWV anomalies in % for all cases (solid lines) and for cases with cloud higher than 75 % (dashed lines). For detailed description see the text.

Figure 6.7 shows the seasonal mean TCWV as a function of cloud cover . The low cloud cover class (0-20 %) is indicated by bright colors and the high cloud cover class (80-100 %) is indicated by dark colors. For the observation, meaning the GNSS TCWV and MODIS cloud-mask (upper left plot with blue colors), a clear relationship of increasing TCWV with increasing cloud cover for all seasons emerges. Overall, the statistics for COSMO-DE represent this relation, but the absolute values of the seasonal TCWV are significant smaller for cloud classes below 80 % cloud cover in comparison to the observations. The same applies to the ERA-Interim data and reflects the dry bias between observations and models. The relationship of increasing TCWV with increasing cloud-over is not represented in the ERA-Interim data set for the cloud classes between 20 and 80 %. This could be due to the fact that there is only a comparably small number of cases of those cloud cover classes, that is confirmed in the following.

In Figure 6.8 the direct comparison of the cloud cover between the models and the observations is shown for each cloud cover class. On the left panel of the figure, the comparison to COSMO-DE data reveals that observations and models agree that there are significant more cases that are either clear or totally covered by clouds. However, COSMO-DE tends to produce more cases with cloud cover higher than 80 % that is consistent with Figure 6.6 (over 50 % of the cases are in that cloud cover class, indicated by the fractions at the right of the plot). Overall, observations and models agree in 48 % of all cases (sum of all numbers in the bisector line, indicated by the grey number in the top right corner of the plot). For ERA-Interim, the general agreement is lower in comparison to COSMO-DE.

The statistical relationship between CWP, cloud cover and TCWV is integrated in Figure 6.9 for the model and observation data sets. Here, CWP bins are plotted as a function of cloud cover and additionally marked with the mean TCWV anomalies for each bin. Terra cases in December and January for the whole time series were omitted in order to account for the larger uncertainties of the MODIS CWP due to low sun elevations. The analysis of the left panel in Figure 6.9 that represents the observations reveals an increase number of cases with higher CWP with increasing cloud cover . As expected, the mean CWP of a scene of 21x21 pixels increases with higher percentage of clouds. Hence, the TCWV anomaly increases with higher CWP and higher cloud cover . Additionally, the TCWV anomaly increases faster with increasing CWP for higher cloud cover than for lower cloud cover . For cases with CWP higher than 200 g/m^2 the mean TCWV anomaly is higher than 120 %, meaning that for cases with high cloud cover and increased CWP, the TCWV is significantly higher than the climatological mean. There are essential differences between the observations and the COSMO-DE model-data output. For cloud cover lower than 80 %, the CWP does not exceed 140 g/m^2 and the TCWV anomalies are below 100 % for these cases. All CWP classes at cloud cover class 80-100 % show a mean TCWV anomaly of over 100 %. The statistics of the ERA-Interim output are more similar to the observations. Here again, an increase of TCWV anomaly and CWP with increasing cloud cover is recorded. Nevertheless, cloud classes below 80 % have lower CWP than in the observations.

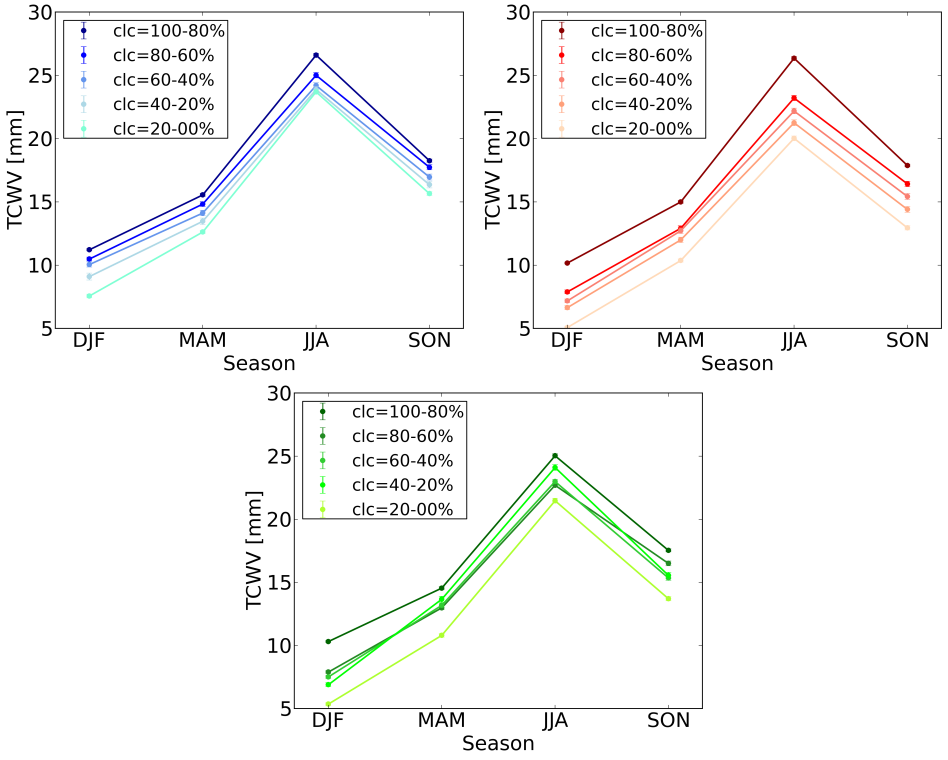

FIGURE 6.7: Seasonal mean TCWV as a function of seasonal mean cloud cover for the observations (top left Panel; blue), COSMO-DE (top right panel; red), and ERA-Interim (lower Panel; green). The markers include the interval of 95 % confidence of the mean value.

In the following, the total cloud water path is connected to the height and the extend of the cloud. High and thin clouds have a significant lower CWP than clouds that range from the lower troposphere to the tropopause such as cumulus nimbus. Figure 6.10 shows a study of the influence of the height of the cloud on the TCWV. The cloud top pressure of the MODIS observations and the cloud cover in a certain height of the models can not be compared directly due to the fact that the satellite can only detect the height of the uppermost cloud layer. Therefore, the data was transformed in the following way.

1. First, for each MODIS scene the pixel where classified in the height classes presented in Table 6.1 using the CTP. Afterwards, the number of pixel in each cloud-height class was converted to a total cloud cover . All cases that contain snow pixels were excluded.

2. The cloud cover for the three height classes of the COSMO-DE output was modified so that the sum of the cloud cover in the classes equals the total cloud cover given by the model. This was done while favouring always the highest cloud layer. For example, all grid-cells on the highest cloud layer, that have a cloud cover higher than 50 % were counted as cloudy for the highest cloud class. For the medium

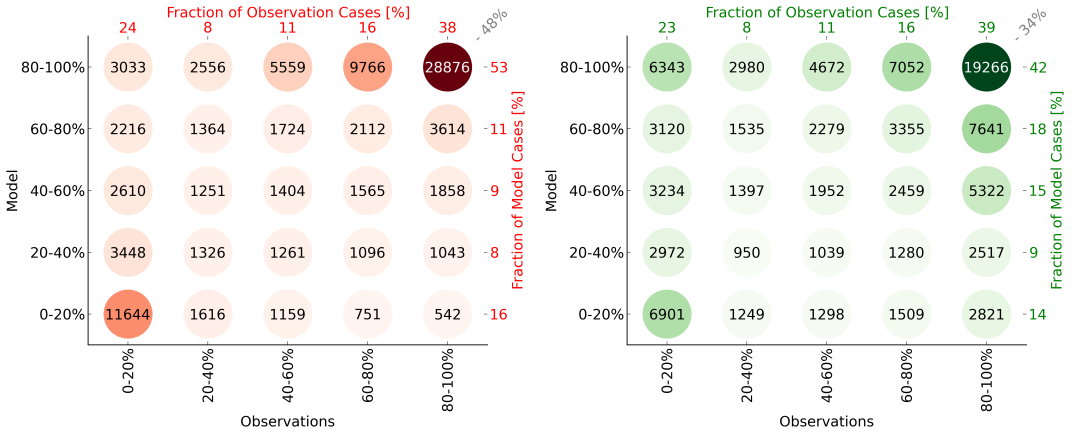

FIGURE 6.8: Number of cases for cloud cover classes of direct comparison of the total cloud cover between observations and model data output (left panel: COSMO-DE; right panel: ERA-Interim). The darker the colors, the higher the number of cases. The coloured numbers at the right and top end give the fraction of all cases in the cloud class for model or observation in comparison to the number of all cases. The grey number at the top right end indicates the percentage of cases that are in the angle bisector.

cloud layer, all grid cells that have a cloud cover higher than 50 % BUT are not detected as cloudy in the highest layer where counted as cloudy for the medium cloud layer. This procedure was applied equivalently to the lowest layer. The outcome is similar to the cloud cover seen from space.

3. Because of the large grid-cell size of the ERA-Interim data, the fractional cloud cover for each height class was used for the comparison as provided by the model.

Afterwards, the collocated cases were sorted into the three cloud-height classes if the according cloud cover in that level exceeds 50 %. This artificial threshold is expected to represent the dominating cloud-height class. For example, a cases with 62 % high cloud cover , 30 % medium cloud cover and 8 % low cloud cover is sorted into the group of high clouds. Figure 6.10 shows the frequency of occurrence of a certain cloud cover height-class as a function of TCWV anomalies. Here, for all three data sets a similar picture is revealing. For low TCWV anomalies, cases with medium cloud-height are dominant. Cases with low level clouds are sparse in this comparison. First, this could be due to the shielding effect of the higher clouds in multilayer cloud conditions and second due to the fact that clouds below 2 km are usually small cumulus clouds that do not produce cloud cover s higher than 50 %. With increasing TCWV anomalies, the fraction of high clouds is increasing while the fraction of medium and low clouds is decreasing. For cases with 180 % TCWV anomaly over 60 % of the cases are high clouds, only about 30 % are medium clouds and low clouds are rarely observed.

The good agreement between observations and models in the statistics of Figure 6.8 does not propagate into the direct comparison of the cloud heights, shown in Table

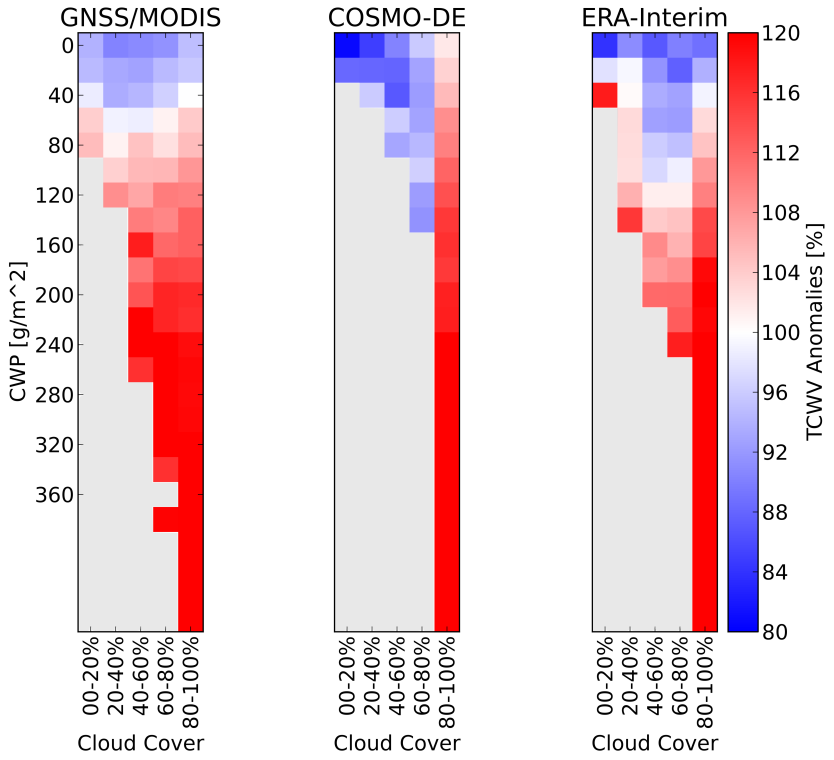

FIGURE 6.9: TCWV anomalies in % for different CWP intervals in g/m^2 as a function of cloud cover .

TABLE 6.3: Case to case agreement between observations and models for the cloud top height classes.

Cloud height	COSMO-DE [%]	ERA-Interim [%]
High	71	55
Medium	55	45
Low	30	22

6.3. The agreement is increasing with higher clouds. COSMO-DE performs better than ERA-Interim.

6.4 Summmary and outlook

In this study the statistical relationship between TCWV and selected cloud properties for observations and analysis of NWP models was assessed. Additionally, climatologies of different parameters for the observations and models were analysed. Five years of TCWV derived from German GNSS receivers were collocated with the MODIS-L2 cloud product for the observations. For the models, analysis data of the corresponding grid cells of

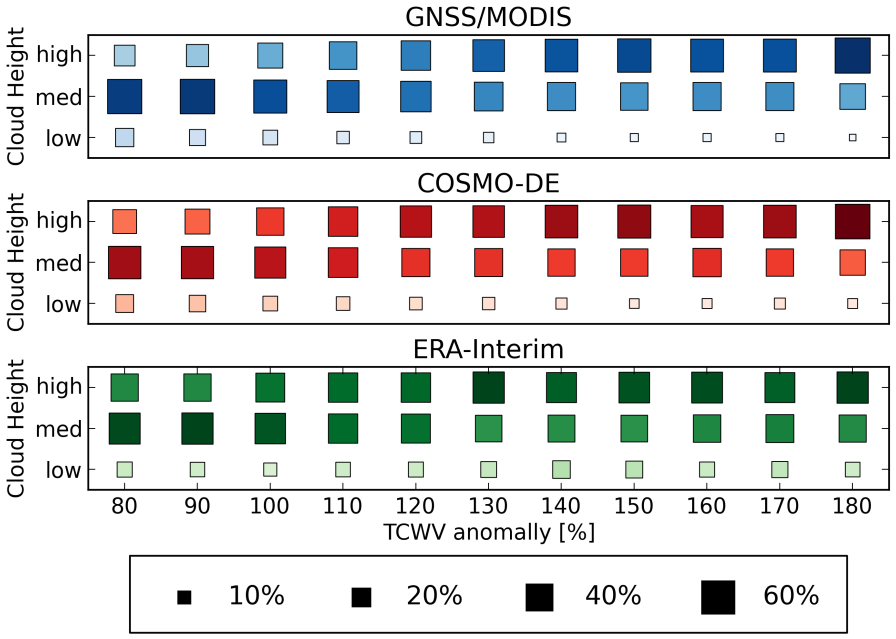

FIGURE 6.10: Frequency of cloud top heights for different TCWV anomaly intervals (indicated by the size and the darkness of the squares). See text for detailed description.

the COSMO-DE model and ERA-Interim data set were collocated. In the following the main findings of this study are listed:

1. The comparison of weekly mean TCWV reveals that COSMO-DE agrees with the observations even in short term variations of the TCWV, whereas ERA-Interim shows some deviations. The modelled TCWV shows a systematic dry bias.

2. The weekly mean TCWV for scenes, where MODIS detects mostly ice clouds is higher on average than for the cases with mostly water clouds.

3. There are systematic differences in the comparison of the weekly mean CWP. Generally, the models show lower CWP with only half of the yearly mean CWP in the COSMO-DE case in comparison to the observations. A possible explanation is the lack of sub-grid clouds in the integral of cloud water path. The observed weekly mean CWP is significantly higher in the winter months. This could be explained by the high sun zenith angles that are problematic for the retrieval.

4. The TCWV anomaly from the climatological mean is increased for cloudy cases in comparison to all cases (consistent with the findings in Chapter 5). Here, COSMO-DE overestimates the number of cases with cloud cover higher than 75 %. A detailed analysis reveals that mostly high clouds are responsible for the difference, that is consistent with evaluation studies of the Model.

5. The observations show a clear relationship of increasing seasonal mean TCWV with increasing cloud cover . In the COSMO-DE output this relationship is captured, although the TCWV for lower cloud cover s is reduced in comparison to the observation. This could be explained by the dominance of the number of cases with high cloud cover s above 80 % in the model data output. The observations show that cloud cover between 20 and 80 % are less common in this comparison. COSMO-DE overestimates the number of cases with high cloud cover. A similar behaviour applies to the ERA-Interim data set.

6. The direct comparison of TCWV anomaly, CWP and cloud cover supports the earlier findings. TCWV anomaly is increasing and cases with higher CWP are more likely with higher cloud cover in the observations. COSMO-DE only produces mean CWP higher than $140\,\mathrm{g/m^2}$ only for cloud cover higher than 80 %. The outcome of the ERA-Interim data is closer to the observation than COSMO-DE.

7. The investigation of the statistical relationship between TCWV anomaly and cloud height reveals that for low TCWV anomalies medium cloud top heights are most common. With increasing TCWV anomaly, the number of cases with higher cloud top as well as the number of low cloud cases is decreasing. Here, observations and models generally agree. However in the direct case-by-case comparison the agreement is lower.

Summarizing the relationship between TCWV and clouds for the observations, the TCWV increases not only with higher cloud cover but also with increasing CWP and cloud top height and the fraction of cloud top ice phase. The CWP and the cloud top height and phase can be a measure of the cloud thickness and type. However, in order to draw a clear conclusion of the relationship between TCWV and cloud type, observations of cloud types or at least cloud extend such as from space borne radar have to be taken into account. These studies can also serve the improvement of the parametrisation of the models.

Summarizing the relationship between TCWV and clouds of the observations in comparison to the models, there are some differences. This could originate from the spatial and temporal resolution of the models as well as the parametrisations of the cloud processes. Although the spatial resolution of COSMO-DE allows simulations of deep moist convection, it can not resolve small scale convection. The underestimation of TCWV and CWP could be a result of that. The overestimation of cloud cover , in detail of high thin clouds as stated by Böhme *et al.* (2011), could be verified in this comparison.

Overall summarizing, this study represents a first step to a detailed analysis of the interaction between cloud and TCWV and the corresponding representation/parametrisation in the models. On the one hand, the limitation of the area of interest (Germany) allows a better interpretation of the data than a study of global data, due to the similar climatological circumstances. On the other hand, the outcome of this study is constrained to only this area and can not be extrapolated to other regions. Consequently, it is planned to extend the collocation for the global GNSS data set used in Chapter 5 (Wang *et al.*

2007). In addition to the GNSS TCWV, observations from space on high spatial resolutions such as from MERIS (see Chapter 3) can be used to derive the spatial variability on a statistical level. These information can serve the improvement of the cloud evolution parametrisation in the models. The consideration of information of the weather situation or general circulation patterns is favourable.

Chapter 7

Conclusion and outlook

An universal total column water vapour retrieval has been developed and implemented that derives TCWV from space borne radiance measurements for cloud-free land and ocean surfaces. The procedure allows the adaption to satellite sensors that measure radiance in the $\rho\sigma\tau$-water vapour absorption band. The algorithm iteratively minimises the difference between simulated and measured radiances in a water vapour absorption channel with a sophisticated optimal estimation method. Additionally, it provides uncertainty estimates on a pixel basis.

For this purpose, radiative transfer simulations have been performed for the water vapour absorption band around 950 nm including the adjacent window bands. In order to fill the gap between MERIS and OLCI in the TCWV time series, the retrieval was first adapted to MODIS observations.

The investigation of a retrieval using only one of the three absorption channels of MODIS results in different biases for each channel. After an extensive search for reasons for these deviations and excluding several possible sources of errors such as the inaccurate spectral calibration, the real cause remained unclear. Consequently, correction coefficients were obtained setting ground based MWR measurements as truth and applied to the forward operator that derives the atmospheric transmittance for each absorption channel. Further, the universal retrieval was extended to ocean surfaces. Despite the fact that dark ocean surfaces lead to higher uncertainties, information about the TCWV on a pixel basis can improve atmospheric corrections, especially for ocean color remote sensing.

A detailed theoretical analysis of uncertainties of TCWV retrievals, that use radiance measurements in the NIR, has been performed, focussing on the optimal channel combination for future sensors. The study reveals that the uncertainties are most depended on the surface reflectance followed by the presence of aerosols. In order to reduce the uncertainties, in particular over dark surfaces, it is suggested to use at least two water vapour absorption bands. Additionally, the optimal positions of the absorption bands were evaluated by means of minimising the theoretical uncertainties.

Furthermore, influences of the constrains to cloud-free areas and the low temporal sampling of TCWV retrieved from polar orbiting satellites using reflected sunlight were assessed. A global data set of TCWV derived from ground based GNSS zenith total delay measurements, that is not affected by clouds, was analysed. The study reveals that analysis of global mean TCWV is only marginally influenced by the fact that most of the areas on the globe are only covered maximal once per day at 10:30 local time. However, the variability of TCWV on a particular day can be larger than the difference between the TCWV value observed from space and the daily mean TCWV. The limitation to cloud-free areas introduces a significant dry bias to monthly mean TCWV.

Although this thesis focusses on the observation of TCWV, its representativeness and the uncertainties, two applications of TCWV were presented. First, full resolution MERIS TCWV data was used to demonstrate that small scale variations of water vapour in the boundary layer can be resolved. A case study was presented demonstrating the possibility to detect convective rolls could be detected over land surfaces over Central Europe.

Secondly, the statistical relationship between TCWV and cloud properties was quantified. Ground based GNSS TCWV data over Germany has been used and collocated with space borne observations of cloud properties extracted from the MODIS L2 cloud product. The general outcome of the investigation is that on average, TCWV and total cloud water path (CWP) increase with increasing cloud coverage. Additionally, analysis data of the high resolution COSMO-DE model and reanalysis data from ERA-Interim were collocated. It turns out that on average the models agree with the observations. However, the models tend to produce more cloudy cases with lower CWP.

To conclude, a basis of future remote sensing of water vapour has been accomplished with the universal water vapour retrieval. Detailed analysis of the uncertainties and representativeness were performed that enable fair interpretations of the outcomes of studies that make use of the retrieved TCWV. A vital component of this work are ground based observations of TCWV, in particular from GNSS stations. These observations serve as ground-truth for the evaluation studies and are basis of the quantification of the statistical relationship between cloud properties and TCWV.

In the near future, there are a few issues that have to be addressed regarding the universal TCWV retrieval. Most importantly, the evaluation of the ocean processor has to be done for MODIS and continued for MERIS with appropriate and independent data. Furthermore, the reasons for the wet bias in the ocean processor need to be assessed. Additionally, a comparison between MODIS and MERIS TCWV will be performed in order to check for consistency. TCWV will be processed using the first OLCI data in order to evaluate the performance especially over water surfaces. A closer look will be taken on the uncertainties of the retrieved TCWV on a global scale will be taken. Especially over land, the influence of the surface type, e.g. to vegetation, is planned to be addressed.

Generally, TCWV will be retrieved for the entire MERIS and MODIS time series, allowing studies about global water vapour trends like Docter (2015). Further, small scale

variabilities of TCWV from MERIS full resolution data will be investigated. In particular, statistics of the small scale humidity structures will be derived. These information can potentially improve the understanding of cloud formation processes in the NWP and climate models.

The universal TCWV retrieval will be implemented in the BEAM software toolbox (open source). A broad community of remote sensing scientist will be able to retrieve TCWV for the scenes of interest. Finally, the retrieval will be adapted to OLCI data, validated and cross compared with MODIS TCWV.

Once MTG is operating, observations of TCWV on high temporal and spatial resolutions are possible. This will largely benefit studies of the diurnal cycle of TCWV. Furthermore, studies about the interaction of water vapour and clouds, in particular the prediction of convective initiation processes, will be performed with this data.

Bibliography

Albert, P., Bennartz, R., and Fischer, J. (2001). Remote Sensing of Atmospheric Water Vapor from Backscattered Sunlight in Cloudy Atmospheres. *Journal of Atmospheric and Oceanic Technology*, **18**, 865.

Albert, P., Bennartz, R., Preusker, R., Leinweber, R., and Fischer, J. (2005). Remote Sensing of Atmospheric Water Vapor Using the Moderate Resolution Imaging Spectroradiometer. *Journal of Atmospheric and Oceanic Technology*, **22**, 309.

Amato, U., Antoniadis, A., De Feis, I., Masiello, G., Matricardi, M., and Serio, C. (2009). Technical note: Functional sliced inverse regression to infer temperature, water vapour and ozone from iasi data. *Atmospheric Chemistry and Physics*, **9**(14), 5321–5330.

Antón, M., Loyola, D., Román, R., and Vömel, H. (2015). Validation of GOME-2/MetOp-a total water vapour column using reference radiosonde data from the GRUAN network. *Atmos. Meas. Tech.*, **8**(3), 1135–1145.

Baldauf, M., Seifert, A., Förstner, J., Majewski, D., Raschendorfer, M., and Reinhardt, T. (2011). Operational convective-scale numerical weather prediction with the COSMO model: Description and sensitivities. *Mon. Wea. Rev.*, **139**(12), 3887–3905.

Bandeen, W. R., Hanel, R. A., Licht, J., Stampfl, R. A., and Stroud, W. G. (1961). Infrared and reflected solar radiation measurements from the tiros II meteorological satellite. *J. Geophys. Res.*, **66**(10), 3169–3185.

Bartsch, B., Bakan, S., and Fischer, J. (1996). Passive remote sensing of the atmospheric water vapour content above land surfaces. *Advances in Space Research*, **18**, 25–28.

Bennartz, R. and Fischer, J. (2000). A modified k-distribution approach applied to narrow band water vapour and oxygen absorption estimates in the near infrared. *Journal of Quantitative Spectroscopy & Radiative Transfer*, **66**, 539–553.

Bennartz, R. and Fischer, J. (2001). Retrieval of columnar water vapour over land from backscattered solar radiation using the medium resolution imaging spectrometer. *Remote Sensing of Environment*, **78**(3), 274 – 283.

Bevis, M., Businger, S., Herring, T. A., Rocken, C., Anthes, R. A., and Ware, R. H. (1992). GPS meteorology: Remote sensing of atmospheric water vapor using the global positioning system. *J. Geophys. Res.*, **97**(D14), 15787.

Boesch, H., Deutscher, N. M., Warneke, T., Byckling, K., Cogan, A. J., Griffith, D. W. T., Notholt, J., Parker, R. J., and Wang, Z. (2013). HDO/h2o ratio retrievals from GOSAT. *Atmos. Meas. Tech.*, **6**(3), 599–612.

Böhme, T., Stapelberg, S., Akkermans, T., Crewell, S., Fischer, J., Reinhardt, T., Seifert, A., Selbach, C., and Lipzig, N. V. (2011). Long-term evaluation of COSMO forecasting using combined observational data of the GOP period. *Meteorologische Zeitschrift*, **20**(2), 119–132.

Bourg, L., D'Alba, L., and Colagrande, P. (2008). Meris smile effect characterisation and correction. Technical note, European Space Agency, Paris.

Bruegge, C. J., Conel, J. E., Green, R. O., Margolis, J. S., Holm, R. G., and Toon, G. (1992). Water vapor column abundance retrievals during FIFE. *Journal of Geophysic Research*, **97**, 18759.

Cadeddu, M. P., Liljegren, J. C., and Turner, D. D. (2013). The atmospheric radiation measurement (ARM) program network of microwave radiometers: instrumentation, data, and retrievals. *Atmos. Meas. Tech.*, **6**(9), 2359–2372.

Carbajal Henken, C. K., Diedrich, H., Preusker, R., and Fischer, J. (2015). MERIS full-resolution total column water vapor: observing horizontal convective rolls. *Geophys. Res. Lett.*

Carrer, D., Roujean, J.-L., and Meurey, C. (2010). Comparing operational MSG/SEVIRI land surface albedo products from land SAF with ground measurements and MODIS. *IEEE Trans. Geosci. Remote Sensing*, **48**(4), 1714–1728.

Casadio, S., Castelli, E., Papandrea, E., Dinelli, B., Pisacane, G., Burini, A., and Bojkov, B. (2016). Total column water vapour from along track scanning radiometer series using thermal infrared dual view ocean cloud free measurements: The advanced infrared WAter vapour estimator (AIRWAVE) algorithm. *Remote Sensing of Environment*, **172**, 1–14.

Clough, S. A., Shephard, M. W., Mlawer, E. J., Delamere, J. S., Iacono, M. J., Cady-Pereira, K., Boukabara, S., and Brown, P. D. (2005). Atmospheric radiative transfer modeling: a summary of the AER codes. *Journal of Quantitative Spectroscopy & Radiative Transfer*, **91**, 233–244.

Cox, C. and Munk, W. (1954). Measurement of the roughness of the sea surface from photographs of the sun's glitter. *Journal of the Optical Society of America (1917-1983)*, **44**, 838.

Dee, D. P., Uppala, S. M., Simmons, A. J., Berrisford, P., Poli, P., Kobayashi, S., Andrae, U., Balmaseda, M. A., Balsamo, G., Bauer, P., Bechtold, P., Beljaars, A. C. M., Bergvan de , L., Bidlot, J., Bormann, N., Delsol, C., Dragani, R., Fuentes, M., Geer, A. J., Haimberger, L., Healy, S. B., Hersbach, H., Hólm, E. V., Isaksen, L., Kållberg, P., Köhler, M., Matricardi, M., McNally, A. P., Monge-Sanz, B. M., Morcrette, J.-J., Park, B.-K., Peubey, C., Rosnayde , P., Tavolato, C., Thépaut, J.-N.,

and Vitart, F. (2011). The ERA-interim reanalysis: configuration and performance of the data assimilation system. *Quarterly Journal of the Royal Meteorological Society*, **137**(656), 553–597.

Delwart, S., Preusker, R., Bourg, L., Santer, R., Ramon, D., and Fischer, J. (2007). MERIS in-flight spectral calibration. *International Journal of Remote Sensing*, **28**, 479–496.

Dick, G., Gendt, G., and Reigber, C. (2001). First experience with near real-time water vapor estimation in a German GPS network. *Journal of Atmospheric and Solar-Terrestrial Physics*, **63**, 1295–1304.

Diedrich, H., Preusker, R., Lindstrot, R., and Fischer, J. (2013). Quantification of uncertainties of water vapour column retrievals using future instruments. *Atmospheric Measurement Techniques*, **6**, 359–370.

Diedrich, H., Preusker, R., Lindstrot, R., and Fischer, J. (2015). Retrieval of daytime total columnar water vapour from modis measurements over land surfaces. *Atmospheric Measurement Techniques*, **8**(2), 823–836.

Dirksen, R. J., Sommer, M., Immler, F. J., Hurst, D. F., Kivi, R., and Vömel, H. (2014). Reference quality upper-air measurements: GRUAN data processing for the vaisala RS92 radiosonde. *Atmos. Meas. Tech.*, **7**(12), 4463–4490.

Docter, N. (2015). *Spatially high resolution trend analysis of TCWV over land surfaces using MERIS*. Master's thesis, Freie Universität Berlin.

Doppler, L., Carbajal-Henken, C., Pelon, J., Ravetta, F., and Fischer, J. (2014a). Extension of radiative transfer code MOMO, matrix-operator model to the thermal infrared - Clear air validation by comparison to RTTOV and application to CALIPSO-IIR. *Journal of Quantitative Spectroscopy and Radiative Transfer*, **144**, 49–67.

Doppler, L., Preusker, R., Bennartz, R., and Fischer, J. (2014b). k-bin and k-IR: k-distribution methods without correlation approximation for non-fixed instrument response function and extension to the thermal infrared / Applications to satellite remote sensing. *Journal of Quantitative Spectroscopy and Radiative Transfer*, **133**, 382–395.

Durack, P. (2015). Ocean salinity and the global water cycle. *Oceanography*, **28**(1), 20–31.

Durre, I., Vose, R. S., and Wuertz, D. B. (2006). Overview of the Integrated Global Radiosonde Archive. *Journal of Climate*, **19**, 53–68.

Eikenberg, S., Köhler, C., Seifert, A., and Crewell, S. (2015). How microphysical choices affect simulated infrared brightness temperatures. *Atmospheric Research*, **156**, 67–79.

Fell, F. and Fischer, J. (2001). Numerical simulation of the light field in the atmosphere-ocean system using the matrix-operator method. *Journal of Quantitative Spectroscopy & Radiative Transfer*, **69**, 351–388.

Fischer, J. and Grassl, H. (1984). Radiative transfer in an atmosphere-ocean system: an azimuthally dependent matrix-operator approach. *Applied Optics*, **23**, 1032–1039.

Frankenberg, C., Yoshimura, K., Warneke, T., Aben, I., Butz, A., Deutscher, N., Griffith, D., Hase, F., Notholt, J., Schneider, M., Schrijver, H., and Rockmann, T. (2009). Dynamic processes governing lower-tropospheric HDO/h2o ratios as observed from space and ground. *Science*, **325**(5946), 1374–1377.

Gaffen, D. J. and Elliott, W. P. (1993). Column Water Vapor Content in Clear and Cloudy Skies. *Journal of Climate*, **6**, 2278–2287.

Gao, B.-C. and Kaufman, Y. J. (2003). Water vapor retrievals using Moderate Resolution Imaging Spectroradiometer (MODIS) near-infrared channels. *Journal of Geophysical Research (Atmospheres)*, **108**, 4389.

Gao, B.-C., Goetz, A. F. H., Westwater, E. R., Conel, J. E., and Green, R. O. (1993). Possible Near-IR Channels for Remote Sensing Precipitable Water Vapor from Geostationary Satellite Platforms. *Journal of Applied Meteorology*, **32**, 1791–1801.

GCOS (2010). World meteorological organization: Guideline for the generation of datasets and products meeting gcos requirements (gcos-143).

Gendt, G., Dick, G., Reigber, C., Tomassini, M., Liu, Y., and Ramatschi, M. (2004). Near real time gps water vapor monitoring for numerical weather prediction in germany. *Journal of the Meteorological Society of Japan. Ser. II*, **82**(1B), 361–370.

Grant, I. P. and Hunt, G. E. (1969). Discrete Space Theory of Radiative Transfer. I. Fundamentals. *Royal Society of London Proceedings Series A*, **313**, 183–197.

Grossi, M., Valks, P., Loyola, D., Aberle, B., Slijkhuis, S., Wagner, T., Beirle, S., and Lang, R. (2015). Total column water vapour measurements from GOME-2 MetOp-a and MetOp-b. *Atmos. Meas. Tech.*, **8**(3), 1111–1133.

GTOPO (1996). Us geological survey: Global 30 arc-second elevation data set.

Held, I. and Soden, B. (2000). Water vapor feedback and global warming. *ANNUAL REVIEW OF ENERGY AND THE ENVIRONMENT*, **25**, 441–475.

Held, I. M. and Soden, B. J. (2006). Robust Responses of the Hydrological Cycle to Global Warming. *Journal of Climate*, **19**, 5686.

Henken, C. K. C., Lindstrot, R., Preusker, R., and Fischer, J. (2014). FAME-c: cloud property retrieval using synergistic AATSR and MERIS observations. *Atmos. Meas. Tech.*, **7**(11), 3873–3890.

Hess, M., Koepke, P., and Schult, I. (1998). Optical Properties of Aerosols and Clouds: The Software Package OPAC. *Bulletin of the American Meteorological Society*, **79**, 831–844.

Hollstein, A. and Fischer, J. (2012). Effects of salinity, temperature, and polarization on top of atmosphere and water leaving radiances for case 1 waters. *Appl. Opt.*, **51**(33), 8022.

Illingworth, A. J., Hogan, R. J., O'Connor, E. J., Bouniol, D., Delanoë, J., Pelon, J., Protat, A., Brooks, M. E., Gaussiat, N., Wilson, D. R., Donovan, D. P., Baltink, H. K., Zadelhoffvan , G.-J., Eastment, J. D., Goddard, J. W. F., Wrench, C. L., Haeffelin, M., Krasnov, O. A., Russchenberg, H. W. J., Piriou, J.-M., Vinit, F., Seifert, A., Tompkins, A. M., and Willén, U. (2007). Cloudnet. *Bull. Amer. Meteor. Soc.*, **88**(6), 883–898.

Immler, F. J., Dykema, J., Gardiner, T., Whiteman, D. N., Thorne, P. W., and Vömel, H. (2010). Reference quality upper-air measurements: guidance for developing GRUAN data products. *Atmos. Meas. Tech.*, **3**(5), 1217–1231.

IPCC (2007). IPCC (2007): Climate Change The Physical Science Basis. *AGU Fall Meeting Abstracts*, **1**, D1+.

IPCC (2014). Climate change 2014: Synthesis report. contribution of working groups i, ii and iii to the fifth assessment report of the intergovernmental panel on climate change. *IPCC, Geneva, Switzerland*, page 151 pp.

Jin, S., Park, J.-U., Cho, J.-H., and Park, P.-H. (2007). Seasonal variability of GPS-derived zenith tropospheric delay (1994-2006) and climate implications. *J. Geophys. Res.*, **112**(D9).

Kiehl, J. T. and Trenberth, K. E. (1997). Earth's Annual Global Mean Energy Budget. *Bulletin of the American Meteorological Society*, **78**, 197–197.

Koepke, P. (1985). The reflectance factors of a rough ocean with foam - comment on 'Remote sensing of the sea state using the 0.8-1.1 mu m spectral band' by L. Wald and J. M. Monget. *International Journal of Remote Sensing*, **6**, 787–797.

Li, G., Kimura, F., Sato, T., and Huang, D. (2007). A composite analysis of diurnal cycle of GPS precipitable water vapor in central japan during calm summer days. *Theoretical and Applied Climatology*, **92**(1-2), 15–29.

Lindstrot, R. and Preusker, R. (2012). On the efficient treatment of temperature profiles for the estimation of atmospheric transmittance under scattering conditions. *Atmospheric Measurement Techniques*, **5**, 2525–2535.

Lindstrot, R., Preusker, R., Diedrich, H., Doppler, L., Bennartz, R., and Fischer, J. (2012). 1D-Var retrieval of daytime total columnar water vapour from MERIS measurements. *Atmospheric Measurement Techniques*, **5**, 631–646.

Lindstrot, R., Stengel, M., Schröder, M., Fischer, J., Preusker, R., Schneider, N., Steenbergen, T., and Bojkov, B. R. (2014). A global climatology of total columnar water vapour from ssm/i and meris. *Earth System Science Data*, **6**(1), 221–233.

Liou, K. (2002). *An Introduction to Atmospheric Radiation, Second Edition*, volume 84 of *International Geophysic Series*. Academic Press, 2nd edition.

Loeb, N. G., Wielicki, B. A., Doelling, D. R., Smith, G. L., Keyes, D. F., Kato, S., Manalo-Smith, N., and Wong, T. (2009). Toward optimal closure of the earth's top-of-atmosphere radiation budget. *Journal of Climate*, **22**(3), 748–766.

Masiello, G., Serio, C., Deleporte, T., Herbin, H., Behrendt, A., Bosser, P., Bock, O., Wulfmeyer, V., Pommier, M., and Flamant, C. (2013). Comparison of iasi water vapour products over complex terrain with cops campaign data. *Meteorologische Zeitschrift*, **22**(4), 471–487.

McClatchey, R., Fenn, R., Selby, J., Volz, F., and Garing, J. (1972). Optical properties of the atmosphere (3rd ed.). Technical report, Air Force Cambridge Research Laboratories.

Mie, G. (1908). Beiträge zur Optik trüber Medien, speziell kolloidaler Metallösungen. *Annalen der Physik*, **330**, 377–445.

Mieruch, S., Noël, S., Bovensmann, H., and Burrows, J. P. (2008). Analysis of global water vapour trends from satellite measurements in the visible spectral range. *Atmospheric Chemistry and Physics*, **8**(3), 491–504.

Ning, T., Wang, J., Elgered, G., Dick, G., Wickert, J., Bradke, M., and Sommer, M. (2015). The uncertainty of the atmospheric integrated water vapour estimated from GNSS observations. *Atmos. Meas. Tech. Discuss.*, **8**(8), 8817–8857.

Noël, S., Buchwitz, M., Bovensmann, H., and Burrows, J. P. (2002). Retrieval of total water vapour column amounts from GOME/ERS-2 data. *Advances in Space Research*, **29**, 1697–1702.

Ortiz de Galisteo, J. P., Cachorro, V., Toledano, C., Torres, B., Laulainen, N., Bennouna, Y., and de Frutos, A. (2011). Diurnal cycle of precipitable water vapor over Spain. *Quarterly Journal of the Royal Meteorological Society*, **137**, 948–958.

Pérez-Ramírez, D., Whiteman, D. N., Smirnov, A., Lyamani, H., Holben, B. N., Pinker, R., Andrade, M., and Alados-Arboledas, L. (2014). Evaluation of AERONET precipitable water vapor versus microwave radiometry, GPS, and radiosondes at ARM sites. *Journal of Geophysical Research (Atmospheres)*, **119**, 9596–9613.

Petty, G. W. (2006). *A first Course in Atmospheric Radiation*. Sundog Publishing, Madison, Wisconsin, 2nd edition.

Plass, G. N., Kattawar, G. W., and Catchings, F. E. (1973). Matrix operator theory of radiative transfer. 1: Rayleigh scattering. *Applied Optics*, **12**, 314–329.

Platnick, S., Ackerman, S., and King, M. (2015). Modis atmosphere l2 cloud product (06 l2). *NASA MODIS Adaptive Processing System Goddard Space Flight Center USA*.

Pougatchev, N., August, T., Calbet, X., Hultberg, T., Oduleye, O., Schlüssel, P., Stiller, B., St. Germain, K., and Bingham, G. (2009). IASI temperature and water vapor retrievals - error assessment and validation. *Atmospheric Chemistry & Physics*, **9**, 6453–6458.

Pralungo, L. R., Haimberger, L., and Stickler, A. (2014). A global radiosonde and tracked balloon archive on 16 pressure levels (GRASP) back to 1905 part 1: Merging and interpolation to 00:00 and 12:00 GMT. *Earth Syst. Sci. Data*, **6**(1), 185–200.

Ptashnik, I. V., McPheat, R. A., Shine, K. P., Smith, K. M., and Williams, R. G. (2011). Water vapor self-continuum absorption in near-infrared windows derived from laboratory measurements. *J. Geophys. Res.*, **116**(D16).

Quaas, J. (2012). Evaluating the critical relative humidity as a measure of subgrid-scale variability of humidity in general circulation model cloud cover parameterizations using satellite data. *J. Geophys. Res.*, **117**(D9).

Radhakrishna, B., Fabry, F., Braun, J. J., and Hove, T. V. (2015). Precipitable water from GPS over the continental united states: Diurnal cycle, intercomparisons with NARR, and link with convective initiation. *Journal of Climate*, **28**(7), 2584–2599.

Ramanathan, V., Barkstrom, B. R., and Harrison, E. F. (1989). Climate and the earth's radiation budget. *Physics Today*, **42**, 22–33.

Randel, W. J., Moyer, E., Park, M., Jensen, E., Bernath, P., Walker, K., and Boone, C. (2012). Global variations of hdo and hdo/h2o ratios in the upper troposphere and lower stratosphere derived from ace-fts satellite measurements. *J. Geophys. Res.*, **117**(D6).

Rast, M., Bezy, J. L., and Bruzzi, S. (1999). The ESA medium resolution imaging spectrometer MERIS a review of the instrument and its mission. *International Journal of Remote Sensing*, **20**(9), 1681–1702.

Rayleigh, L. (1928). The Light of the Night Sky: Its Intensity Variations when Analysed by Colour Filter. III. *Royal Society of London Proceedings Series A*, **119**, 11–33.

Reagan, J. A., Herman, B. M., Palmer, J. M., and Thomason, L. W. (1986). Assessment of atmospheric limitations on the determination of the solar spectral constant from ground-based spectroradiometer measurements. *IEEE Transactions on Geoscience and Remote Sensing*, **24**, 258–266.

Risi, C., Noone, D., Worden, J., Frankenberg, C., Stiller, G., Kiefer, M., Funke, B., Walker, K., Bernath, P., Schneider, M., Bony, S., Lee, J., Brown, D., and Sturm, C. (2012). Process-evaluation of tropospheric humidity simulated by general circulation models using water vapor isotopic observations: 2. using isotopic diagnostics to understand the mid and upper tropospheric moist bias in the tropics and subtropics. *J. Geophys. Res.*, **117**(D5).

Rodgers, C. (2000). *Inverse Methods for Atmospheric Sounding: Theory and Practice*. World Scientific Pub Co.

Rosenkranz, P. W. (2001). Retrieval of temperature and moisture profiles from AMSU-A and AMSU-B measurements. *IEEE Transactions on Geoscience and Remote Sensing*, **39**, 2429–2435.

Rothman, L., Gordon, I., Babikov, Y., Barbe, A., Benner, D. C., Bernath, P., Birk, M., Bizzocchi, L., Boudon, V., Brown, L., Campargue, A., Chance, K., Cohen, E., Coudert, L., Devi, V., Drouin, B., Fayt, A., Flaud, J.-M., Gamache, R., Harrison, J., Hartmann, J.-M., Hill, C., Hodges, J., Jacquemart, D., Jolly, A., Lamouroux, J., Roy, R. L., Li, G., Long, D., Lyulin, O., Mackie, C., Massie, S., Mikhailenko, S., Müller, H., Naumenko, O., Nikitin, A., Orphal, J., Perevalov, V., Perrin, A., Polovtseva, E., Richard, C., Smith, M., Starikova, E., Sung, K., Tashkun, S., Tennyson, J., Toon, G., Tyuterev, V., and Wagner, G. (2013). The HITRAN2012 molecular spectroscopic database. *Journal of Quantitative Spectroscopy and Radiative Transfer*, **130**, 4–50.

Rothman, L. S., Rinsland, C. P., Goldman, A., Massie, S. T., Edwards, D. P., Flaud, J.-M., Perrin, A., Camy-Peyret, C., Dana, V., Mandin, J.-Y., Schroeder, J., McCann, A., Gamache, R. R., Wattson, R. B., Yoshino, K., Chance, K., Jucks, K., Brown, L. R., Nemtchinov, V., and Varanasi, P. (2010). Reprint of: The HITRAN molecular spectroscopic database and HAWKS (HITRAN Atmospheric Workstation): 1996 edition. *Journal of Quantitative Spectroscopy & Radiative Transfer*, **111**, 1568–1613.

Schluessel, P. and Emery, W. J. (1990). Atmospheric water vapour over oceans from SSM/I measurements. *International Journal of Remote Sensing*, **11**, 753–766.

Schrijver, H., Gloudemans, A. M. S., Frankenberg, C., and Aben, I. (2009). Water vapour total columns from sciamachy spectra in the 2.36 micron window. *Atmospheric Measurement Techniques*, **2**(2), 561–571.

Schroedterhomscheidt, Drews, A., and Heise, S. (2008). Total water vapor column retrieval from MSG-SEVIRI split window measurements exploiting the daily cycle of land surface temperatures. *Remote Sensing of Environment*, **112**(1), 249–258.

Seidel, D. J., Berger, F. H., Immler, F., Sommer, M., Vömel, H., Diamond, H. J., Dykema, J., Goodrich, D., Murray, W., Peterson, T., Sisterson, D., Thorne, P., and Wang, J. (2009). Reference upper-air observations for climate: Rationale, progress, and plans. *Bull. Amer. Meteor. Soc.*, **90**(3), 361–369.

Seidel, D. J., Sun, B., Pettey, M., and Reale, A. (2011). Global radiosonde balloon drift statistics. *J. Geophys. Res.*, **116**(D7).

Shannon, C. (1948). A mathematical theory of communication. *The Bell System Technical Journal*, **27**, 379–423, 623–656.

Sherwood, S. C., Roca, R., Weckwerth, T. M., and Andronova, N. G. (2010). Tropospheric water vapor, convection, and climate. *Rev. Geophys.*, **48**(2).

Shi, L. and Bates, J. J. (2011). Three decades of intersatellite-calibrated high-resolution infrared radiation sounder upper tropospheric water vapor. *J. Geophys. Res.*, **116**(D4).

Shine, K. P., Ptashnik, I. V., and Rädel, G. (2012). The water vapour continuum: Brief history and recent developments. *Surv Geophys*, **33**(3-4), 535–555.

Soden, B. J. (2002). Global cooling after the eruption of mount pinatubo: A test of climate feedback by water vapor. *Science*, **296**(5568), 727–730.

Stephens, G. L., Li, J., Wild, M., Clayson, C. A., Loeb, N., Kato, S., L'Ecuyer, T., Stackhouse, P. W., Lebsock, M., and Andrews, T. (2012). An update on earth's energy balance in light of the latest global observations. *Nature Geoscience*, **5**(10), 691–696.

Stubenrauch, C. J., Rossow, W. B., Kinne, S., Ackerman, S., Cesana, G., Chepfer, H., Girolamo, L. D., Getzewich, B., Guignard, A., Heidinger, A., Maddux, B. C., Menzel, W. P., Minnis, P., Pearl, C., Platnick, S., Poulsen, C., Riedi, J., Sun-Mack, S., Walther, A., Winker, D., Zeng, S., and Zhao, G. (2013). Assessment of global cloud datasets from satellites: Project and database initiated by the GEWEX radiation panel. *Bull. Amer. Meteor. Soc.*, **94**(7), 1031–1049.

Susskind, J., Barnet, C., and Blaisdell, J. (2003). Retrieval of atmospheric and surface parameters from AIRS/AMSU/HSB data in the presence of clouds. *IEEE TRANSACTIONS ON GEOSCIENCE AND REMOTE SENSING*, **41**(2), 390–409.

Trenberth, K. E. (1999). Atmospheric moisture recycling: Role of advection and local evaporation. *Journal of Climate*, **12**, 1368–1381.

Trenberth, K. E., Fasullo, J., and Smith, L. (2005). Trends and variability in column-integrated atmospheric water vapor. *Climate Dynamics*, **24**, 741–758.

Trenberth, K. E., Fasullo, J. T., and Kiehl, J. (2009). Earth's Global Energy Budget. *Bulletin of the American Meteorological Society*, **90**, 311–+.

Turner, D. D., Lesht, B. M., Clough, S. A., Liljegren, J. C., Revercomb, H. E., and Tobin, D. C. (2003). Dry Bias and Variability in Vaisala RS80-H Radiosondes: The ARM Experience. *Journal of Atmospheric and Oceanic Technology*, **20**, 117–132.

Turner, D. D., Clough, S. A., Liljegren, J. C., Clothiaux, E. E., Cady-Pereira, K. E., and Gaustad, K. L. (2007). Retrieving Liquid Water Path and Precipitable Water Vapor From the Atmospheric Radiation Measurement (ARM) Microwave Radiometers. *IEEE Transactions on Geoscience and Remote Sensing*, **45**, 3680–3690.

Twomey, S., Jacobowitz, H., and Howell, H. B. (1966). Matrix Methods for Multiple-Scattering Problems. *Journal of Atmospheric Sciences*, **23**, 289–298.

Wagner, T., Beirle, S., Grzegorski, M., and Platt, U. (2006). Global trends (1996-2003) of total column precipitable water observed by Global Ozone Monitoring Experiment (GOME) on ERS-2 and their relation to near-surface temperature. *Journal of Geophysical Research (Atmospheres)*, **111**(10), 12102.

Wang, J., Zhang, L., Dai, A., van Hove, T., and van Baelen, J. (2007). A near-global, 2-hourly data set of atmospheric precipitable water from ground-based GPS measurements. *Journal of Geophysical Research (Atmospheres)*, **112**(D11), 11107.

Weckwerth, T. M. (2000). The Effect of Small-Scale Moisture Variability on Thunderstorm Initiation. *Monthly Weather Review*, **128**, 4017.

Weckwerth, T. M., Wilson, J. W., Wakimoto, R. M., and Crook, N. A. (1997). Horizontal Convective Rolls: Determining the Environmental Conditions Supporting their Existence and Characteristics. *Monthly Weather Review*, **125**, 505.

Wentz, F. J., Ricciardulli, L., Hilburn, K., and Mears, C. (2007). How much more rain will global warming bring? *SCIENCE*, **317**(5835), 233–235.

Wiegele, A., Schneider, M., Hase, F., Barthlott, S., García, O. E., Sepúlveda, E., González, Y., Blumenstock, T., Raffalski, U., Gisi, M., and Kohlhepp, R. (2014). The MUSICA MetOp/IASI H_2O and δD products: characterisation and long-term comparison to NDACC/FTIR data. *Atmospheric Measurement Techniques Discussions*, **7**, 3915–3952.

Wiscombe, W. J. (1980). Improved Mie scattering algorithms. *Applied Optics*, **19**, 1505–1509.

Xie, Y., Xiong, X., Qu, J. J., and Che, N. (2006). Uncertainty analysis of Terra MODIS on-orbit spectral characterization. In *Society of Photo-Optical Instrumentation Engineers (SPIE) Conference Series*, volume 6296 of *Society of Photo-Optical Instrumentation Engineers (SPIE) Conference Series*.

Xiong, X. X. and Barnes, W. (2006). An overview of MODIS radiometric calibration and characterization. *Advances in Atmospheric Sciences*, **23**, 69–79.

Young, G. S., Kristovich, D. A. R., Hjelmfelt, M. R., and Foster, R. C. (2002). Supplement to rolls, streets, waves, and more. *Bull. Amer. Meteor. Soc.*, **83**(7), 1001–1001.

Appendix

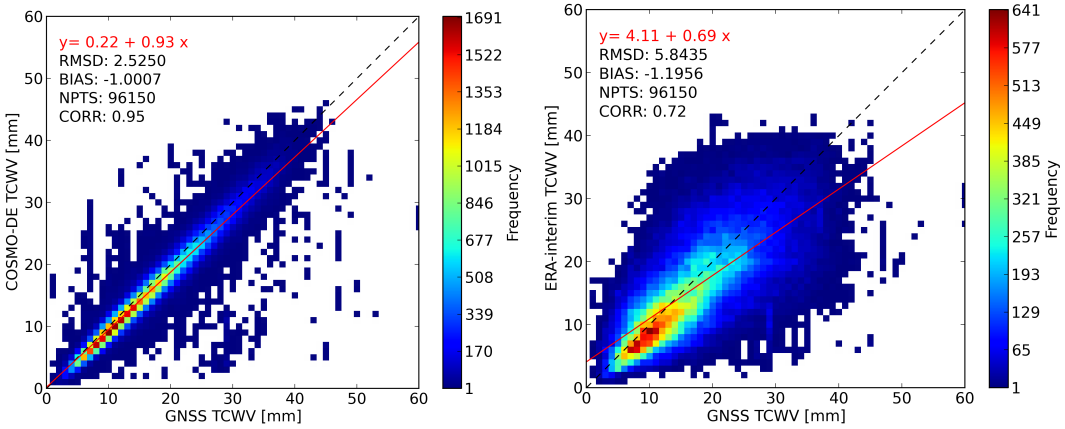

FIGURE 1: Normalized frequencies of occurrence for comparisons between TCWV from GNSS observations and models (left: COSMO-DE, right: ERA-Interim).

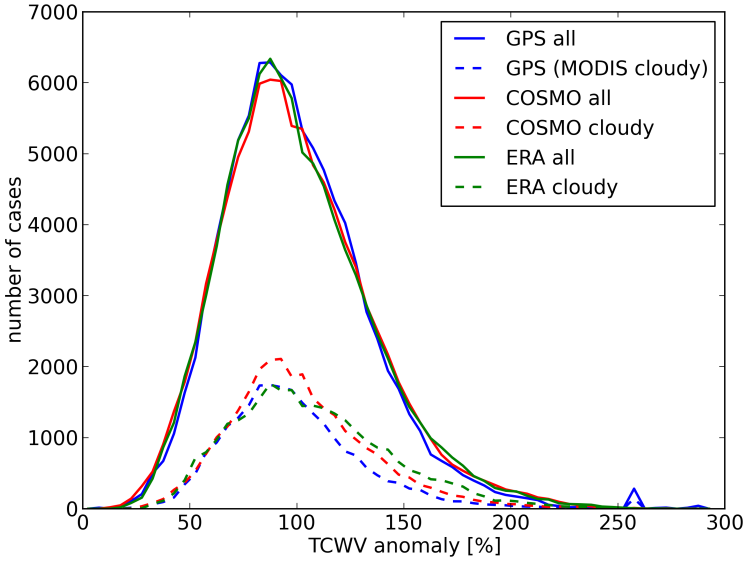

FIGURE 2: Histogram of the TCWV anomalies in % for all cases (solid lines) and for cases with cloud higher than 75 % (dashed lines). For the cloudy cases, all cases with high clouds are omitted (cloud cover of high clouds higher than 5 %).

Abbreviations

AATSR	**A**long **T**rack **S**canning **R**adiometer
AERONET	**AERO**sol Robotic **NET**work
AMF	**A**ir **M**ass **F**actor
AOT	**A**erosol **O**ptical **T**hickness
BRDF	**B**idirectional **R**eflection **D**istribution **F**unction
CERES	**E**arth's **R**adiant **E**nergy **S**ystem
CWP	**C**loud **W**ater **P**ath
DSD	**D**aily **S**tandard **D**eviation
EMiR	**E**RS/Envisat **M**WR **R**ecalibration and Water Vapour Thematic Data Record Generation
FCI	**F**lexible **C**ombined **I**mager
GCM	**G**lobal **C**irculation **M**odel
GCOS	**G**lobal **C**limate **O**bserving **S**ystem
GRUAN	**G**COS **U**pper **A**ir **R**eference **N**etwork
GNSS	**G**lobale **N**avigation **S**atellite **S**ystem
HCR	**H**orizontal **C**onvective **R**oll
LT	**L**ocal **T**ime
LUT	**L**ook **U**p **T**able
IASI	**I**nfrared **A**tmospheric **S**ounding **I**nterferometer
IQR	**I**nner**Q**uartil **R**ange
IR	**I**nfra**R**ed
NIR	**N**ear **I**nfra**R**ed
NWP	**N**umerical **W**eather **P**rediction
NSA	**N**orth **S**lope of **A**laska
MERIS	**ME**dium **R**esolution **I**imaging **S**pectrometer

MSG	**M**eteosat **S**econd **G**eneration
MTG	**M**eteosat **T**hird **G**eneration
MWR	**M**icro**W**ave **R**adiometers
MODIS	**MO**derate **R**esolution **I**imaging **S**pectroradiometer
MOMO	**M**atrix **O**perator **M**ethod **M**odel
NASA	**N**ational **A**eronautics and **S**pace **A**dministration
OLCI	**O**cean and **L**and **C**olor **I**nstrument
OE	**O**ptimal **E**stimation
PDF	**P**robability **D**ensity **F**unction
RMSD	**R**oot **M**ean **S**quare **D**eviation
rH	**r**elative **H**umidity
NPTS	**N**umber of **P**oin**TS**
SEVIRI	**S**pinning **E**nhanced **V**isible and **I**nf**R**ared **I**mager
SH	**S**pecific **H**umidity
SGP	**S**outhern **G**reat **P**lanes
SNR	**S**ignal to **N**oise **R**atio
SSM/I	**S**pecial **S**ensor **M**icrowave/**I**mager
TCWV	**T**otal **C**olumn **W**ater **V**apour
TOA	**T**op **O**f **A**tmosphere
TWP	**T**ropical **W**est **P**acific
UTC	**C**oordinated **U**niversal **T**ime
UTH	**U**pper **T**roposperic **H**umidity
VIS	**VIS**able
VCLW	**V**oigt **C**enter **L**orentz **W**ings
ZTD	**Z**enith **T**otal **D**elay

Summary

Water Vapour plays a vital role in the Earth's atmosphere. It is an important part of the water cycle and accounts for the largest component of the total greenhouse effect. Several feed-back mechanisms are connected to water vapour, in terms of the rise in global mean temperature as part of the global climate change. Observations of water vapour are crucial for the monitoring of the Earth's climate. The diversity of ground based and space borne observations has increased over the years. However, global coverage can only be provided by space borne sensors. Currently, the monitoring of water vapour on spatial resolutions up to a few hundred meters can only be provided by spectrometers that measure reflected sunlight.

In this work, a universal Total Column Water Vapour (TCVW) retrieval has been developed and implemented that derives TCWV from radiance measurements in the ρστ-water vapour absorption band. TCWV and uncertainties are provided on a pixel basis over land and ocean surfaces for all cloud-free daytime scenes. The procedure allows the adaption to satellite sensors that measure radiance in the near-infrared. The algorithm iteratively minimises the difference between simulated and measured radiances in the water vapour absorption channels with a sophisticated optimal estimation method. The procedure has been applied to the channel setups of the MEdium Resolution Imaging Spectrometer (MERIS) on ENVISAT and the MOderate Resolution Imaging Spectroradiometer (MODIS) on Aqua and Terra. It is also ready to be adapted to the Ocean and Land Color Instrument (OLCI) on Sentinel-3.

In order to assess the performance of the algorithm over land, processed TCWV data were compared to several independent ground based observations such as from Global Navigation Satellite System (GNSS) stations and GCOS Reference Upper Air Network

(GRUAN) radiosondes. The validation reveals high correlations and no significant biases. A first evaluation of the MERIS ocean processor shows a significant but constant wet bias.

The retrieval has been applied to full resolution MERIS data. It showed that small scale variations of water vapour in the boundary layer can be resolved. A case study was presented demonstrating the possibility to detect horizontal convective rolls over land surfaces over Central Europe.

Furthermore, a quantification of uncertainties of TCWV retrievals that use radiance measurements in the NIR was performed. This study includes the theoretical determination of the optimal channel combination in order to minimise the uncertainties of the retrieval.

Additionally, influences of the constrains to cloud-free areas and the low temporal sampling of TCWV retrieved from polar orbiting satellites using reflected sunlight were assessed. A global TCWV data set from ground based GNSS stations, that is not affected by clouds, was analysed. The study reveals that analysis of global mean TCWV is only marginally influenced by the fact that most of the areas on the globe are covered maximal once per day. However, the variability of TCWV on a particular day can be larger than the difference between the TCWV value observed from space and the daily mean TCWV. The limitation to cloud-free areas introduces a significant dry bias to monthly mean TCWV.

Finally, the statistical relationship between TCWV and cloud properties has been quantified. Ground based GNSS TCWV data over Germany was used and collocated with space borne observations of cloud properties extracted from the MODIS L2 product. The general outcome of the investigation is that on average, TCWV and total cloud water path (CWP) increase with increasing cloud coverage. Additionally, analysis data of the high resolution COSMO-DE model and reanalysis data from ERA-Interim were collocated. It turns out that on average the models agree with the observations. However, the models tend to produce more cloudy cases with lower CWP.

Zusammenfassung

Wasserdampf spielt eine wichtige Rolle in der Erdatmosphäre. Es ist ein bedeutender Bestandteil des Wasserkreislaufs und ist verantwortlich für den größten Teil am Treibhauseffekt. Mehrere Rückkopplungsmechanismen sind mit dem Wasserdampf verbunden, welche durch die Erhöhung der mittleren globalen Temperatur als Teil der Klimaveränderung hervorgerufen werden. Die Beobachtung von Wasserdampf ist essentiell für die Überwachung des Klimas der Erde. Die Vielfalt an Observationen vom Boden und aus dem Weltraum hat über die Jahre zugenommen. Allerdings können nur weltraumgestützte Sensoren die globale Abdeckung zur Verfügung stellen. Im Moment können nur Spektrometer, die reflektiertes Sonnenlicht messen, räumliche Auflösungen von bis zu wenigen hundert Metern erreichen.

In dieser Arbeit wurde ein Verfahren zum Ableiten des Gesamtsäulenwasserdampfes (TCWV) entwickelt und implementiert, welches TCWV aus Radianzmessungen in der $\rho\sigma\tau$-Wasserdampfabsorptionsbande bestimmt. TCWV und dessen Unsicherheiten werden auf Pixel-Basis für tageszeitliche und wolkenfreie Szenen über Land oder Ozean bereit gestellt. Das Verfahren kann auf Satellitensensoren adaptiert werden, die im nahen infraroten Spektralbereich messen. Der Algorithmus minimiert iterativ die Differenz zwischen simulierten und gemessenen Radianzen in den Wasserdampfabsorptionskanälen mit einer hochentwickelten *optimal estimation method*. Das Verfahren wurde auf die Kanalsetzung des *MEdium Resolution Imaging Spectrometer* (MERIS) auf ENVISAT und des *MOderate Resolution Imaging Spectroradiometer* (MODIS) auf Aqua und Terra angewendet. Die Adaption auf das *Ocean and Land Color Instrument* auf Sentinel-3 wurde vorbereitet.

Um die Leistungsfähigkeit des Algorithmus abzuschätzen, wurden prozessierte TCWV Daten mit mehreren unabhängigen bodengestützten Observationen verglichen, wie z.B.

von *Global Navigation Satellite System* (GNSS) Stationen and *GCOS Reference Upper Air Network* (GRUAN) Radiosonden. Aus diesem Vergleich gingen hohe Korrelationen und keine signifikanten Abweichungen hervor. Eine erste Einschätzung des Ozeanprozessors ergab einen signifikanten aber konstant positiven Fehler.

Der Algorithmus wurde auf MERIS *full resolution* Daten angewendet. Es zeigt sich, dass kleinskalige Variationen des Wasserdampfs in der Grenzschicht aufgelöst werden können. Eine Fallstudie präsentiert die Möglichkeit mit diesen Daten horizontale konvektive Rollen über Landflächen in Zentraleuropa zu detektieren.

Zusätzlich wurden die Unsicherheiten von Wasserdampfableitungsverfahren quantifiziert, welche Radianzmessungen im nahen infraroten Spektralbereich verwenden. Diese Studie beinhaltet außerdem die theoretische Bestimmung der optimalen Kanalsetzung, bei der die Unsicherheit des Verfahrens minimal ist.

Des Weiteren wurden die Einflüsse der Beschränkung auf wolkenfreie Gebiete und die geringe zeitliche Abtastung von TCWV-Verfahren, welche reflektiertes Sonnenlicht verwenden, abgeschätzt. Ein globaler TCWV Datensatz von bodengestützten GNSS Stationen, welcher nicht von Wolken beeinflusst ist, wurde dafür verwendet. Die Studie zeigt, dass Analysen von global gemittelten TCWV-Werten nur marginal dadurch beeinflusst werden, dass viele Bereiche der Erde maximal einmal pro Tag abgedeckt werden. Jedoch kann die Variabilität des TCWV an einem Tag größer sein als die Differenz zwischen dem vom Satelliten abgeleiteten TCWV und dem täglichen Mittel des TCWVs. Durch die Einschränkung auf wolkenfreie Gebiete ist der monatlich gemittelte TCWV-Wert signifikant niedriger als für bewölkte und nicht bewölkte Fälle zusammen.

Weitergehend wurde der statistische Zusammenhang zwischen TCWV und Wolkenparametern quantifiziert. Bodengestützte GNSS-TCWV-Daten über Deutschland wurden ausgewertet und mit den satellitengestützten Observationen von Wolkenparametern kollokiert, welche vom *Moderate Resolution Imaging Spectroradiometer* (MODIS) L2-Produkts extrahiert wurden. Das generelle Ergebnis der Untersuchung ist, dass TCWV und Wolkenwassergehalt (CWP) im Durchschnitt mit zunehmender Wolkenbedeckung ansteigen. Zusätzlich wurden Daten des hochaufgelösten COSMO-DE Modells und Reanalysedaten von ERA-Interim kollokiert. Es ergibt sich, dass die Modelle im Mittel

gleiche Ergebnisse liefern. Allerdings tendieren sie dazu, eine größere Anzahl von wolkigen Fällen mit weniger CWP zu produzieren.

List of Figures

List of Tables

Danksagung

Ich danke Prof. Dr. Jürgen Fischer für die Möglichkeit am Institut für Weltraumwissenschaften promovieren zu können, besonders für die angenehme Zusammenarbeit. Prof. Dr. Ralf Bennartz danke ich für die Übernahme des Zweitgutachtens und für die angenehme Zusammenarbeit im Projekt EMiR.

Meinen ehemaligen und derzeitigen Kollegen möchte ich für die tolle Arbeitsatmosphäre, Aktivitäten in den Pausen, auf Konferenzen und für die Beantwortung so vieler Fragen danken. Hervorheben möchte ich René Preusker, der mir bei allen Problemen geholfen hat, Cintia Carbajal-Henken für interessante Diskussionen und Florian Filipitsch, dem besten Zimmerkollegen den ich mir vorstellen konnte. Vielen Dank auch an Nicole Docter, Therese Keck, Sören Testorp, und Florian Tornow, die meine Arbeit gelesen und korrigiert haben.

Auch gilt mein Dank allen Mitautoren der bis zu diesem Zeitpunkt entstandenen Veröffentlichungen, sowie Dr. Galina Dick vom Geoforschungszentrum Potsdam für die Hilfe bei Problemen mit GNSS.

Ich bedanke mich bei meinen Freunden, die mir die Doktorandenzeit in der Freizeit erheitert haben. Meiner Familie, speziell meinen Eltern, gilt ein besonderer Dank für die großzügige Unterstützung.

Abschließend möchte ich meiner geliebten Kathleen für die moralische Unterstützung danken.